Warm Coronae for Magnetically Supported Disks in Accreting Black Holes

Author:

Dominik Gronkiewicz

A dissertation submitted in partial fulfillment
of the requirements for the degree of
Doctor of Philosophy

Nicolaus Copernicus Astronomical Center
Polish Academy of Sciences
Warsaw, Poland

Supervisor:
prof. dr hab. Agata Różańska

June 2024

Dedicated to my grandfather Jan,
who first showed me the stars.

Acknowledgements

I would not have gotten to this point in life without the continual support of my mother, Ewa, and my grandmother, Teresa. The values they passed down to me helped me navigate through life, even in the moments when it felt more like tumbling in space. Although this stage of my career took much longer than expected, they never lost their patience in encouraging me to achieve my goal. This thesis would certainly not be written, had it not been for my grandfather Jan who sparked my interest in science and technology, as well as gifted me binoculars that became my first astronomical instrument when I was five. Although he is not on our side of the stellar firmament to participate in my defense, he still lives deep in my heart, bringing inspiration and motivation to pursue and spread scientific knowledge. I feel nothing but gratitude for love and years of life dedicated by my family to raise and support me. *Dziękuję Wam za wszystko!*

Many people whom I met on my scientific path helped me get where I am, starting from dr Tomek Mrozek, my supervisor during my Master's in Astronomy, with whom my journey into X-ray astrophysics began. Anne-Marie Dumont, the creator of the TITAN and NOAR codes, for providing the tools used in this work and for taking the time to answer all our questions during our visit to Meudon, Paris. Pierre-Olivier Petrucci, my collaborator from IPAG, Grenoble, for the great memories from my visits to France, including many exciting discussions and brainstorm sessions, during which our project was developed. Most of all, however, I would like to thank my supervisor, prof. dr hab. Agata Różańska, who also became my mentor and support in many areas of life, and who was always there to provide guidance whenever I needed it. Our hours-long discussions involved not only science but also life and philosophy. Although I realize collaboration with me could be at times exhausting, it taught me many important lessons, and I am immensely grateful to have such an intelligent and wise person in my life.

My PhD allowed me to meet and spend time with many new amazing people from all over the world. I hope that our paths cross again someday, somewhere on this globe. I would like to especially thank my friends, many of whom are as close to my heart as family, including Daniel for his encouragement and support in my scientific pursuits, Kasia and David for their friendship and all great moments together, Agata, Agostino, Deepika, Dorota, Filip M., Filip K., José, Karolina, Magda, Marcin G., Marcin L., Radek, as well as many other souls whom I have the honor of being friends with. I have never felt alone since I moved to Warsaw because I knew there was always someone there for me, even in trying times. You made this period in my life as amazing as it could be.

Last but not least, I would like to thank Fatima. Over the last year, we have shared many beautiful and unforgettable moments in life, as well as the pains of finishing our doctoral degrees. Without her patient support, I would not have had the strength to accomplish this task, which one year ago felt impossible and so far away, yet here I am writing these words. Thank you for making my life meaningful.

تو ستاره‌ای هستی که در آسمان یافتم وقتی همه امیدم را از دست داده بودم

Abstract

One of the features present in the X-ray spectra of both black hole X-ray binaries (BHXBs) and active galactic nuclei (AGNs) is excess of soft X-ray photons around 1-5keV. Many studies have demonstrated that it is well-described by Comptonization of soft photons in a warm (around 1 keV) and optically thick (τ = 10-50) coronal layer above the accretion disk. Alternative explanations have been proposed, such as relativistically smeared reflection from the disk illuminated by a hard X-ray continuum. The true origin of soft X-ray excess is still a topic of debate, and this thesis is dedicated to explore the scenario of warm, optically thick and scattering-dominated corona as its possible origin. Theoretical and observational background of this work, together with the aim of my research and most important conclusions are given in the Introduction.

Physical models show that the warm corona consistent with observations cannot be sustained unless some mechanism heating the atmosphere is provided, and this process is very likely driven by the magnetic field. I developed a new numerical code to calculate structure of the magnetically supported disk and corona with all relevent physical processes, which I describe in Paper I. Input parameters for the code are: mass of the black hole, accretion rate, radius and magnetic dynamo parameter. The code computes: gas density, temperature, radiative pressure and flux as well as magnetic pressure as a function of height above the disk equatorial plane. I implemented numerical relaxation method allowing to solve non-linear ordinary differential equations. I showed that if magnetic pressure and heating are included in the vertical structure, a warm and optically thick corona with properties consistent with the observations of black hole X-ray binaries is naturally formed above the accretion disk. I was able to calculate density and temperature structure of the accreting matter for a wide range of parameters.

Using my code I performed analogical computations in the case of supermassive black holes in AGN and presented the results in Paper II. I showed that free-free opacity at the base of the corona causes favorable conditions for the local thermal instability, which may result in matter collapsing into two-phase medium. I computed disk/corona models for a very wide range of parameters, such as black hole mass, magnetic field strength and the accretion rate. I determined that increasing the magnetic field support can stabilize the accretion disk, eliminating the radiation pressure instability. By generating a synthetic population of accretion disk models, I was able to reproduce the distribution of soft excess parameters in AGN in good agreement with observations recently published in the literature. Although my initial assumption to take the temperature minimum as the base of the warm corona overestimated the optical depth of the warm corona, partial collapse of the warm skin due to thermal instability could remove this discrepancy.

The aim of Paper III, is to compute a realistic spectrum of a internally heated warm corona which is simultaeously illuminated by hard X-ray radiation. I use photoionization code TITAN coupled with Monte Carlo photon tracing code NOAR to determine the temperature and ionization structure of the plane-parallel constant-density slab. Thanks to using Monte Carlo method, I am able to study separately the spectrum of the reflection from the ionized atmosphere and warm Comptonization. I determine that the warm Comptonization spectrum is featureless and does not contain emission nor absorption features. By computing models over a large parameter space of internal heating rate and optical thickness of the layer, I confirm that internal heating must be present Comptonization must be the dominating cooling process to obtain soft X-ray spectrum which is consistent with observations.

Streszczenie

W widmach rentgenowskich układów podwójnych z czarną dziurą (Black Hole X-ray Binaries, BHXB) oraz aktywnych jąder galaktyk (Active Galactic Nuclei, AGN) obserwowana jest nadwyżka miękkich fotonów rentgenowskich w zakresie 1-5 keV (Soft X-ray Excess, SXE). Cechę tę można dobrze wytłumaczyć mechanizmem komptonizacji miękkich fotonów w ciepłej (około 1 keV) i optycznie grubej (τ = 10-50) koronie nad dyskiem akrecyjnym. Zaproponowano również alternatywne wyjaśnienia, na przykład rozmyte relatywistycznie odbicie twardego promieniowania rentgenowskiego od częściowo zjonizowanego dysku. Prawdziwe pochodzenie SXE jest nadal przedmiotem aktywnej debaty naukowej, a niniejsza praca poświęcona jest badaniu scenariusza ciepłej, optycznie grubej korony zdominowanej przez rozpraszanie jako możliwego wytłumaczenia tego zjawiska. Teoretyczne i obserwacyjne tło tej pracy, cel badań oraz najważniejsze wnioski zostały przedstawione we wstępie do pracy.

Dotychczasowe rozwiązania modeli fizycznych ciepłej korony sugerują, że do jej zasilenia wymagany jest mechanizm deponujący energię w atmosferze, który najprawdopodobniej jest związany z polem magnetycznym. W Publikacji I opisuję stworzony przeze mnie nowy kod numeryczny pozwalający na obliczenie struktury pionowej dysku akrecyjnego z uwzględnieniem wszystkich istotnych procesów fizycznych. Parametrami wejściowymi dla programu są masa czarnej dziury, tempo akrecji, promień oraz parametr dynama magnetycznego. Kod oblicza: gęstość gazu, temperaturę, ciśnienie oraz strumień promieniowania, a także ciśnienie magnetyczne jako funkcja wysokości nad płaszczyzną równikową dysku. Zaimplementowana przeze mnie metoda relaksacji numerycznej pozwala na rozwiązanie nieliniowych równań różniczkowych zwyczajnych. W powyższej pracy pokazałem, że uwzględnienie grzania oraz ciśnienia magnetycznego w strukturze pionowej powoduje uformowanie ponad dyskiem akrecyjnym ciepłej korony o właściwościach zgodnych z obserwacjami BHXB. Przeprowadziłem obliczenia struktury pionowej gęstości oraz temperatury akreującej materii dla szerokiego zakresu parametrów.

Korzystając z mojego kodu, przeprowadziłem analogiczne obliczenia dla supermasywnych czarnych dziur w AGN. Wyniki przedstawiłem w Publikacji II. Wykazałem, że nieprzezroczystość wolny-wolny u podstawy korony stwarza korzystne warunki do zajścia lokalnej niestabilności termicznej, skutkującej zapaścią materii do postaci dwufazowej. Obliczyłem modele dysku z koroną dla bardzo szerokiego zakresu parametrów, takich jak masa czarnej dziury, siła pola magnetycznego i tempo akrecji. Określiłem, ze zwiększenie magnetyzacji może stabilizować dysk akrecyjny, eliminując niestabilność ciśnienia promieniowania. Generując syntetyczną populację modeli dysków akrecyjnych udało mi się odtworzyć rozkład parametrów SXE w AGN, zgodnie z zależnościami wynikającymi z obserwacji publikowanych ostatnio w literaturze. Choć moje początkowe założenie, że minimum temperatury jest podstawą ciepłej korony, przeszacowywało optyczną głębokość ciepłej korony, częściowa jej zapaść z powodu niestabilności termicznej mogłaby usunąć tę rozbieżność.

Celem Publikacji III było obliczenie realistycznego widma wewnętrznie ogrzewanej ciepłej korony, jednocześnie oświetlanej przez twarde promieniowanie rentgenowskie. Użyłem kodu fotojonizacyjnego TITAN sprzężonego z kodem Monte Carlo NOAR do określenia struktury temperaturowej i jonizacyjnej płasko-równoległej warstwy o stałej założonej gęstości. Dzięki użyciu metody Monte Carlo byłem w stanie oddzielnie zbadać widmo odbicia od zjonizowanej atmosfery i ciepłej komptonizacji. Pokazałem, że widmo ciepłej komptonizacji jest pozbawione cech, takich jak linie emisyjne czy absorpcyjne. Poprzez obliczenie modeli dla dużej przestrzeni parametrów

wewnętrznego tempa ogrzewania i grubości optycznej warstwy, potwierdziłem, że występowanie dodatkowego ogrzewania oraz dominacja chłodzenia komptonowskiego w obrębie warstwy są niezbędne, aby uzyskać widmo SXE zgodne z obserwacjami.

Contents

Chapter 1

Introduction

1.1 Accretion

Accretion of gas onto compact objects, either black hole (BH) or neutron star (NS), is one of the most powerful way of energy production in the Universe. Due to the high mass-to-radiation efficiency of the accretion process (order of 0.1, which is far greater than the value for – among others – nuclear fusion), the large amount of gravitational energy is then converted into electromagnetic flux and radiated away towards an observer just before matter will fall onto a compact object. This process – simple at first glance, but very complicated in detail – is behind multiple fascinating phenomena observed in the Universe at different times and scales. It is a crucial source that provided us with many important facts about the most dense, and often normally invisible, objects known in the Universe. Accretion explains the nature of distant quasars powered by monstrous supermassive black holes (SMBHs) and Galactic X-ray transients. Neutron stars and black holes – remnants of stellar evolution – may accrete matter from their companion stars, often exhibiting fascinating and violent temporal evolution. The accretion above the Eddington limit is most probably responsible for the high energy emitted by ultraluminous X-ray sources – ULXs.

Accreting sources display a set of common and diverse spectral characteristics, that can be seen in a very wide wavelength range from infrared to – most notably, largely distinguishing them from the background – X-rays. Different cutting-edge observatories have to be used to construct full spectral energy distribution of accreting compact objects, with the special role of X-ray telescopes, for which the study of accreting compact objects was often the main scientific goal of the mission. X-ray satellites, unaffected by the absorption of high-energy photons in Earth's atmosphere, allowed us to discover components and mechanisms of emission in regions around compact objects.

X-ray spectra of accreting black holes are diverse, but it is possible to point out several components that generally appear in most objects. One of them is the power law X-ray continuum, which was the first spectral feature to be studied and measured until X-ray instrumentation allowed us to obtain spectra at better resolution and quality. Despite the presence of other spectral features, the slope of the X-ray power law is still one of the first parameters determined for the source and used to diagnose its state. Many objects, particularly AGNs, will also present an excess of photons at lower energies ($\sim 0.1 - 1$ keV) above the power law. This soft X-ray excess (SXE) is one of the central phenomena this thesis will treat. Another prominent feature is the iron K_α emission line located at $6.4 - 6.7$ keV, as well as many other lines and features produced in the surface layer of the cold accretion flow ionized by external illumination. Finally, winds and outflows may produce absorption or emission lines, typically much narrower than ones originating in the accretion flow.

X-ray spectra are the most powerful way to study compact objects. They allowed us to measure the temperature of electrons in X-ray corona. They showed that the spectral features of the

accretion disk are distorted exactly how Einstein's Theory of General Relativity predicts. They help to study the structure of the atmospheres of accretion disks. Finally, they can be used to probe the geometry of the central engine in AGNs.

1.1.1 AGN

As determined by the measurements of the stellar motion in the cores of galaxies, massive objects, that could be anywhere between 10^6 and 10^9 solar masses must reside in the centers of majority of them. In some of the galaxies, such as the Milky Way, the radiative activity around the central object is insignificant, and while detectable in X-ray or radio domains, the bolometric power of the emitted radiation is low. Other objects, that I will refer to as Active Galaxies, have cores where active accretion onto the supermassive black hole – which we have identified to be the central object – causes extremely luminous emission of electromagnetic radiation across the whole spectrum.

The first quasars were discovered as radio sources in the 1950s, but the real significance of this discovery was understood when their peculiar, highly redshifted spectral appearance, fast variability timescale, combined with apparent luminosity comparable to stars from our Galaxy suggested that these objects must be at the same time extremely distant, luminous and compact (Schmidt, 1963). After all, processes known in astrophysics up until that point had failed to provide an explanation for such an extreme property of the newly discovered sources, involvement of the black holes – a novel, exotic cosmic object, suggested barely 50 years before by Albert Einstein – as the driver behind this luminous phenomenon, opened a new and exciting chapter in the history of astrophysics (Salpeter, 1964; Zel'dovich, 1964).

The electromagnetic spectrum that is emitted by these objects is a sum of complex phenomena and is generally understood in terms of a well-established unified model of AGN (Urry & Padovani, 1995), although details are still a topic of debate and research. The AGN emission spectrum is very rich due to extreme conditions caused by the accretion of matter onto a supermassive black hole, which results in the coexistence of very hot (10^9 K) and relatively cold (10^4 K) matter, interacting with and reprocessing the energetic ionizing radiation. Additionally, the appearance of the AGN spectrum will vary strongly between objects, partly due to intrinsic differences in the sources, but also strong non-isotropy of the emission causing variations in appearance due to the viewing angle, as demonstrated in Fig. 1.1.Starting from the electromagnetic waves of the lowest energy, radio waves primarily originate from jets of particles that are ejected from the vicinity of the black hole, emitting synchrotron radiation (Padovani et al., 2017). Infrared radiation is typically associated with the thermal emissions of dust within the torus structure surrounding the black hole and the accretion disk, re-emitting absorbed ultraviolet and visible light (Müller-Sánchez et al., 2016).

The visible and ultraviolet emission predominantly originate from the accretion disk surrounding the black hole, where the flow of infalling matter dissipates the gravitational energy by heating up to hundreds of thousands of Kelvins. In low-luminosity AGNs (LLAGNs), there is not enough matter to form an accretion disk that would cool itself radiatively, therefore a very hot and low-density flow (radiatively inefficient accretion flow, RIAF) is formed which is considerably less luminous than an optically thick disk but extends into much higher X-ray energies (has a more shallow slope of the spectrum). However, I mostly consider modes of accretion that do have an optically thick accretion disk, as more relevant to our study. Finally, processes in relativistic jets may upscatter photons into extreme energies, well in the gamma radiation range. An example of a broadband spectrum in the case of Active Galaxy Mrk 509 is presented in Fig. 1.2.

The energetic environment around the supermassive black hole in AGNs leads to several complex radiation reprocessing phenomena. Radiation reprocessing means that photons that were emitted as a result of one process, are driving or being subjected to another process, introducing

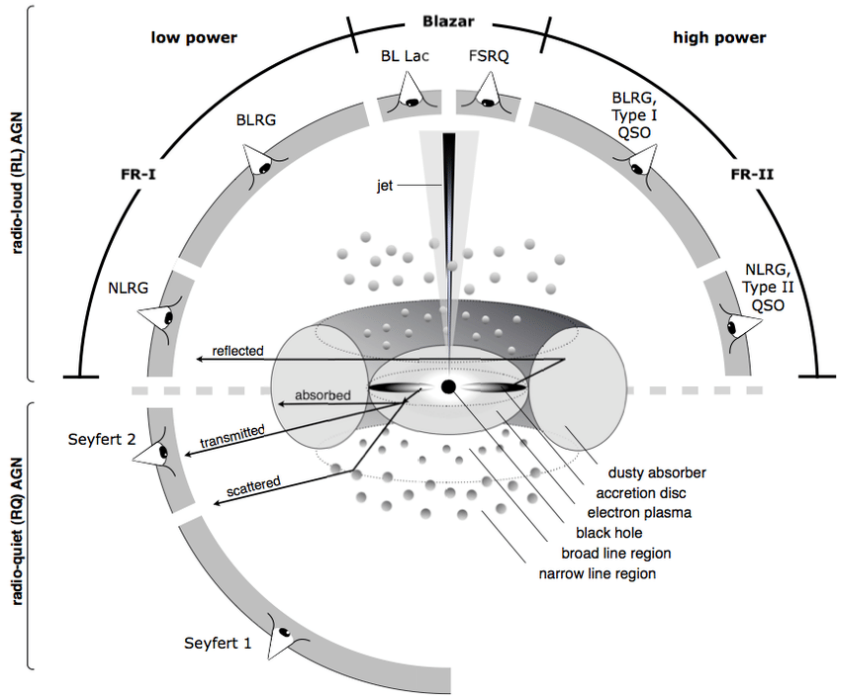

Figure 1.1: A generalized model of AGN demonstrates the location of the most important components typically present in the nucleus, as well as the classification of the objects depending on the angle that the system is viewed from. Reprinted from Beckmann & Shrader (2012).

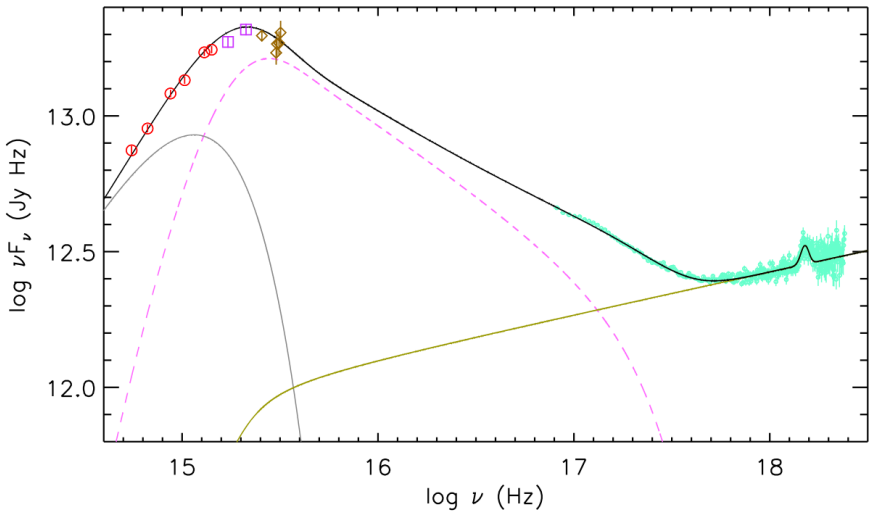

Figure 1.2: Broadband spectrum of Seyfert-1 galaxy Mrk 509. The red circles indicate the OM data on-board *XMM-Newton* observatory, the purple squares the HST/COS data, the brown diamonds the scaled FUSE data, and the green circles the absorption-corrected EPIC-pn data. The grey line represents the disc blackbody component, the magenta dashed line represents the warm Comptonization component which is responsible for the soft excess, and the olive line represents the broken power-law and incorporates a Gaussian for modeling the Fe Kα line. The black line represents the total spectrum of the model. (Mehdipour et al., 2011)

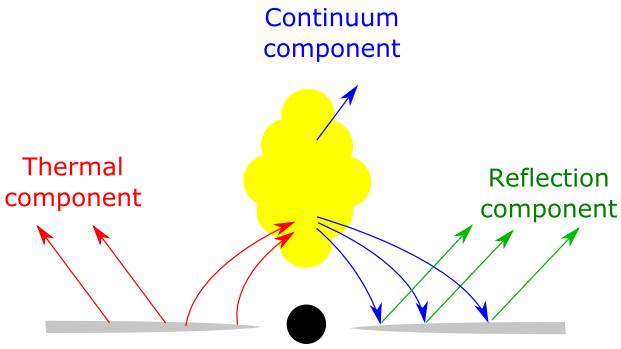

Figure 1.3: Sketch showing the reprocessing path of the radiation producing different spectral components, commonly observed in AGN and XRB (X-ray binaries) in the presence of an accretion disk. Reprinted from Bambi et al. (2021).

a new component in the spectrum. Our current understanding of photon reprocessing in compact objects can be summarized as follows: a pool of thermal photons emitted by the accretion disk inevitably propagates through a less dense yet extremely hot medium, likely surrounding the central object or sandwiching the disk, composed of sub-relativistic and relativistic electrons – the corona. Rare and hot plasma, heated by magnetic reconnection, shocks, or other mechanisms of particle acceleration, has very little way to cool itself, therefore electrons may easily reach relativistic energies. The flood of soft photons provides cooling to the medium by receiving the energy from electrons through inverse Compton scattering, resulting in a very hard, almost flat photon spectrum of scattered photons (Haardt & Maraschi, 1991). The latter can illuminate the disk, leading to reflection and re-emission, often as Fe Kα lines from the partially ionized "skin" of the disk (Pounds et al., 1990). Fig. 1.3 provides a simplified illustration of this dependency network. The reflection component forms a significant part of the X-ray spectrum of many AGNs (Ricci et al., 2011). The luminous ionizing continuum originating from the central engine reaches much further than that, illuminating cooler, slower clouds, and producing broad and narrow emission lines, typically in the optical regime. Finally, the finite speed of light introduces lags in these interactions, linking the temporal variability of the spectral components to the distances between sites of their emission and helping to constrain the geometry of the system.

This already paints a very complicated picture of the core of the active galaxies, despite many details having been omitted from this brief summary. Although there is still an ongoing discussion about the placement and geometry of the forementioned regions in the AGN core, the presence of such distinct components is clearly seen across many sources, and spectral as well as timing studies from currently operating and planned X-ray missions help us build a more complete picture.

1.1.2 X-ray binaries

X-ray binaries (XRBs) are a broad group of binary objects, where two bodies making the binary system are: the donor object (often a giant star) and the compact accretor (neutron star or a black hole). The latter is an accreting matter that is being lost by the donor object, either by emission of the wind, Roche lobe overflow, magnetically-driven accretion, or other mechanism. Such systems are categorized based on the mass of the donor companion: low-mass X-ray binaries (LMXB), which contain a companion at around solar mass in later stages of the stellar evolution, and high-mass X-ray binaries (HMXB) where the companion is a younger, hotter, more massive star. The latter appear generally more persistent in their luminosity, while the former undergo luminous outbursts interleaved between periods of quiescence. The kind of the accretor also has a large

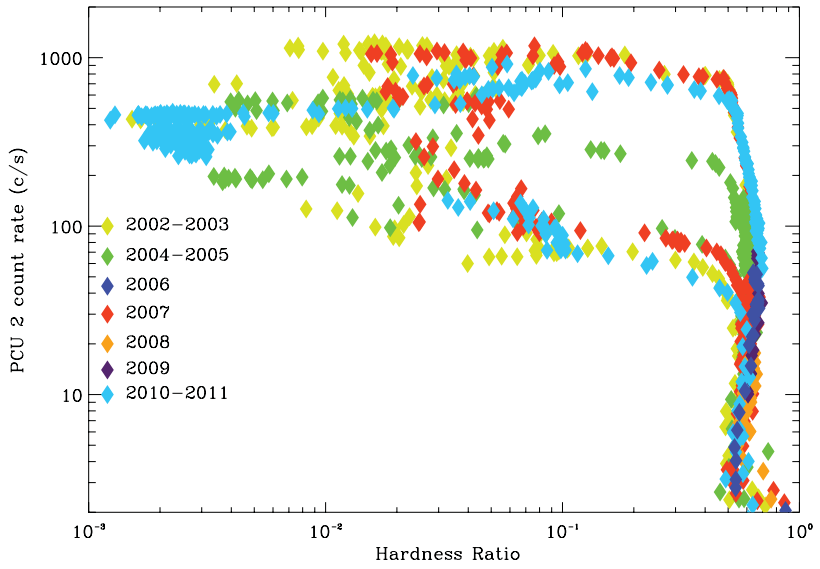

Figure 1.4: Hardness ratio – intensity diagram covering 10 years of outbursts of the BHXB GX 339-4, as observed by PCA (Proportional Counter Array) instrument on Rossi X-ray Timing Explorer (*RXTE*). The signal was background subtracted, and the hardness ratio was defined as the ratio of count rate in the bands 9.4–18.5 keV and 2.5–6.1 keV and the intensity as the count rate in the energy band 2.5–18.5 keV. Adapted from Corbel et al. (2013).

impact on the system behavior: neutron stars, unlike black holes, do have a hard surface and their own magnetic field, which introduces a range of interesting effects, such as thermonuclear flares on the surface, column accretion and pulsations due to rotation (Davidson & Ostriker, 1973). Black holes, on the other hand, have unconstrained mass, and in practice, black holes of stellar origin may reach up to tens of solar masses.

The X-ray emission of black-hole X-ray binaries (BHXBs) shows many parallels to the AGN, the continuum being a sum of soft component originating from an optically thick accretion flow and hard component attributed to the Comptonization of thermal photons by a hot corona, which geometry is not yet fully constrained (Makishima et al., 1986; Done et al., 2007). Other features, such as radio emission, jets, and outflows also may be observed (Remillard & McClintock, 2006). For BHXBs that emit collimated jets, the term "microquasar" was coined, since they appear to be miniature versions of quasars.

What is perhaps the most fascinating about LMXBs in particular is the violent evolution of the spectral state that they undergo (Homan et al., 2001; Churazov et al., 2001; Muñoz-Darias et al., 2011, and references therein). The observed states of XRBs, such as the high/soft state dominated by the soft excess and the low/hard state dominated by the power-law emission, are reflective of changes in the structure of the accretion flow and corona – interpreted as the presence of an accretion disk and hot, rare accretion flow, respectively (Belloni, 2010). The time of an outburst, when the system is luminous, might last from weeks to months (Homan et al., 2005). The evolution of the X-ray spectral state of the system is typically depicted in a hardness-intensity (HI) diagram, where the hardness of a spectrum is usually approximated by the photon index Γ. The evolutionary path plotted in this diagram often resembles the "q" letter as demonstrated in Fig. 1.4. The source traverses the hardness-intensity space counter-clockwise, starting from quiescence in the low-luminosity and hard state, followed by an increase in luminosity, then switching to a soft spectrum, gradual fall of the luminosity until it switches back to a hard spectrum and luminosity dying down back to the quiescent level.

1.1.3 ULX

Ultra-luminous X-ray sources are a puzzling class of objects. Just as AGNs were difficult to explain in the time following their discovery, ULXs have brought new challenges. They are typically defined by their absolute X-ray luminosity $L_X > 10^{39}$ erg s^{-1} (King, 2002). This is a huge value, and for typical galactic accretors (stellar mass black holes or neutron stars) obtaining such a power output would require super-Eddington accretion.

For some time, this large luminosity prompted curious speculations over the existence of intermediate-mass black holes (IMBHs). Increasing the accretor mass to around $10^4\,M_\odot$, placing them in the mass gap between stellar-origin compact objects and supermassive black holes, would naturally explain the observed luminosity without requiring new, unknown accretion modes (Colbert & Mushotzky, 1999). However exciting the perspective of a new class of black holes could be, many issues – primarily concerning requirements for their formation and some inconsistencies with observations, caused consideration of alternative models (King et al., 2023).

Observations of pulsating ULX (PULX, Bachetti et al., 2014) confirm that rotating, magnetized neutron stars accreting at super-Eddington luminosities could be driving at least some of the known objects. Non-pulsating ULXs could be driven either by a neutron star or a stellar-mass black hole. That super-Eddington accretion would be accompanied by a strong outflow, while the central body would gain only a small fraction of the inflowing mass. However, intense and fast wind would cause beaming of the radiation, increasing the apparent luminosity seen by the observer (Abarca et al., 2021). In this light, ULXs can be considered an extreme subclass of X-ray binaries.

ULX spectra are continuum-dominated, with a cutoff of the power law at around 10 keV. Notably, the iron Kα line is mostly absent and can be observed only in a couple of objects (Mondal et al., 2021), which suggests a high ionization state of the matter. However, blueshifted lines consistent with relativistic outflows have been observed (Pinto et al., 2016). The photon index Γ varies significantly between 1.5 and 3.5 (Kajava & Poutanen, 2009). This is explained by the unified model of the ULX (Poutanen et al., 2007; King et al., 2023), which predicts the spectrum of ULX to be strongly non-isotropic: as the observer moves closer to the accretion plane, the spectra become softer due to wind obscuration and reprocessing until the luminosity finally reaches $L_{\rm Edd}$ when viewed edge-on (Pinto et al., 2017).

1.1.4 Same mechanism, different scale

The aforementioned three classes of objects (AGNs, XRBs, and ULXs) are all powered by the same mechanism of accretion within a disk-like structure. The variations in their spectral characteristics and temporal behavior can be seen as part of a unified, overarching pattern, once we take into consideration the influence of both the mass of the central object and the rate of accretion (Merloni et al., 2003).

All of them exhibit two X-ray continuum components: hard X-ray power law and soft X-ray excess. However, accretion disk temperatures typically are much higher in XRBs (typical values of 10^{6-7} K,) due to the smaller size of the stellar mass black hole, compared to the cooler AGN disks (typical values of 10^5 K) which surround supermassive black holes (Koratkar & Blaes, 1999). As a consequence, XRBs prominently emit in the X-ray band, whereas the peak of the AGN spectral energy distribution (SED) is generally in the UV band, sometimes referred to as the Big Blue Bump. In the case of ULXs, the strong outflow may obscure the accretion disk and reprocess its radiation, hence a greater dependence of the spectral shape on the inclination angle is anticipated than for the other two classes.

Reflection features, including the iron Kα line, are frequently seen in the AGN and typical X-ray binaries, as long as the sufficiently cool disk is present and iron is not fully ionized. This

is not possible in a hard state in X-ray binaries and low-luminosity AGNs. Obviously, due to the difference of temperature and density of the disk photosphere between XRB and AGN (typically an order of 10^{12} K for AGN and 10^{19} K for galactic objects), different atomic transitions will be relevant. Reflection features appear to be much less pronounced in ULXs, however.

Outflows are a basis for the currently accepted ULX model, but they also are observed for other X-ray binaries and in AGN. The mechanisms of wind-launching are still a topic of debate and research, but radiation-driven winds are launched in ULX (Kitaki et al., 2021) and AGN (Hagino et al., 2015; Nomura & Ohsuga, 2017).

The characteristic timescales of variability are significantly shorter in XRBs and ULXs (ranging from milliseconds to hours) due to the smaller size of the system, while in AGNs these timescales can range from days to years (Ponti et al., 2012). Both ULX and X-ray binaries undergo state transitions that dramatically alter their spectral shape, and it is reasonable to expect that a similar phenomenon occurs in AGN (Kewley et al., 2006). We may not observe the transitions as they happen due to significantly longer timescales, but we may see different states across objects, depending on whether the black hole experiences abundance or scarcity of matter to accrete or the structure of the accretion changes (see discussion in Sec 7.1 of Done et al., 2012). The same is true for radio emission, which for XRB is observed in the hard state more often than in their soft state (Gallo et al., 2003, 2005). AGN equivalent would be the classification of different objects as radio-loud and radio-quiet (Rusinek-Abarca & Sikora, 2021). This provides us with a unique opportunity to study the rapid changes in XRBs as a scaled-down model for AGN behavior (Falcke et al., 2004).

1.2 Soft X-ray excess

1.2.1 Background

X-ray spectroscopy started with the launch of the first missions to escape the atmospheric absorption of energetic radiation. Before orbital missions such as *Uhuru* (Jagoda et al., 1972) provided us with the possibility of almost constant monitoring of the X-ray sky, sub-orbital rockets or even balloons carried the first X-ray instruments, typically made of a simple collimator and a proportional counter. Current X-ray missions are far more advanced and allow for registering energy, timing, and direction of photons with unprecedented precision.

Any spectrum obtained from an X-ray instrument (although this is also true for any other domain), is made of the signal from the observed object folded with the response of the instrument, such as cross-sections for different photon energies. The real-world response matrix is non-diagonal and generally difficult to invert, which means that it is error-prone to retrieve an accurate true spectrum of photons based on the spectrum of instrument counts. Instead, the most commonly used technique is to assume a parametrized, theoretical model of the X-ray spectrum, which is then folded with the instrument response matrix, and compared with observed data. A goodness-of-fit metric (for example, χ^2) is computed and through the iterative process, the best-fit model parameters can be found. This can be performed using publicly available software, for example as: *XSPEC* (Arnaud, 1996), *SPEX* (Kaastra et al., 1996) or *Sherpa* (Freeman et al., 2001).

Perhaps the most important step for the interpretation of the data is assuming the right theoretical models for fitting. Real astrophysical objects are very complex and poorly understood, which means that in practice, the model of the X-ray spectrum would consist of many components, each representing one part of the system. It is important to remember, however, that these are phenomenological models: each of them represents a spectrum emitted in a simplified, isolated system (such as blackbody radiation at a given temperature), and by combining them we attempt

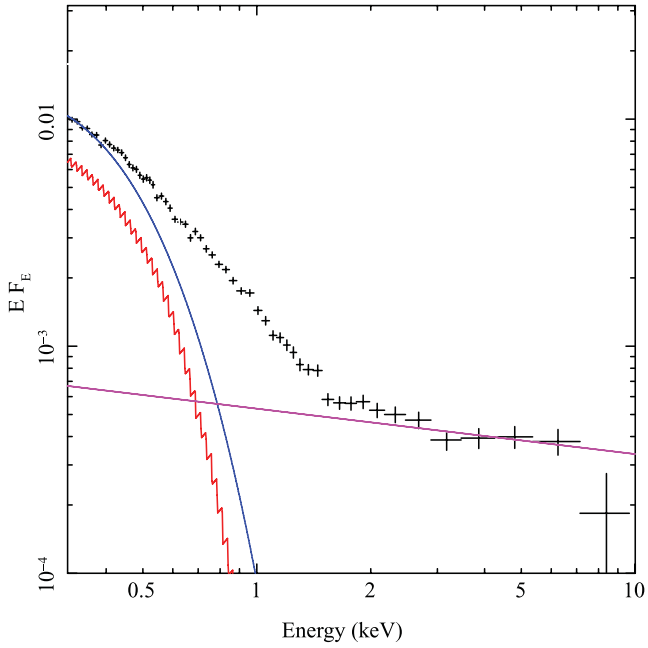

Figure 1.5: Spectrum of RE J1034+396 obtained by *XMM-Newton* (black points). Two model spectra have been computed for $M_{\rm BH} = 10^6 M_\odot$: disk spectrum obtained by radiative transfer calculations for $L/L_{\rm Edd} = 1$ is plotted in red, color-corrected blackbody disk spectrum for $L/L_{\rm Edd} = 1.15$ is shown in blue. Power-law, fitted for high-energy tail of the spectrum is violet. Reprinted from Done et al. (2012).

to model the spectrum given by a complicated physical system, at the same time acknowledging that we must ignore to some degree the physical consistency of relations between the components. Self-consistently modeling the spectrum of an entire system (which will be discussed in more detail in Section 1.3.4) is a very challenging task, especially in the X-ray astrophysics of compact objects, where often the geometry of the system is not exactly known.

The simplest theoretical spectrum, which works surprisingly well for many X-ray sources is the power law $I_E \propto E^{-\alpha}$ where E is the photon energy and α is the spectral slope. Photon index Γ is used more frequently in observational work and is defined as $\Gamma = \alpha + 1$ (Ishibashi & Courvoisier, 2010). For many objects power law alone is it is not sufficient to model the Spectrum, and extrapolation of power law from higher into lower X-ray energies underpredicts the photon count, yielding an excess of photons at energy around 1 keV. The term: soft X-ray excess (SXE) was coined for that spectral feature, which, as discussed in Section 1.1, may be seen in AGNs, XRBs and ULXs. First identified in AGNs in the 1980s thanks to progress in the quality of observations brought by *Einstein* and *EXOSAT* observatories, its presence has been confirmed in a significant fraction of both AGN and XRB populations Jin et al. (2012); Zhang et al. (2000).

Several physical explanations have been proposed for the SXE, including a thermal origin in a medium with a very stable electron temperature (Magdziarz et al., 1998) or a non-thermal origin, such as blurred absorption or emission feature Czerny & Elvis (1987); Gierliński & Done (2004b). The earliest explanations suggested that it could be due to thermal emission from the innermost regions of the accretion disk, but those were quickly found to overestimate the disk temperature. Currently, the SXE is modeled as Comptonized disk photons in a cool, optically thick corona (Done et al., 2012), or a reflection of the hard X-rays off an ionized accretion disk (Crummy et al., 2006). No single explanation has yet gained universal acceptance. In the sections below, I will expand on the observational characteristics of the SXE, followed by more in-depth elaboration regarding each model.

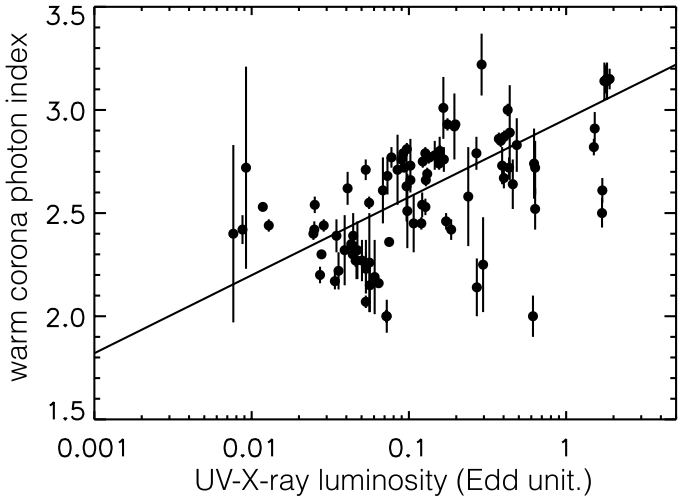

Figure 1.6: Corellation between the photon index Γ of the warm corona component fitted to *XMM-Newton* spectra of 22 objects, versus luminosity in the UV/X-ray band. For higher luminosities, an increase in the photon index indicates softer spectra. Reprinted from Petrucci et al. (2018).

1.2.2 Observations

The first observation of SXE can be attributed to Singh et al. (1985) in Mrk 509 and Arnaud et al. (1985) in Mrk 841. Since then, it has been well-established that Soft X-ray excess appears to be a common occurrence in the extragalactic sources. Turner et al. (1991) have found that 48% of the 25 Seyfert galaxies studied exhibit some form of SXE. Masnou et al. (1992) have found soft excesses in 8 out of 14 studied objects, confined to below 0.6 keV, and dominating the spectrum below 0.3 keV. Walter & Fink (1993) in their analysis of 58 Seyfert 1 type active galactic nuclei have found the excess above the power-law extrapolation of the high-energy part of the spectrum in 90% of the analyzed sources. The intensity of the excess was correlated with the intensity of the big blue bump in the UV range. Brunner et al. (1997) have studied 31 radio-quiet quasars, and have found that 90% of them show SXE. Reeves & Turner (2000) observed SXE in most of the radio-quiet quasars in their sample. Porquet et al. (2004) found soft excesses below 1-1.5 keV in 19 out of 21 low-redshift quasars they studied. Corral et al. (2011) – in 35 AGNs out of 41.

Kruper et al. (1990) from the study of 75 Seyfert galaxies have concluded the correlation between the steepness of the power-law X-ray spectrum of the object and its Eddington ratio – brighter objects have softer spectra. This correlation has been confirmed multiple times in more recent observations (Shemmer et al., 2008; Risaliti et al., 2009; Ishibashi & Courvoisier, 2010). Keek & Ballantyne (2016) studied Mrk 335 across different spectral states and established a very tight correlation for this object. However, some studies explored particularly photon index Γ produced by the SXE, separating it from the main power law by assuming some model for the spectrum of this component, typically warm Comptonization (I will refer to this quantity as $\Gamma_{\rm wc}$ for differentiation). Porquet et al. (2004) in their study of 21 low-redshift quasars found a positive correlation of photon index $\Gamma_{\rm wc}$ and the accretion rate as well as hard X-ray photon index Γ. Petrucci et al. (2018) showed a similar correlation between the SXE photon index $\Gamma_{\rm wc}$ and Eddington luminosity (Fig. 1.6). They found that $2 < \Gamma_{\rm wc} < 3$, with average being $\Gamma_{\rm wc} \approx 2.5$. An interesting exception that must be mentioned is work by Pal et al. (2021), demonstrating that this commonly established correlation can be occasionally inverted when comparing multiple observations of a single object performed at different epochs.

The timing analysis is another valuable tool used to study compact objects, where spectral fitting alone is troubled by parameter degeneracy. De Marco et al. (2013) and later Kara et al.

(2016) found that for Seyfert galaxies, soft X-ray seems to be lagging behind hard X-ray in the high temporal frequency range, but the opposite is true for long-term, low-frequency variability. On the other hand, Dewangan et al. (2007) found no correlation between the hard flux and SXE in Ark 564 and Mrk 1044, although they assumed no lag. Similarly, Mehdipour et al. (2011) determined no correlation of SXE with hard X-ray continuum in Mrk 509, but a strong correlation with UV continuum. Neither did Middleton et al. (2009), who analyzed Narrow-Line Seyfert 1 AGN RE J1034+396 with strong SXE and exhibiting quasi-periodic oscillations (Gierliński et al., 2008), and proved that the fast variability originates from the hard power law, and is completely independent of SXE. Jin et al. (2020) revisit this object by studying several observations carried out over 15 years, and conclude that the oscillation in the harder band langs behind the softer band by a stable time offset. In two *XMM-Newton* observations where the QPO is absent, the soft excess is found to be the strongest. They conclude that the mechanism of QPO must be physically linked to the soft X-ray component.

1.3 Spectral models of soft X-ray excess

Since the first observations of SXE in AGN and compact objects in general, there has been an ongoing discussion about its origin. Most – but not all, see for example Bourne & Nayakshin (2013) – agree that it is a signature of an accretion disk (Shields, 1978), although the exact radiative mechanism is still under debate. Multiple mechanisms were proposed as an explanation, involving radiation processes (emission or absorption) as well as geometries (reflection, extended corona emission, outflow). In this section, I will describe three scenarios that are mostly discussed in the recent literature: Comptonization of the radiation in the warm corona, absorption or emission in the relativistic outflow and relativistically smeared reflection.

1.3.1 Absorption

One of the scenarios proposed to explain the soft X-ray excess was the absorption features of ionized gas. In the frame of the gas, these features (edges, lines) are sharp and distinct, therefore to fit a featureless bump that SXE presents as relativistic smearing is required to smoothen the spectrum. This interpretation was motivated by the extraordinary stability of the SXE temperature inferred from the spectral cutoff, which could be explained by it being merely an absorption feature mimicking the cutoff of a thermal spectrum (Czerny & Elvis, 1987). Gierliński & Done (2004a) have studied observations of 10 sources, and have found that while the soft-band spectra can be explained by multi-color blackbody emission from the α-disk, the instability of that disk model calls for a different mechanism of heating. In the following papers, Gierliński & Done (2004b) and Gierliński & Done (2006) claim that instead of trying to fit the α-disk model parameters to the observations, SXE can be explained as being an artifact caused by strong but relativistically smeared, partially-ionized absorption from oxygen and iron, around 0.7 keV. This dip in the spectrum would cause an apparent excess of photons in lower energies.

The model combining absorption and emission by an outflow appeared to yield very good fits to the spectra of even strong X-ray excesses without the need for strong reflection features (Schurch & Done, 2006; Miniutti et al., 2010), at the same time avoiding the recurring issue of extreme parameters that are required by reflection models to fit the data (Sobolewska & Done, 2007). However, in recent years the smeared absorption models have declined in popularity. These models require very high speeds of the matter, up to around $0.9c$, to provide sufficient relativistic blurring to fit the spectra correctly (Schurch & Done, 2008). At the same time, numerical simulations struggle to provide matter outflow at a required speed or density Schurch et al. (2009).

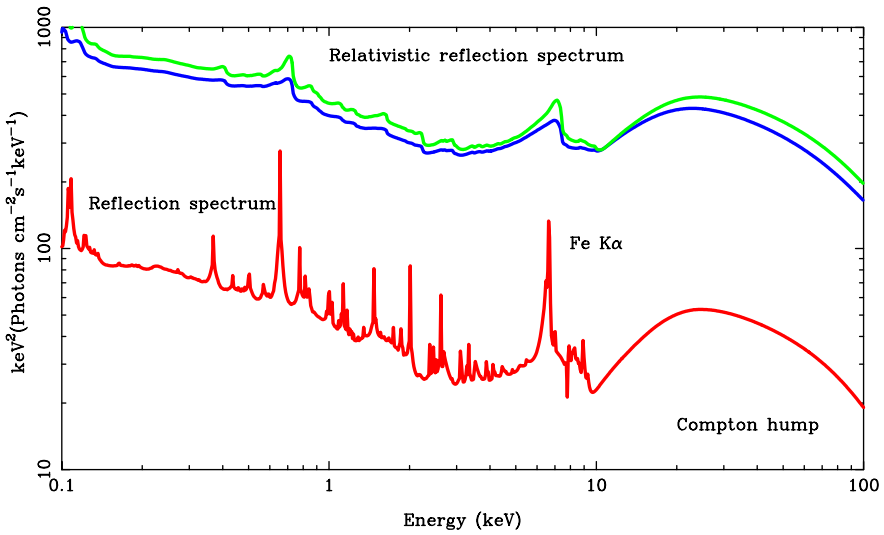

Figure 1.7: Reflection spectra obtained from *xillver* model, for slab at density $n_H = 10^{15}\mathrm{cm}^{-3}$ illuminated by incident X-ray radiation with photon index $\Gamma = 2$ and seen at inclination angle 45 degrees. The reflection spectrum as seen in the rest-frame in the disk is shown in red, while green and blue are spectra seen in the rest-frame of a distant observer, assuming black hole spin parameter $a_\star = 0$ (low spin) and $a_\star = 0.998$ (high spin), respectively. Normalization is shifted for clarity. Reprinted from Bambi et al. (2021).

1.3.2 Reflection

Reflection models typically assume the presence of a medium which is a site of abundant energy deposition and reprocesses the soft thermal photons into a hard spectrum extending into high energies. This reprocessed energetic radiation illuminates the accretion flow back. Such an irradiated atmosphere would be typically a partly-ionized medium with free electrons, which would scatter back some of the continuum, although with high-end energy cutoff imposed by diminishing Klein-Nishina cross-section and low-end with increasing true absorption, such as bremsstrahlung (Zdziarski et al., 1999; Gierliński et al., 1999; Rybicki & Lightman, 2008). Energy deposited by the intense radiation changes the temperature structure, causing temperature inversion. The ionization structure also follows to reach a new state of equilibrium. The energy range 0.1 keV–10 keV contains many atomic transitions of metals such as iron (notable for its prominent lines at around 6.4 keV–6.7 keV), magnesium, silicon, sulfur, arsenic, calcium, and chromium, which results in fluorescent emission in a plethora of spectral lines. Their intensities are very sensitive measures of the ionization structure of the atmosphere and deliver invaluable tools to measure conditions in partially ionized plasma (Ross & Fabian, 2005).

The reflection models are typically computed by solving the transfer of radiation alongside the ionization structure of the illuminated medium (Madej & Różańska, 2000b). Many factors, such as the shape and power of the incident radiation, as well as the temperature and density of the illuminated medium are important. The complex shape of the reflection spectrum can appear more continuum-like to an observer, however. A high ionization state due to strong illumination removes features from the spectrum. Since the origin of the reprocessed radiation is in a disk that might rotate at relativistic speeds, the spectral features may also be blurred, becoming less obvious as demonstrated in Fig. 1.7. Particularly at high assumed density, due to increased free-free opacity, some of the photons may become absorbed at $\tau > 0.1$, causing a spike in temperature and emission of blackbody-like spectrum peaking between 0.1 and 0.2 keV, as demonstrated in Fig. 1.8 (Jiang et al., 2019).

Using such models in application to the real data, Zdziarski et al. (1990) showed that reflection

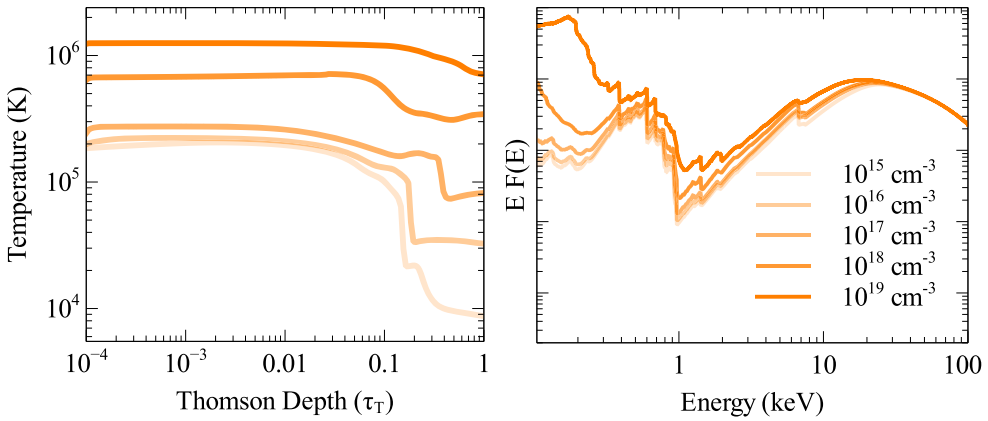

Figure 1.8: Temperature structures and spectra reflected from a high-density slab and modeled for different atmosphere densities. Ionization parameter $\xi = 50$, maximum black hole spin, and inclination angle of 30° was assumed. Reprinted from Jiang et al. (2019).

of the hard X-ray radiation illuminating a cold disk produces a spectrum with a pronounced soft X-ray excess at around 0.5 keV, provided a majority of the hard radiation is emitted towards the disk and not towards the observer. Czerny & Zycki (1994) studied the spectra of six Seyfert 1 galaxies. They have found that all except one (Mrk 335) give good fits to the model consisting of direct power law and reflection component, without the need for the separate component to produce the SXE. Fabian et al. (2005) could find a satisfactory explanation for the entire spectrum of Seyfert galaxy 1H 0419-577, including the hard part and the soft excess, by a two-component model which consists of power law and a reflection component. A similar conclusion was reached by Crummy et al. (2006) who studied a sample of 34 sources, although they only assumed multi-color blackbody as a model for disk emission, without any Comptonization component. The variability analysis performed by Fabian et al. (2005) indicated that most of the hard X-ray emission comes from within a few gravitational radii from the central object, which is also confirmed by strong relativistic signatures in the reflection component. Fabian & Miniutti (2005) argue that soft excess originating from the thermal disk emission would be inconsistent with its roughly constant temperature across a large span of accretion rates and black hole masses. Finally, high-frequency soft-lag (De Marco et al., 2013) points towards the soft spectrum being causally secondary to the hard illumination, yielding a strong point towards the reflection scenario.

Attempting to explain SXE solely by the ionized reflection model causes issues, however. Purely theoretical predictions based on radiative transfer calculations indicated that reflection from a stratified atmosphere does not produce SXE due to the bound-bound and bound-free transitions on partially ionized heavy elements (Madej & Różańska, 2000b; Różańska et al., 2002). Nevertheless, in the same atmosphere being in hydrostatic equilibrium and fully taking into account flux from the underlying disk, which consists of hydrogen-helium only, the Compton process cannot compete with absorption on metals, and can strongly shift hard photons toward soft X-ray band thus producing SXE (Madej & Różańska, 2000b). However, the above models were never tested with observations. Done & Nayakshin (2007) found that the reflection models in hydrostatic equilibrium cannot sustain the ionization state required to produce soft excess, and even if constant density is assumed, they cannot reproduce spectra of some objects. Although there were many successful attempts to completely explain the spectrum with relativistically blurred reflection (García et al., 2019), the obtained parameters appear to be rather extreme, pointing towards at least some contribution from the warm Comptonization. A very similar conclusion regarding the extremity of parameters when using the reflection model was reached earlier by De-

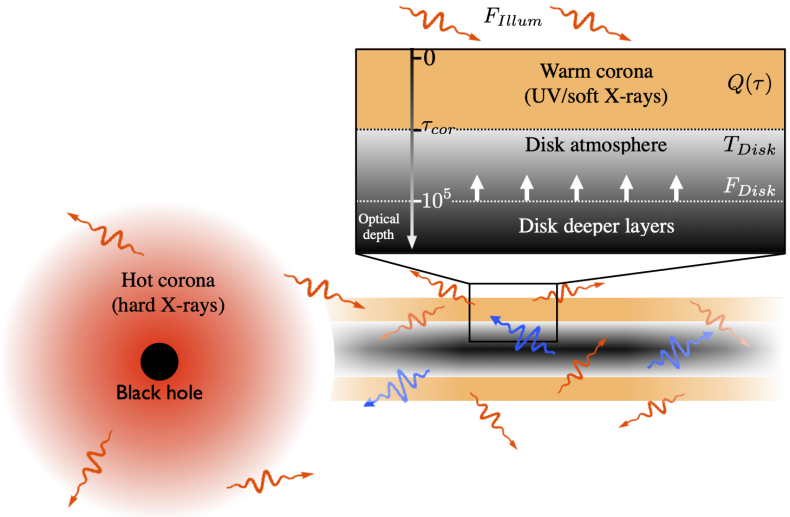

Figure 1.9: A sketch, presenting the two-coronae scenario: hot X-ray corona, shown as red shading surrounding the central object, and a slab-like heated corona covering the accretion disk and comptonizing its radiation. The vertical structure of an accretion disk with a covering corona is presented in detail. Reprinted from Petrucci et al. (2020).

wangan et al. (2007) and Sobolewska & Done (2007). While for some observations they indeed can completely describe the soft excess (Ding et al., 2021) including the time variability (Laha et al., 2014), for other objects they underestimate the soft flux (Ezhikode et al., 2023). It seems that, at least for some objects, there must exist another component to fill that discrepancy (Keek & Ballantyne, 2016).

1.3.3 Warm Comptonization

Another possible explanation for the SXE is the warm Comptonization scenario (Bechtold et al., 1987; Walter & Fink, 1993; Magdziarz et al., 1998; Dewangan et al., 2007; Done et al., 2012; Petrucci et al., 2013). The primary source of radiation, the accretion disk, emits low-energy photons which then interact with the coronal region. The physics behind Comptonization of astrophysical plasmas has been studied and well understood for decades (Sunyaev & Titarchuk, 1980; Madej & Różańska, 2000a; Petrucci et al., 2000; Madej et al., 2017). In this case, however, the corona itself is cooler and more optically thick than the hot corona that is typically considered to be a source of the hard power law radiation illuminating the disk in the reflection scenario, hence it is referred to as *a warm corona* – see Fig. 1.9 for illustration. The warm corona is characterized by its moderately high temperature (approximately 1 keV or around 10^7K) and high optical thickness (τ ranging from 10 to 20) (Done et al., 2012).

The medium is highly ionized, and electron scattering opacity is dominant. Because of its large optical thickness and much more moderate temperature, photons undergo multiple upscatterings before they reach the surface. The radiation spectrum inside the scattering-dominated corona has a Wien distribution (Rybicki & Lightman, 2008). However, the outgoing spectrum is slightly more complicated and may be computed using various models that contain more or fewer assumptions about the soft photon source and the comptonizing layer, one example being NTHCOMP.

The NTHCOMP model, based on the thermal Comptonization continuum model introduced by Zdziarski et al. (1996) and further refined by Życki et al. (1999), describes the spectral continuum shaped by Compton upscattering of low-energy seed photons in a high-energy electron cloud

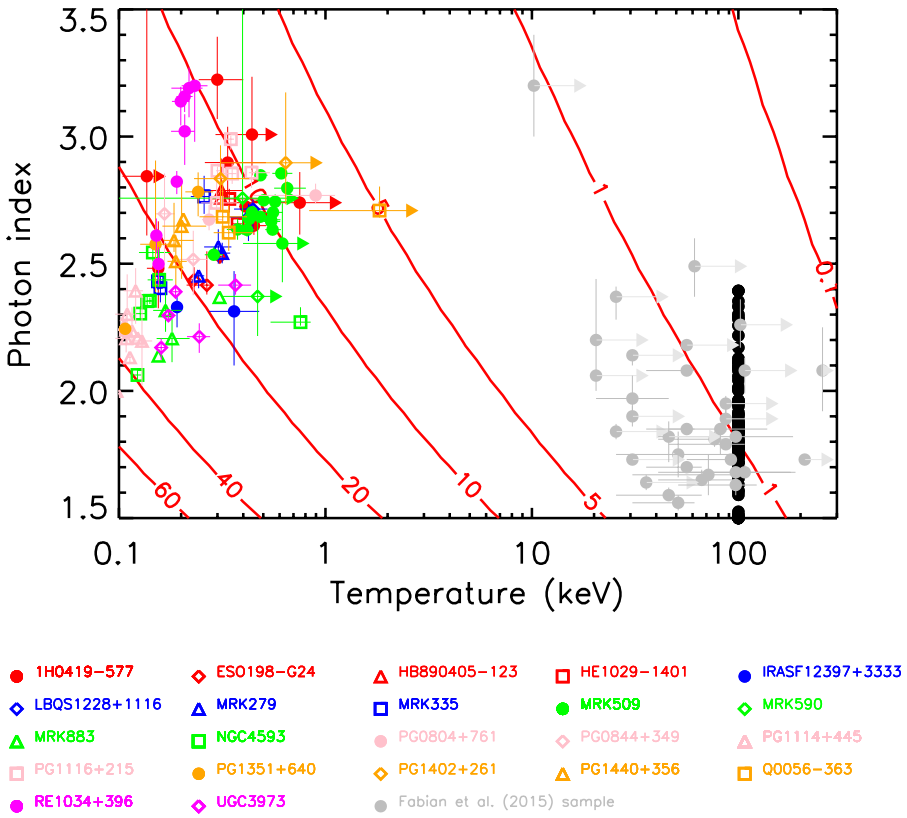

Figure 1.10: Temperature and photon index of SXE in 22 objects, obtained by fitting 100 *XMM-Newton* spectra using NTHCOMP model. Red contours show the optical thickness of the comptonizing layer. Green circles are measurements obtained from Mrk 509. Black points are the parameters obtained for the spectral component corresponding to the hot, optically thin corona, and grey points are fit results to sample of objects from another study (Fabian et al., 2015). Reprinted from Petrucci et al. (2018).

with greater accuracy than simple models, such as the exponentially cutoff power law. It is distributed as part of the *XSPEC* package. The model is parameterized by several inputs that describe the properties of the corona and the seed photons. The electron temperature (kT_e) specifies the temperature of the Comptonizing electrons, influencing the high-energy cutoff in the spectrum. Contrary to an exponential cutoff power law, the high-energy cutoff in the NTHCOMP model is sharper, generally resulting in the rollover energy E_c being approximately 2-3 times kT_e.

The spectrum of seed photons is typically assumed as quasi-blackbody or disk blackbody in shape, each represented by a seed photon temperature (kT_{bb}). Upscattering results in fewer photons at energies below the average seed photon energies, producing a notable low energy cutoff in the scattered spectrum, and making it significantly different from a simple power law below this energy. The shape of the spectrum between the low and high energy cutoffs is influenced by the combination of electron scattering optical depth and electron temperature. Although the spectrum is not strictly a power law in this region, it can be parameterized by an asymptotic power-law photon index (Γ), which may be approximated with the formula (Shapiro et al., 1976; Zdziarski et al., 1996):

$$\Gamma = \alpha + 1 = -\frac{1}{2} + \left(\frac{9}{4} + \frac{(kT_e)^{-1} m_e c^2}{\tau \left(1 + \tau/3\right)} \right)^{1/2} \tag{1.1}$$

where $\alpha = \Gamma - 1$ is the spectral index, k is the Boltzmann constant, T_e and m_e is electron temperature and mass respectively, τ is opticall thickness of a layer and c is the speed of light.

Simple models, such as NTHCOMP, come with the implicit assumption that the Comptonizing corona is isotropic, homogeneous, and perfectly scattering (the true absorption coefficient is equal to zero) which may not always hold true in all astrophysical scenarios. With that in mind, it is a great approximation, successfully applied to the analysis of X-ray spectra over the past 20 years (Magdziarz et al., 1998; Jin et al., 2012; Petrucci et al., 2013, 2018; Porquet et al., 2018; Tripathi et al., 2021).

Petrucci et al. (2013) can be considered an exemplary study (considered both observed object and used methodology) of Mrk 509, a high-luminosity AGN with SXE clearly present in the spectrum, due to high inclination angle allowing us to see straight into the nucleus (Singh et al., 1985). Based on observations from three orbital instruments (*XMM-Newton*, *INTEGRAL* and *Swift*), they performed fit to the broadband spectral data. Besides the used warm Comptonization model NTHCOMP, the primary X-ray continuum, warm absorber, and iron line are included in the model. They obtained very stable fits from all observations: the warm component had spectral slope $\Gamma \approx 2.53$, temperature $kT \approx 0.5$ keV corresponding to $\tau \approx 19$. Petrucci et al. (2018) extend the analysis using a similar methodology to 100 separate observations collected by XMM-Newton, particularly on UV and X-ray spectra of 22 unabsorbed radio-quiet AGNs. Results of warm Comptonization parameters obtained from their fits are shown in Figure 1.10. The spectral slope Γ ranged between 2 and 3.3, with a peak of the distribution being around Γ =2.7. Most sources show warm corona temperature below 0.4 keV, although it ranges between 0.1-1.0 keV. As already discussed in Sec. 1.2.2, Γ has a positive correlation with source luminosity, meaning that brighter objects have softer spectra, shown in Fig. 1.10. By solving some simplified energy balance equations, based on fitted spectral parameters the authors determined that most if not all of the accretion power must be released in the corona.

The typical approach, as done in the above studies, is to fit one warm and one hot Comptonization component. However, timing analysis introduces an extra dimension that may improve our capability to discern different components. Recently, studying the QPOs in Narrow-Line Seyfert 1 AGN RE J1034+396, Jin et al. (2021) find that two warm corona components best describe both observed spectrum and variability. A similar "double warm-corona" approach appears to be the most successful in an application to Seyfert 1.5 galaxy ESO 362-G18 by Zhong & Wang (2022).

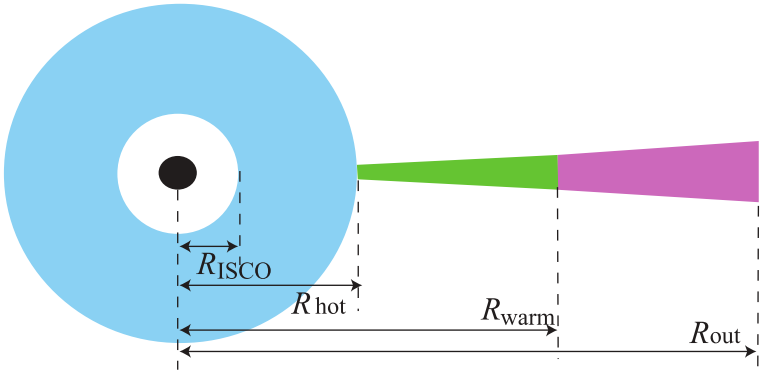

Figure 1.11: A sketch, presenting the radially stratified accretion model by Kubota & Done (2018). Starting from the black hole, the zones of the model are: hot flow zone, warm Comptonization zone and cold disk zone.

Although simple phenomenological models like NTHCOMP can be built for basic geometries, such as plane-parallel atmosphere or spherical halo, the method for obtaining Comptonized spectra for arbitrary geometry and ionization state of the matter is needed. Monte Carlo methods have been extensively utilized to address this challenge. Due to the discrete and stochastic nature of the process, these methods are very well fit to the task and very easy to compute by parallelized numerical codes. There have been many linear (Dumont et al., 2000) and non-linear (Dove et al., 1997a,b) implementations of Comptonization in compact object environments, which can be performed on pre-computed structures, either by radiative transfer code or MHD simulation (Schnittman et al., 2013). Typically, these are implemented by injecting photons into the system and tracing them as they get scattered in the medium until their absorption. Such techniques allow for better accounting of different absorption phenomena and geometrical effects of the cloud than analytic models such as the popularly used NTHCOMP model.

Their weakness, which may be partially mitigated, is the difficulty in keeping track of the proper photon count, which can be tricky, especially in media where the photon absorption probability $\epsilon = \kappa_{\rm abs}/\left(\kappa_{\rm abs} + \kappa_{\rm es}\right)$ is anything but very close to zero. In the case of a perfectly scattering medium, the photon number is conserved, only its energy may be shifted by Compton interaction with electrons. Even small true opacity causes many photons to end up being absorbed and never leave the system. In nature, such energy would likely be re-emitted by creating new photons, but in this process, the photon number is not conserved, which is opposite to what happens in scattering. While for optically thin layers this effect may be negligible, when considering optically thick atmospheres photons may experience tens to hundreds of scatterings and even $\epsilon \approx 0.1$ means that a significant number of photons will be emitted and absorbed in the medium itself. This to be correctly accounted for to produce a spectrum with accuracy that would make it practical to use, and such photons would be much lower energy and more numerous for X-ray photons. The codes need to carefully keep the photon pool alive by re-injecting the absorbed photons. These challenges are very clearly described in the paper by Dove et al. (1997a). Despite these limitations, Monte Carlo methods can still be a good tool to study Comptonization in partially absorbing atmospheres (see Paper III).

1.3.4 Self-consistent approach

As I discussed before, until very recently most observational models were phenomenological and considered each component of the spectrum (such as soft excess, reflection, disk emission, etc.) in isolation. In some cases, this approach may lead to inconsistency. One of them could be the

geometry of the system: the luminosity of a spectral component is limited by the physical size of the medium by which it is emitted. Likewise, distances and angles between interacting media (for example, the distance and solid angle between the hard X-ray source and the reflecting surface in the lamp-post scenario) will also constrain the subset of possible output spectra, allowing to removal of some degeneracy of model parameters during fitting to data. Linking different emission mechanisms into a consistent model is particularly advantageous when studying broadband spectra. Such an approach allows us to ensure rough physical accuracy, as the most implausible scenarios are ruled out, but falls short of the fully self-consistent physical model, although recent 10 years have brought significant progress and current state-of-the-art models include more and more mechanisms jointly calculated in a self-consistent way.

The precursor to such an approach which must be noted in this place is a fundamental paper by Haardt & Maraschi (1991). They have described a model where the disk is sandwiched between the corona on either side. Model is parametrized by fraction f of total thermal output that is dissipated in a corona through a mechanism described by Galeev et al. (1979), and which is cooled by the Comptonization of the soft photons. The significance of this research was that the energy budget divided between the accretion disk and the corona was considered, providing at least some physically motivated constraint. They model the spectrum by Monte-Carlo photon tracing. To match the X-ray spectral slope index of the primary X-ray spectrum $\Gamma \approx 1.9$ seen in the Seyfert galaxies, almost the entirety of the accretion energy need to be deposited in the corona, so $f \approx 1$ and the disk would be passive. Although their model is simple and only considered a hot and optically thin corona, it introduced the idea of an active corona and a passive disk. The f parameter defined as the coronal power fraction is still used today, as is determining disk-corona system energy budget from the X-ray spectra, as used by, for example, Petrucci et al. (2018).

An example of a more recent and well-established model that ties together multiple spectral components, such as warm and hot comptonization as well as disk emission was developed by Done et al. (2012) and extended by Kubota & Done (2018) and – introducing relativistic raytracing effects – Hagen & Done (2023). The model does not contain reflection from a partially ionized surface and is focused on the prediction of the continuum emission. Unlike models where the warm corona covers the entire accretion disk (or at least the most significant portion of it), they assume radial stratification into three zones: hot Comptonization, warm Comptonization, and cold disk zone. The geometry of the model is shown in Figure 1.11. Output spectrum is computed by integrating spectra emitted by each of the annuli, which are modeled by simple approximations: color-corrected blackbody following Shakura & Sunyaev (1973) temperature distribution – in the cold disk zone, NTHCOMP seeded with photons consistently with underlying thin disk temperature – in the warm Comptonization zone and power law with fixed cutoff – in the hot corona. The energy budget of all components is calculated, therefore the resulting output spectrum is physically self-consistent. The models of Done et al. (2012), Kubota & Done (2018) and Hagen & Done (2023) are available for *XSPEC* under names: OPTXAGN, AGNSED and RELAGN, respectively.

The OPTXAGN model underwent observational test by Jin et al. (2012) who conduct a comprehensive study of the continuum and emission lines of 51 unobscured type I AGNs, including 11 NLS1s and 40 BLS1s by fitting the model to the broadband data from optical to X-ray. NLS1s have lower black hole sizes and higher accretion rates, even though distributions of the bolometric luminosity are similar, according to the model fits. Electron temperature for the warm corona was found to be in 0.2 keV range, while the optical depth varied between 10 and 30, with the average being around $\tau \approx 12$. The radial extent of the corona was constrained to $50 - 60 R_{\rm g}$ on average. Both parameters do not seem to exhibit a large difference between NLS1 and BLS1 subsamples of the group, although they did show that NLS1s exhibit a higher ratio of corona-to-disk luminosity compared to BLS1s. Kubota & Done (2018) tested AGNSED model on three sources (NGC 5548, Mrk 509 and PG1115+407) with accretion rates ranging from $0.03\dot{M}_{\rm Edd}$, $0.1\dot{M}_{\rm Edd}$ and $0.4\dot{M}_{\rm Edd}$,

respectively. The power output of the hot flow is almost constant with the accretion rate. They confirm the "softer when brighter" behavior. The determined size of both hot and warm corona region is shrinking with the accretion rate, although for higher accretion rates the spectrum is modeled well also by warm corona extending over the entire disk. Both scenarios are difficult to distinguish due to the gap in EUV region of the spectra.

Another issue that is difficult to study using decoupled models for different spectral components is the consistency of the ionization structure. For example, it is well-established that the warm Comptonization layer on the disk requires additional local heating in that layer (Różańska et al., 2015), which also will cause an increase in the temperature of the matter until the new equilibrium is reached. This will also influence the ionization states of the elements, and consequently the spectrum of the reflection should this layer be illuminated by ionizing radiation. The true spectrum of such a system would be different than the sum of warm Comptonization and reflection components evaluated separately.

The only way to address this issue is to self-consistently compute the structure of the disk atmosphere including all significant processes and interplay between them. This is non-trivial, as computing the ionization equilibrium is a difficult task on its own, and including Comptonization in the calculations brings its own set of challenges. My attempt to tackle this issue is described in Paper III. Recent years since that publication have brought further advancements in this area.

Ballantyne (2020) shows radiative transfer computations of accretion disk atmosphere which is both irradiated by hard X-ray power law and heated internally by a uniform heating function. The ionization and temperature structure of the plane-parallel atmosphere is computed self-consistently, and Compton scattering redistribution functions are taken into account, therefore the outgoing spectrum contains all Comptonization features. The atmosphere is optically thick and both constant-density and hydrostatic equilibrium variants are considered. A grid of models assuming different densities, optical depths, and internal heating rates, was computed, showing that obtaining the spectrum consistent with observations requires choosing parameters within a limited region. It was confirmed that Comptonization must be a dominant process to obtain the proper spectral shape and that there is an upper limit on density, outside of which the warm corona is difficult to sustain due to very strong radiative cooling. When the hydrostatic equilibrium was included, a sharp drop in density and increase in temperature and Compton cooling was formed, although it was only a skin of the atmosphere at $\tau \leq 1$. (Ballantyne & Xiang, 2020) continued the study, by testing the model on a more dense parameter grid and determining values of typical observables, such as spectral index Γ or fluxes computed over different energy bands. They predict that a higher accretion rate should lead to stronger soft excesses.

Following computation for different radii, black hole parameters, and including relativistic effects, the model for the spectrum of the entire accretion disk was released for use with *XSPEC* as reXcor (Xiang et al., 2022). The four model parameters are warm corona heating fraction and Thomson depth, as well as hard X-ray photon index and hard X-ray power fraction. Models for different black hole masses, spins, accretion rates, and lamppost heights are available. The model is tested on two Seyfert 1 galaxies, HE 1143-1820 and NGC 4593. Obtained values for the warm corona fraction h_f and optical depth τ for several observations are around $h_f \approx 0.4$ and $\tau \approx 11$ (HE 1143-1820); $h_f \approx 0.5$ and $\tau \approx 25$ (NGC 4593). The origin of the heating of the warm corona in this model is connected to purely viscous dissipation of accretion energy by standard disk, and the total dissipated energy is divided between three emitting regions: cold disk, warm corona and hot corona. Given that, a hot corona needs to be powered as well, the authors concluded that 50% of the total accretion energy powers the warm corona, which supports the existence of large level of heating.

Porquet et al. (2024) analyzed simultaneous *XMM-Newton* and *Nustar* data of Mrk 110 using both models: relagn and reXcor. This study is very interesting, as it directly compares two

distinct approaches to modeling. From reXcor fits, they obtained $h_f \approx 0.5$ and $\tau \approx 15$ for black hole spin $a = 0.99$. Assuming $a = 0.90$, however, the results were $h_f \approx 0.7$ and $\tau \approx 20$. Hard X-ray contribution was found to be around 0.05. Despite the uncertainty surrounding spin, undoubtedly warm corona dissipates at least half of available accretion energy, which is different from than findings of Petrucci et al. (2018) based only on the Comptonization spectrum. relagn case (completed with reflection component modeled with relxillcp) constrained the radius of the warm Comptonization zone between 20 and 80 gravitational radii.

These recent advances show on one hand, how far our knowledge about radiative mechanisms governing the soft X-ray excess mechanism has progressed over the recent years. On the other hand, the direction of the study is clear: more accurate and realistic models incorporating multiple processes enrich better our understanding of reality than single scenarios.

1.4 Physical models

Both mechanisms that seem to have survived the trial of observational verification (reflection and warm Comptonization) require a huge energy output to power the production of SXE (Meyer-Hofmeister et al., 2012). The largest revolution since the first fundamental paper of Shakura & Sunyaev (1973) has been brought in the last three decades by the means of increasing the power of computers, which makes grid-based numerical simulations viable. They allow us to study the turbulent flow of the gas, interactions with the magnetic field, and radiation, often in three dimensions and with relativistic effects included. That does not mean that simpler models completely are out of place. Their simplicity, explainability, and speed in evaluation allow them to cover a wide parameter range, giving them an edge over time-consuming complicated simulations in some cases. In this section, I will have a look at both approaches.

1.4.1 Physical models of an accretion disk with corona

Any story about accretion would be incomplete without citing a paper describing the fundamental model of a thin accretion disk, published by Shakura & Sunyaev (1973). The assumption of their model was the prescription for the turbulent stress tensor $t_{r\phi} = \alpha P$, causing transport of the angular momentum outside of the disk and dissipation of gravitational energy in the disk, following the formula:

$$Q_{\text{disk}} = \alpha \Omega P \tag{1.2}$$

where Ω is the angular velocity of the Keplerian orbit at the given radius and P stands for the pressure of the matter, typically assumed as the sum of gas and radiation pressure, and α is the proportionality constant, representing – at the time unknown – viscosity mechanism. There have been numerous derivatives of the α-disk model and many other "prescriptions" assuming different expressions for P have been proposed since (Janiuk & Czerny, 2011; Grzędzielski et al., 2017). Further developments of the analytic or semi-analytic accretion disk models involve accounting for relativistic effects in Schwarzschild metric (Novikov & Thorne, 1973), as well as solutions for very specific physical conditions, such as super-Eddington accretion (Abramowicz, 2005).

Shapiro et al. (1976) extended the model of α-disk by replacing an innermost part of the disk, that in the Shakura & Sunyaev (1973) model would be radiation-pressure dominated by a hot, optically thin flow, where photons and ions are decoupled and gas pressure dominates. The inner region would contribute to the overall spectrum by inverse-Compton scattering of the soft photons by free electrons in the hot region. The spectrum computed from the model yielded a good fit to Cyg X-1 spectrum obtained by *Uhuru* and other X-ray data available at the time. Begelman et al. (1987) evaluated the behavior of such a decoupled hot flow for accretion rates around Eddington rate, the interactions between electron-positron pairs and protons cause cooling of the latter and

cause them to condensate into a disk near the equatorial plane, a potential source of the soft X-ray component. The presence of an optically thick medium so close to the black hole could explain the rapid variability observed in some objects.

Regardless of the model, however, the source of the viscosity was the greatest puzzle in the accretion theory for many years. Eardley & Lightman (1975) proposed a model where a magnetic field flux cell in the disk would be sheared by the disk motion causing stress and angular momentum transfer, and eventually undergo reconnection, splitting into two flux cells. The reconnection would be a natural limiter to the magnetic field growth, and a mechanism of dissipating the magnetic energy into heat (see Coroniti, 1981, for more details about the model). Galeev et al. (1979) expressed a contrary view, claiming that the reconnection within the disk would be ineffective, causing the magnetic field to be amplified and grow until achieving the equipartition. Such a strong field acquires buoyancy and flows away from the midplane of the accretion disk into the corona, heating it in the analogy to the solar corona. The viscosity mechanism was eventually formulated and named Magneto-Rotational Instability (MRI), described by Balbus & Hawley (1991). The next section will discuss it in more detail.

Nakamura & Osaki (1993) proposed a similar, self-consistent model, parametrized by f ratio, where disk and the corona are coupled, both governed by an α-prescription and accrete simultaneously. They note that the mass is stored mostly in the cold disk, but the energy dissipation occurs mostly in the corona, which makes them suspect that the energy transport between the disk and the corona is by magnetic field. This also makes the cold disk stable against radiation pressure instability. They can determine physical variables, such as the surface density of the cold disk, electron temperature, and the optical depth of the hot corona, as well as compute the spectra resulting from their model using a Monte-Carlo Compton scattering model, obtaining spectral index $\alpha \approx 1.2$, corresponding to $\Gamma \approx 2.2$.

Doerrer et al. (1996) use a modified α-prescription by a term accounting for energy loss of turbulent elements in the optically thin regime and relativistic effects of Kerr spacetime are included. They use the Fokker-Planck approximation to treat Comptonization and obtain a highly scattering-dominated photon-starved solution which is optically thick for Compton scattering but optically thin for most other frequencies. They obtain spectra that extend to a higher energy than a simple disk-blackbody would, therefore providing a possible model for the soft X-ray excess observed in AGN.

Merloni (2003) solve the radial structure of an accretion disk assuming that the magneto-rotational instability (MRI) is the source of turbulence and viscosity and that the magnetic field intensity saturates due to buoyant escape. For low viscosities and high accretion rates, they find the classical radiation pressure instability known from α-disk; for high viscosity, however, they obtain a thermally and viscously stable, radiation-pressure dominated solution. They can determine the fraction of the magnetic flux that escapes the disk into the corona, obtaining $0.69 \leq f \leq 1$. Oda et al. (2009) approximated the radial magnetic field advection by parametrizing its radial distribution in the accretion disk, and obtained a family of new solutions for low-β disks, ranging from optically thin to optically thick. Similarly, the new solution appears to be thermally stable and becomes a smooth bridge linking the very low accretion rate regime (RIAF) and extremely high accretion rate regime (slim disk).

Uzdensky (2013) consider a gas-pressure dominated thin disk with MRI operating. They determine a layer within the disk vertical structure where the MRI is still active and generating the field but Parker instability becomes important, therefore flux generated in that zone escapes buoyantly into the corona. This allows them to obtain a simple analytic lower limit for the coronal power fraction $f \approx \beta_0^{1/5}$ where β_0 is the midplane poloidal magnetic beta parameter, parametrizing the model. Their result is significant: an example value $\beta_0 = 20$ yields $f > 0.55$, and a stronger net vertical field will increase that fraction.

Begelman & Pringle (2007) discuss the magnetic disk, where the MRI dynamo produces large-scale toroidal fields until the dynamo quenching criterion described by Pessah & Psaltis (2005), at which point the efficiency of MRI decreases, ceasing any further build-up of the magnetic energy. The solution of the disk operating at the saturation limit has vastly different properties from the Shakura & Sunyaev (1973) solution: the disk thickness is almost independent of the mass of the central object, radius, or the accretion rate; moreover, for high accretion rates, no radiation-pressure instability is present, as the disk is magnetic pressure dominated at almost all radii. Magnetic support also may remove the problem of self-gravitating SMBH disk in regions far away from the black hole, raising the limitation for accretion rates to around the Eddington limit. Begelman et al. (2015) developed further the model, stating equations to solve for the vertical structure of such a magnetically supported disk. They show that in the hard state of XRBs, the MRI may be operating in two independent zones: at the equatorial plane of the disk and in the corona. While the magnetic flux may migrate buoyantly between the zones, matter accretion could occur independently in the disk and the corona. The creation of a second MRI zone in the accreting corona provides a possible explanation for the transition into the hard state and sudden evaporation of the accretion disk.

1.4.2 Numerical simulations of magnetic disks

Since the analytic considerations, searching for the viscosity source in the accretion disks Eardley & Lightman (1975) and Galeev et al. (1979), no tool has revolutionized the field as much as fast computers and numerical modeling of hydrodynamic flows. They allowed to simulate and visualize the process – magneto-rotational instability – MRI (Balbus & Hawley, 1991; Hawley & Balbus, 1991, 1992; Balbus & Hawley, 1992) – that was theorized to occur for years, and yield an answer to that long-standing question what really happens in a magnetized, sheared flow. It is appropriate, that I explore a bit deeper this process and the results of the numerical simulations of accretion.

MRI carries a great resemblance to what was described by Galeev et al. (1979), the simplified description of this phenomenon involving two weakly coupled parcels of fluid in a rotating flow. The shearing in the flow will cause accelerating deformation of the coupled cell; the weak coupling force will transfer the angular momentum between the two. The faster parcel will lose the angular momentum and descend into a lower orbit, while the slower parcel will gain the angular momentum and climb to a higher orbit. Globally, the angular momentum will be transferred outward in the disk, which means that MRI acts as a mechanism of viscosity. This process also breaks down an initially laminar flow into a turbulent flow.

To initiate the MRI, only a very weak field is needed, and has even been shown to operate in simulations that contain no net poloidal field (Davis et al., 2010). The theory predicts that the perturbation growth rate is only dependent on the Keplerian angular velocity Ω, and – importantly – independent on the magnetic field strength. The other way around, this process acts as a dynamo, converting the kinetic energy of the turbulent gas into magnetic flux (Hawley et al., 1996). The growth of the initially weak magnetic field is constant until saturation when it reaches $\beta = P_{\rm rad}/P_{\rm mag} \approx 10 - 100$.

The intensity of the dynamo, and hence the magnetization of the resulting disk, increases as the poloidal component of the magnetic field becomes stronger, eventually killing the MRI and resulting in Magnetically Arrested Disk (Begelman et al., 2022; Bai & Stone, 2013; Pessah & Psaltis, 2005).

The dynamo causes the growth of a large-scale, turbulent, but on average coherent toroidal component of the field in the disk. Due to buoyancy, this field escapes the disk body, and the shearing box simulations suggest that a new field with opposite polarity starts to be created, as presented in Fig. 1.12 (Brandenburg et al., 1995; Simon et al., 2011). Such magnetic field polarity

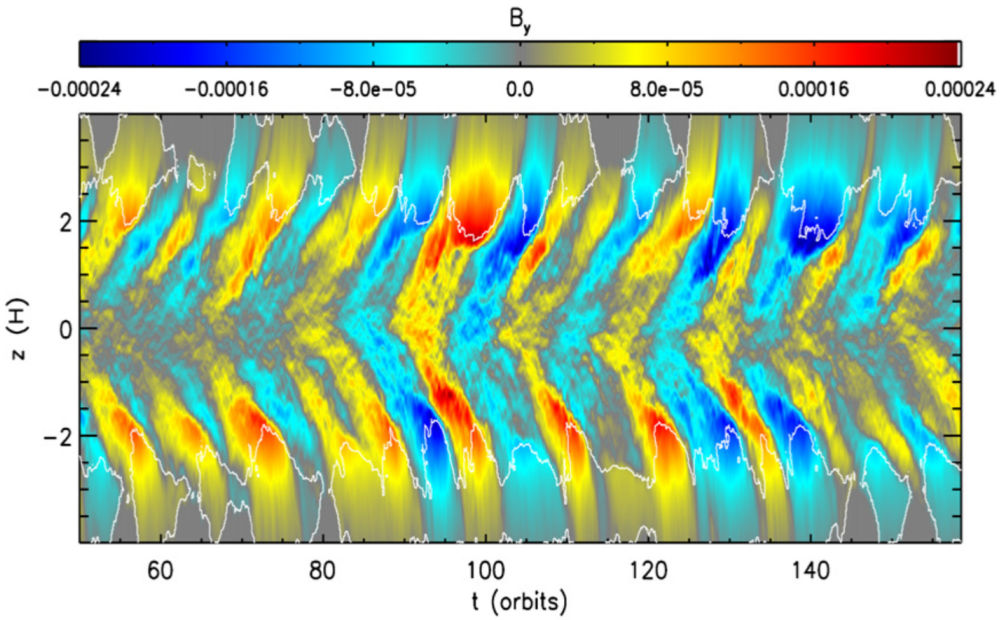

Figure 1.12: The longitudinal component of the magnetic field averaged over horizontal planes and plotted concerning position above the disk midplane (z) and simulation time expressed in orbits. The buoyant escape of the magnetic field from the disk can be seen, as well as "the butterfly pattern" caused by the periodic reversals of field polarity. Reprinted from Simon et al. (2011).

reversal occurs around every 10 orbits, but this number depends on the magnetic parameter β and seems to be more frequent for less magnetized disks (Salvesen et al., 2016). Since the sheets between the reversed polarity regions are the sites for magnetic reconnection, more thermal energy is released within the disk (Begelman et al., 2015). Although not as perfectly regular as in the shearing box setup, global simulations suggest that this behavior does persist in three-dimensional setup (Rodman & Reynolds, 2024).

The creation of a significant magnetic field from an almost zero seed field is obviously very important since not only plays a large part in the viscosity mechanism but also contributes to the pressure structure. The inclusion of the magnetic pressure support in the disk structure may stabilize the disk and alleviate the most common instability in the Shakura-Sunyaev model which is radiation pressure instability (Begelman & Pringle, 2007; Merloni, 2003).

The magnetic field, especially the presence of the poloidal component, is also an important part of the wind-launching mechanism (Jacquemin-Ide et al., 2021). The field is rooted in the disk and pulled due to the rotation. The magnetocentrifugal force exerted on the matter causes the wind to launch. Conversely, these magnetic winds not only carry away a portion of the matter but also very effectively transmit the angular momentum outwards. Due to the effective braking of the disk by the magnetic field, a layer above the disk forms where the accretion is very efficient, so-called "accreting corona", while within the disk body, the accretion of the matter is virtually zero, or even a slight outflow is observed (Zhu & Stone, 2018). This is perhaps the greatest paradigm shift from the traditional optically thick and geometrically thin disk model, which is consistent with observational findings of the power required to sustain a warm corona (Haardt & Maraschi, 1991; Petrucci et al., 2018).

Stronger magnetic field increases the accretion rate while lowering the disk density, which is beneficial for photon reprocessing (Mishra et al., 2020). The simulations show that the accretion disk may become truncated, but rather than disappearing completely, it evaporates into a clumpy, two-phase medium, where the hot and cold phases coexist (Liska et al., 2022). Finally, for the

sub-Eddington accretion, when the radiation pressure becomes dominant, the puffy disk solution emerges, which contains a diffuse layer covering the disk. The puffy disk produces a strongly beamed radiation, and the produced synthetic spectra can be fit with `nthcompt` model yielding spectral index around $\Gamma \approx 3$ (Lančová et al., 2019, 2022; Wielgus et al., 2022).

1.5 Thermal Instability

To determine the temperature of the gas, one must solve the thermal balance equation containing heating components on one side and the radiative cooling function on the other. This equation typically has a single solution, and the cooling rate should have a positive temperature derivative. The intuition would suggest that the increase in power input will increase the temperature, which in turn will cause greater energy losses, and the system will find a new point of balance.

Occasionally, when different physical processes are involved than a simple thermal emission, there could be more than one point of equilibrium. Assuming a continuous dependence of energy losses from temperature, that would usually mean three or more solutions: the hottest and the coolest solution would be stable, while the middle would be unstable. For that middle solution, any deviation from the equilibrium would cause a runaway reaction: the temperature increasing (decreasing) would cause the cooling rate to decrease (increase), causing a buildup (loss) of internal energy and further increase (decrease) in temperature until the system reaches a new, stable point of equilibrium.

This condition, which I will call thermal instability (TI) from now onwards, can occur in the medium if under given conditions the cooling rate does not increase with temperature, which, in its simplest form, I can write down as follows:

$$\frac{d\Lambda_{\rm net}}{dT} = \frac{d\Lambda}{dT} - \frac{d\mathcal{H}}{dT} < 0 \tag{1.3}$$

where Λ is sum of all cooling terms, and $\mathcal{H}$ is the sum of all heating terms and $\Lambda_{\rm net}$ is the net cooling function.

The foundations for the theory of thermal instability have been laid down by Parker (1953), who was mostly interested in its application for the solar corona. He developed a general condition for the instability, and by applying it to highly-ionized hydrogen atmosphere, he found it to be most likely thermally unstable. Zanstra (1955) made further developments towards solar chromosphere and corona, while Weymann (1960) generalized this in the context of dwarf chromospheres. Field (1965) expanded this theory considerably, by including, among other, the finite speed of sound, thermal conduction, and magnetic field, and made predictions for the solar corona, planetary nebulae, and interstellar and intra-galactic medium.

In a fundamental paper, Krolik et al. (1981) analyzed the energy balance of a cloud system in equilibrium, including heating by photoionization, Compton scattering, thermal conduction, and friction. They were able to compute the dependence of $\Lambda_{\rm net}$ on temperature of the medium, for models that assume various illumination spectra, chemical compositions et cetera. Fig. 1.13 presents the net cooling function computed for different values of the ionization parameter Ξ, which is defined as

$$\Xi = \frac{F_{\rm ion}}{cP_{\rm gas}} \tag{1.4}$$

where $P_{\rm gas}$ is gas pressure and $F_{\rm ion}$ is the ionizing radiation flux. The above quantity has been used many times to describe thermal equilibrium between radiative cooling and heating of the gas, by the relation $T(\Xi)$, where temperature is computed from the radiative energy balance. For positive value of $dT/d\Xi$ matter is thermally stable, while for a negative value of $dT/d\Xi$ - the instability occurs. For very large Ξ only Compton processes are important, but with the decrease of

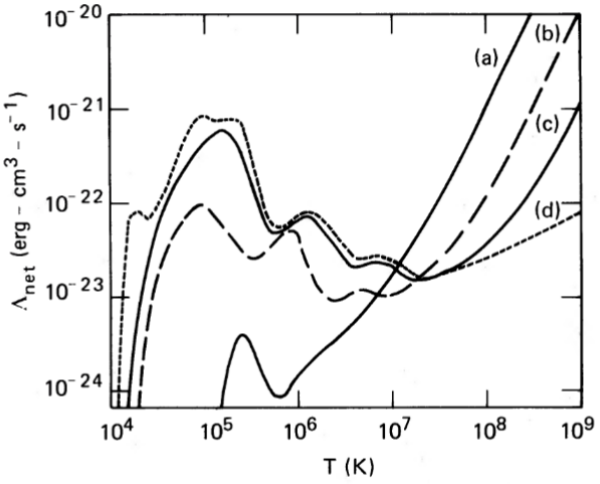

Figure 1.13: Net cooling rate as a function of gas temperature for four values of the ionization parameter: (a) $\Xi = 10$, (b) $\Xi = 1$, (c) $\Xi = 0.1$, (d) $\Xi = 0$. (Krolik et al., 1981)

ionization parameter, followed by decrease of temperature, the bremsstrahlung process becomes more important, and finally cannot overwhelms photoionization making the gas thermally unstable. The minimum value of ionization parameter when high temperature equilibrium can be achieved has been recognized by the base of the corona in many of papers concerning two-slab disk/corona geometry (Krolik et al., 1981; Haardt & Maraschi, 1991; Różańska & Czerny, 2000).

So far, I have not mentioned the particular geometry of the situation. In accretion theory, stability analysis has found most application in studying the stability of an accretion disk, or a coupled disk-corona system (Shakura & Sunyaev, 1976; Nakamura & Osaki, 1993; Kusunose & Mineshige, 1994). In these works, the division between disk and corona was arbitrary and no vertical structure was computed. Other works were focused on the structure and stability of the disk-corona boundary although primarily they assumed conditions where strong illumination by hard X-ray is the main source of the heating, rather than internal dissipation of energy. Rozanska & Czerny (1996) followed by Różańska (1999) showed that an illuminated accretion disk atmosphere shows a discontinuity at the disk-corona boundary, which is unstable when perturbed.

In the case of the optically thick atmosphere of an accretion disk, direct illumination by ionizing radiation can only penetrate up to optical depths in the order of unity, therefore it ceases to be the major energy input that could destabilize the equilibrium. Instead, one has to compute the instability condition from the definition (1.3). We can generalize the energy balance condition for the instability if one can express the cooling function Λ as a function of temperature. For simplicity in this definition, we assume that the heating term $\mathcal{H}$ is temperature-invariant, although this can be very easily incorporated into the equation below. With the above assumption, the condition for instability reads

$$\mathcal{L}_{\rm rad} \equiv \frac{d\ln\Lambda}{d\ln T} = \frac{\partial\ln\Lambda}{\partial\ln T} - a\frac{\partial\ln\Lambda}{\partial\ln\rho} \leq 0, \tag{1.5}$$

where a is a numerical constant, depending on the constraining regime:

- $a = 1$ for $\delta P_{\rm gas} = 0$ (isobaric)
- $a = 0$ for $\delta\rho = 0$ (isochoric)
- $a = \frac{\beta}{\beta+2}$ for $\delta P_{\rm gas} + \delta P_{\rm mag} = 0$ where $\beta = P_{\rm gas}/P_{\rm mag}$ (Field, 1965)

The above considerations are aproprate for stationary solution and do not take into account the mass transfer due to the radiation/magnetic pressure. Nevertheless, they allow us to estimate

the need for two-phase medium caused by thermal instability which existence is proven observationally in several sources (Różańska et al., 2014; Borkar et al., 2021, and references therein).

1.6 Goal of the thesis

This thesis is devoted to exploring the origin of the soft X-ray spectral component in the context of developing new code for computing theoretical models of the gas structure and predicting the physical mechanism responsible for the emission of the soft X-ray excess, commonly observed in accreting BHs - those with large BH masses as active galactic nuclei (AGN), and those with stellar mass. Note, that I do not consider accreting NSs, since the emission from the NS surface appears exactly in the range of the SXE, and strongly interferes with our main scientific goal.

In this thesis, I developed new numerical model to study the warm corona/accretion disk structure in accreting black holes across the masses. The most challenging task was to invent the computational scheme in order to pass across thermally unstable regions in the gas with magnetic heating and therefore magnetic pressure accounted in the hydrostatic balance. For this thesis, the most important radiative and possibly mechanical interaction between two: the hot and cold regions of accreting BHs, is the appearance of the SXE in the spectra of those sources. I aimed to study here what physical mechanism is responsible for the production of this common feature observed in many sources. I postulate that the soft corona, heated by magnetic reconnection, can arise above an accretion disk and physically form a stable optically thick region, cooled by radiative processes. The structure of such a warm corona, which is founded in the physics of accretion, is the main result of our work. Finally, I attempt to compute the spectrum from the region where the SXE may be created.

The structure of this dissertation is as follows:

- In the current chapter, Introduction, I present the background story, including SXE observations; I discuss the possible interpretation of this emission, and I present the recent developments in simulations of radiative processes and accretion flows in such regions. I detail the motivation of our work as well as include analysis and conclusions drawn from all my papers.

- Paper I (Gronkiewicz & Różańska, 2020) describes our model of the magnetically supported disk, above which a warm corona may naturally arise. A computational algorithm and full numerical method are presented in this paper. The model is applied to stellar-mass black holes, and I present results comparing them to some of the observations.

- Paper II (Gronkiewicz et al., 2023) expands the model by incorporating more physics into it, and applies it to supermassive black holes. I also perform a more extensive comparison to a sample of observations and discuss in-depth how the thermal instability affects the SXE.

- In Paper III (Petrucci et al., 2020) I evaluate the SXE spectrum using a photoionization radiative transfer code TITAN and a Monte Carlo code NOAR that allows for accounting for the effects of Comptonization.

1.7 Conclusions

This thesis is dedicated to researching the warm corona scenario as a possible explanation for the observed soft X-ray excess in compact objects. To differentiate the mechanism responsible for soft X-ray excess from other proposed scenarios, most significantly – relativistically blurred reflection – both physical plausibility and consistency with observations must be demonstrated. For this

reason, part of the work was conducted from the perspective of physical modeling of accretion flow (Chapters 2 and 3) to verify whether warm corona can even form above an accretion disk assuming a consistent physical model, while part of the work focused more on radiative transfer (Paper III) to demonstrate spectral appearance of the warm corona which is the most important aspect helping to prove or reject model based on observations.

In my work dedicated to modeling the accretion flow, I solve the model of the magnetically supported disk (MSD) introduced by Begelman et al. (2015) which derives the equation governing the vertical structure of a thin accretion disk threaded by a toroidal magnetic field in hydrostatic equilibrium. The energy transport in the disk is based on the assumption of the outflow of the toroidal flux from the equatorial plane, causing heating of the disk atmosphere. I extended the model by incorporating radiative transfer, heating and cooling balance, and equation of state of the ideal gas, as well as integrating into the equation system the effect of shutoff of the MRI dynamo that was described in the original paper. This development of the model required us to implement a code that employs a relaxation technique to reliably obtain the solution of the system of nonlinear ordinary differential equations.

The model is applied to two cases: stellar-mass black hole and supermassive black hole. In either case, I was able to find stable solutions for the vertical structure of the disk-corona system. By computing this structure for many parameters (such as accretion rate, magnetization, and distance from the central body), I was able to study the behavior of the system. For all of the studied cases, some type of corona is observed in the structured atmosphere: that is, as I go from large optical depths toward the surface, the temperature of the gas reaches its minimum and then an inversion occurs when it starts to increase again. Some basic parameters of the corona, such as the optical depth of the temperature inversion and the averaged temperature are computed for each model. The stellar-mass black hole model (described in Paper I), yields values of forementioned parameters as $\tau \approx 10$ and $kT \approx 10$ keV, while for supermassive black hole (Paper II) the obtained parameters are $\tau \approx 40$ and $kT \approx 1$ keV. These are consistent with observations of the warm Comptonization in accreting objects and I managed to obtain them for vastly different scales using the same model. In the magnetically supported disk, the magnetic field has a double role: provides support, helps to keep the density low, and constitutes the main heating mechanism of the corona. The aforementioned values were obtained when the accretion rate and magnetic field strength in the disk were extreme, being in the range $0.1 < \dot{m} < 1$ and $P_{\rm mag} \approx P_{\rm gas} + P_{\rm rad}$. Outside of that subspace, a hot and optically thin corona was formed but not the warm and optically thick corona. Indeed, by synthesizing a population of models, I showed that high magnetization is required to reproduce the distribution of observable parameters of sources that exhibit strong soft X-ray excess.

In another part of this work (Paper III), I studied the problem of radiation emitted by the warm coronae. I assumed plane-parallel atmospheres located on top of an accretion disk. Each of our atmosphere models is constant-density and fixed optical depth. In addition, I considered illumination by the hard X-ray power law radiation on one side and blackbody radiation originating from the accretion disk on the other side of the atmosphere, which should match as much as possible real conditions experienced by the warm corona. I solved the radiative transfer problem using codes TITAN and NOAR (Dumont et al., 2000). TITAN is a classic radiative transfer code, which employs the Accelerated Lambda Iteration (ALI) method and provides us with a solution for radiation intensity and matter temperature and ionization structure, while NOAR is a Monte-Carlo code that enables us to compute the Comptonized spectrum of the radiation, using the structure of the atmosphere computed by TITAN. I obtained grids of models, parametrized by corona optical depth $\tau_{\rm es}$, density $n_{\rm H}$, ionization parameter ξ_0 versus corona dissipation power parameter χ, where $\chi = 0$ corresponds to passive corona, $\chi = 1$ to active corona and passive disk and $\chi > 1$ would represent patches of strongly dissipative corona over a passive disk. Comparing the obtained

temperature of the warm corona as well as spectral index Γ, I was able to compare solutions in the whole parameter space to the values determined from observations of the Soft X-ray Excess by fitting phenomenological spectral models. The parameter subspace that this constrained is consistent with a strongly dissipative patchy corona $1 < \chi < 1.5$ with large optical thickness $\tau \approx 20$. Spectra obtained from our computations had very few features, particularly no absorption lines were present due to high ionization. Compton cooling was a dominant mechanism determining the obtained temperature of the atmosphere, which is consistent with previous findings, but internal heating is crucial to obtain consistent solutions which are also in agreement with observations.

Two different approaches I conducted in the study of warm-corona as an explanation of the soft X-ray excess have some commonalities and some differences. I established in both studies that Comptonization must be the dominant radiative process to obtain both a stable structure of the warm corona and agreement with the observations. Whenever other types of opacity (bremsstrahlung or ionization processes) come into play, the effective optical depth for the photons is limited altering the output spectral shape. At a constant pressure, the matter also may not be stable concerning thermal collapse. Lower density and high temperature helps to keep the atmosphere in a Comptonization-dominated regime. In both approaches, the limit to the density is in very good agreement, as it is imposed purely by opacity. Both approaches showed that high power output is needed in the corona to sustain the favorable conditions for warm Comptonization. In our study of the consistent disk-corona structure model, I concluded that event of extremely high magnetization the ratio of power emitted in the corona to the total power χ can reach up to around half. In other words, I was not able to obtain a solution where the disk is passive and entire energy dissipation takes place in the corona. However, this is the result I got in our study focused on the radiation spectra. This could be considered the most meaningful discrepancy that I have encountered in this work. Nevertheless, most of the conclusions are consistent despite two entirely different approaches to modeling the system.

1.8 Final remarks and future steps

The model of the magnetically supported accretion disk (MSD) by Begelman et al. (2015), which I completed with some basic radiative transfer, is quite simple in the age of computers that allow numerical simulations to run with simplified radiative transfer and general relativity effects on very dense computational grids. Nevertheless, our model allowed us to draw some surprisingly interesting conclusions that are consistent with works that are more computationally advanced.

As I discussed in the introduction to this thesis, two competing models, the reflection model (Section 1.3.2) and the warm corona model (Section 1.3.3), are currently a topic of scientific discussion regarding the soft X-ray excess origin. There is ample evidence for each of the proposed models. They need not necessarily be mutually exclusive. The question is not really which of them is correct, since almost certainly both processes contribute to the outgoing spectrum, but rather what the ratio of that contribution is, and how can we understand the process governing both? This has been recently observed for changing-looks AGNs, where objects transitioned from reflection-like to Comptonization-like within years (Pal et al., 2021).

Warm Comptonization obviously produces a very featureless spectrum, especially when the temperature of the warm skin is sufficient to provide compatibility with the observations (see Paper III), therefore a separate reflection component is usually needed when fitting the X-ray data. Both the traditional approach in fitting spectra (Lohfink et al., 2012; Porquet et al., 2021) as well as recent models that include both Comptonization and reflection (for example Xiang et al., 2022) seem to indicate that some contribution from each component is required to accurately describe the spectrum. If indeed we follow the model of Done et al. (2012), and the warm corona covers only the inner part of the disk, which is on the verge of evaporation (either by the radiation

pressure or strong magnetic field inflating the disk), that part of the disk atmosphere would be highly ionized and reflection features would not be visible. Therefore, we could be dealing with a whole spectrum of objects, one extreme being a hot and thin corona illuminating the partially ionized skin of a dense and cold disk (reflection component dominating) and another extreme would be a disk with a warm, completely ionized, magnetically heated Comptonizing skin, with very weak lines and other reflection features (Comptonization component dominating).

This aligns with what we ascertain from the other side of the study – the simulations for moderate accretion rates. A weak magnetic field yields a rather cool disk. A stronger magnetic field will decrease the density of the matter while increasing the accretion rate (higher infall velocity) within the coronal region, as demonstrated both in simulations by Mishra et al. (2020) and in our simple model (Paper II). Furthermore, a stronger magnetic field will cause enhanced corona heating. The strongest field will cause the disk to become magnetically arrested – a MAD, in which case we expect disk truncation and an outflow or a jet, preceded by a transition area where both phases mix, see Liska et al. (2022). Increasing the accretion rate to sub-Eddington will also induce the coronal accretion and create favorable conditions for the warm Comptonization, but for very high accretion rates the radiation is funneled and expected to be seen only for low inclination angles (Wielgus et al., 2022). Of course, how strong the disk magnetic field is, and as a result, how close to the black hole and how large each of the zones is (arrested disk, strongly magnetized disk, weakly magnetized disk), is currently believed to depend on the net poloidal field.

How do these studies compare to the hard truth – the observations? Mrk 509 (Singh et al., 1985; Kaastra et al., 2011) is a high-luminosity extragalactic X-ray source, extensively studied. From Earth, we see it almost face-on and we can also observe outflows from the nucleus. Interestingly, the iron Kα spectral line analysis lacks reflection features from the inner part of the disk, despite high luminosity, which would indicate a lack of a dense accretion disk up to the very ISCO (or even hundreds of gravitational radii, according to Ponti et al., 2013). This would be consistent, for one, with a situation where both a reasonably strong magnetic field and a good mass influx (like in a puffy disk) is present. Generous field could help maintain very efficient coronal accretion despite low density, depositing enough energy to sustain the warm comptonization of the disk hidden under the warm halo and suppress some of the reflection features in the innermost, hottest and most magnetized parts of the flow. Perhaps, to some degree, disk evaporation could be present, as long as the accretion throughput is sustained, which could aid in driving the outflow that we are able to observe in Mrk 509. Wielgus et al. (2022) determined the spectral slope index $\Gamma \approx 2.8$ and $kT \approx 15$keV for their puffy disk at $\dot{m} = 0.6$ around a stellar mass black hole, which is only slightly steeper compared to $\Gamma_{\rm wc} \approx 2.5$ with $kT \approx 0.5$keV for the warm component determined by Petrucci et al. (2013) (and the average Γ for AGN is closer to 3 on average, derived from a larger sample studied by Petrucci et al.). Unfortunately, comparing any values for such a difference in accretor mass cannot be performed directly, since radiative effects are usually not easily scalable. However, one could ask an interesting question, which could be answered by future simulations of SMBH accretion: Is Mrk 509 a good candidate for a puffy disk?

Of course, this source is only a single example. Many more studies are needed, namely: cross-sectional analyses over many objects (such as Jin et al., 2012; Petrucci et al., 2018), models that can treat the subtle interplay between photoionization and Comptonization (an example being Xiang et al., 2022), and perhaps most importantly, realistic modeling of the radiation based on the output of modern simulations (the likes of Wielgus et al., 2022).

As it is discussed in Paper II, in AGN the conditions required by the warm corona coincide with conditions that could trigger a local coronal thermal instability (LCTI). Particularly, the observed optical depth of the warm corona is for some part of the sample of Jin et al. (2012) well

predicted by the optical depth of the LCTI, which can be characterized by the critical density:

$$\rho_{\text{crit}}/m_{\text{H}} = 2.87 \cdot 10^{16} \left(\frac{T_{\text{rad}}}{10^6 \text{ K}} \right)^{9/2} \text{cm}^{-3} \tag{1.6}$$

That would mean that for some objects, the warm corona is unstable and might go undergo abrupt changes on a thermal timescale. Tripathi et al. (2021) indeed observed in IC 4329A that the warm comptonization component, which almost completely explains the SXE for this particular object, goes through rapid changes over half a year, the shortest observed variability timescale being around the thermal timescale for the disk. This variability could not be explained by changes in the disk luminosity, because the viscous timescale is much longer. Interestingly, they determined the accretion rate to be $\dot{m} \approx 0.06$ which is within the range predicted in Paper II for thermal instability operation ($\dot{m} < 0.2$).

Would such instability occur in Mrk 509? Unlikely so, since its variability timescale is slow therefore it certainly comes as a result of accretion rate changes (Mehdipour et al., 2011), but also its higher accretion rate $\dot{m} > 0.2$ makes it sit comfortably in the regime that I predict should be unaffected by the instability (although based only on free-free opacity). Interestingly, Kubota & Done (2018) noted that the transition between the warm corona and cold disk for three analyzed objects appeared to occur in the disk where the ultraviolet opacity peaked. Would we see a clear split in the timing data and relativistic reflection features between the objects on both sides of our criterion? This is another interesting question to be explored.

What this thesis aimed to achieve is to reduce the complexity of lengthy MHD simulations into a simple and extensible model that would include basic thermal properties of the matter. On the way to this goal, the interesting puzzle of hypothetical coronal instabilities was barely touched. It attempted to draw some connections between accretion disk models and X-ray spectroscopy, on the journey to understand the true physical mechanism behind the soft X-ray excess.

Bibliography

Abarca D., Parfrey K., Kluźniak W., 2021, ApJ, 917, L31

Abramowicz M. A., 2005, in Merloni A., Nayakshin S., Sunyaev R. A., eds, Growing Black Holes: Accretion in a Cosmological Context. pp 257–273 (arXiv:astro-ph/0411185), doi:10.1007/11403913_49

Arnaud K. A., 1996, in Jacoby G. H., Barnes J., eds, Astronomical Society of the Pacific Conference Series Vol. 101, Astronomical Data Analysis Software and Systems V. p. 17

Arnaud K. A., et al., 1985, MNRAS, 217, 105

Bachetti M., et al., 2014, Nature, 514, 202

Bai X.-N., Stone J. M., 2013, ApJ, 767, 30

Balbus S. A., Hawley J. F., 1991, ApJ, 376, 214

Balbus S. A., Hawley J. F., 1992, ApJ, 400, 610

Ballantyne D. R., 2020, MNRAS, 491, 3553

Ballantyne D. R., Xiang X., 2020, MNRAS, 496, 4255

Bambi C., et al., 2021, Space Sci. Rev., 217, 65

Bechtold J., Czerny B., Elvis M., Fabbiano G., Green R. F., 1987, ApJ, 314, 699

Beckmann V., Shrader C. R., 2012, Active Galactic Nuclei

Begelman M. C., Pringle J. E., 2007, MNRAS, 375, 1070

Begelman M. C., Sikora M., Rees M. J., 1987, ApJ, 313, 689

Begelman M. C., Armitage P. J., Reynolds C. S., 2015, ApJ, 809, 118

Begelman M. C., Scepi N., Dexter J., 2022, Monthly Notices of the Royal Astronomical Society, 511, 2040

Belloni T. M., 2010, in Belloni T., ed., , Vol. 794, Lecture Notes in Physics, Berlin Springer Verlag. Springer, p. 53, doi:10.1007/978-3-540-76937-8_3

Borkar A., et al., 2021, MNRAS, 500, 3536

Bourne M. A., Nayakshin S., 2013, MNRAS, 436, 2346

Brandenburg A., Nordlund A., Stein R. F., Torkelsson U., 1995, ApJ, 446, 741

Brunner H., Mueller C., Friedrich P., Doerrer T., Staubert R., Riffert H., 1997, A&A, 326, 885

Churazov E., Gilfanov M., Revnivtsev M., 2001, MNRAS, 321, 759

Colbert E. J. M., Mushotzky R. F., 1999, ApJ, 519, 89

Corbel S., Coriat M., Brocksopp C., Tzioumis A. K., Fender R. P., Tomsick J. A., Buxton M. M., Bailyn C. D., 2013, MNRAS, 428, 2500

Coroniti F. V., 1981, ApJ, 244, 587

Corral A., Della Ceca R., Caccianiga A., Severgnini P., Brunner H., Carrera F. J., Page M. J., Schwope A. D., 2011, A&A, 530, A42

Crummy J., Fabian A. C., Gallo L., Ross R. R., 2006, MNRAS, 365, 1067

Czerny B., Elvis M., 1987, ApJ, 321, 305

Czerny B., Zycki P. T., 1994, ApJ, 431, L5

Davidson K., Ostriker J. P., 1973, ApJ, 179, 585

Davis S. W., Stone J. M., Pessah M. E., 2010, ApJ, 713, 52

De Marco B., Ponti G., Cappi M., Dadina M., Uttley P., Cackett E. M., Fabian A. C., Miniutti G., 2013, MNRAS, 431, 2441

Dewangan G. C., Griffiths R. E., Dasgupta S., Rao A. R., 2007, ApJ, 671, 1284

Ding N., et al., 2021, A&A, 650, A183

Doerrer T., Riffert H., Staubert R., Ruder H., 1996, A&A, 311, 69

Done C., Nayakshin S., 2007, MNRAS, 377, L59

Done C., Gierliński M., Kubota A., 2007, A&A Rev., 15, 1
Done C., Davis S. W., Jin C., Blaes O., Ward M., 2012, MNRAS, 420, 1848
Dove J. B., Wilms J., Begelman M. C., 1997a, ApJ, 487, 747
Dove J. B., Wilms J., Maisack M., Begelman M. C., 1997b, ApJ, 487, 759
Dumont A.-M., Abrassart A., Collin S., 2000, A&A, 357, 823
Eardley D. M., Lightman A. P., 1975, ApJ, 200, 187
Ezhikode S. H., Shyam Prakash V. P., Dewangan G. C., Mathew B., 2023, Astronomische Nachrichten, 344, e20230042
Fabian A. C., Miniutti G., 2005, arXiv e-prints, pp astro–ph/0507409
Fabian A. C., Miniutti G., Iwasawa K., Ross R. R., 2005, MNRAS, 361, 795
Fabian A. C., Lohfink A., Kara E., Parker M. L., Vasudevan R., Reynolds C. S., 2015, MNRAS, 451, 4375
Falcke H., Körding E., Markoff S., 2004, A&A, 414, 895
Field G. B., 1965, ApJ, 142, 531
Freeman P., Doe S., Siemiginowska A., 2001, in Starck J.-L., Murtagh F. D., eds, Society of Photo-Optical Instrumentation Engineers (SPIE) Conference Series Vol. 4477, Astronomical Data Analysis. pp 76–87 (arXiv:astro-ph/0108426), doi:10.1117/12.447161
Galeev A. A., Rosner R., Vaiana G. S., 1979, ApJ, 229, 318
Gallo E., Fender R. P., Pooley G. G., 2003, MNRAS, 344, 60
Gallo E., Fender R., Kaiser C., Russell D., Morganti R., Oosterloo T., Heinz S., 2005, Nature, 436, 819
García J. A., et al., 2019, ApJ, 871, 88
Gierliński M., Done C., 2004a, MNRAS, 347, 885
Gierliński M., Done C., 2004b, MNRAS, 349, L7
Gierliński M., Done C., 2006, MNRAS, 371, L16
Gierliński M., Zdziarski A. A., Poutanen J., Coppi P. S., Ebisawa K., Johnson W. N., 1999, MNRAS, 309, 496
Gierliński M., Middleton M., Ward M., Done C., 2008, Nature, 455, 369
Gronkiewicz D., Różańska A., 2020, A&A, 633, A35
Gronkiewicz D., Różańska A., Petrucci P.-O., Belmont R., 2023, A&A, 675, A198
Grzędzielski M., Janiuk A., Czerny B., Wu Q., 2017, A&A, 603, A110
Haardt F., Maraschi L., 1991, ApJ, 380, L51
Hagen S., Done C., 2023, MNRAS, 525, 3455
Hagino K., Odaka H., Done C., Gandhi P., Watanabe S., Sako M., Takahashi T., 2015, MNRAS, 446, 663
Hawley J. F., Balbus S. A., 1991, ApJ, 376, 223
Hawley J. F., Balbus S. A., 1992, ApJ, 400, 595
Hawley J. F., Gammie C. F., Balbus S. A., 1996, ApJ, 464, 690
Homan J., Wijnands R., van der Klis M., Belloni T., van Paradijs J., Klein-Wolt M., Fender R., Méndez M., 2001, ApJS, 132, 377
Homan J., Buxton M., Markoff S., Bailyn C. D., Nespoli E., Belloni T., 2005, ApJ, 624, 295
Ishibashi W., Courvoisier T. J. L., 2010, A&A, 512, A58
Jacquemin-Ide J., Lesur G., Ferreira J., 2021, A&A, 647, A192
Jagoda N., Austin G., Mickiewicz S., Goddard R., 1972, IEEE Transactions on Nuclear Science, 19, 579
Janiuk A., Czerny B., 2011, MNRAS, 414, 2186
Jiang J., et al., 2019, MNRAS, 489, 3436
Jin C., Ward M., Done C., Gelbord J., 2012, MNRAS, 420, 1825
Jin C., Done C., Ward M., 2020, MNRAS, 495, 3538
Jin C., Done C., Ward M., 2021, MNRAS, 500, 2475
Kaastra J. S., Mewe R., Nieuwenhuijzen H., 1996, in UV and X-ray Spectroscopy of Astrophysical and Laboratory Plasmas. pp 411–414
Kaastra J. S., et al., 2011, A&A, 534, A36

Kajava J. J. E., Poutanen J., 2009, MNRAS, 398, 1450
Kara E., Alston W. N., Fabian A. C., Cackett E. M., Uttley P., Reynolds C. S., Zoghbi A., 2016, MNRAS, 462, 511
Keek L., Ballantyne D. R., 2016, MNRAS, 456, 2722
Kewley L. J., Groves B., Kauffmann G., Heckman T., 2006, MNRAS, 372, 961
King A. R., 2002, MNRAS, 335, L13
King A., Lasota J.-P., Middleton M., 2023, New A Rev., 96, 101672
Kitaki T., Mineshige S., Ohsuga K., Kawashima T., 2021, PASJ, 73, 450
Koratkar A., Blaes O., 1999, PASP, 111, 1
Krolik J. H., McKee C. F., Tarter C. B., 1981, ApJ, 249, 422
Kruper J. S., Urry C. M., Canizares C. R., 1990, ApJS, 74, 347
Kubota A., Done C., 2018, MNRAS, 480, 1247
Kusunose M., Mineshige S., 1994, ApJ, 423, 600
Laha S., Dewangan G. C., Kembhavi A. K., 2014, MNRAS, 437, 2664
Lančová D., et al., 2019, ApJ, 884, L37
Lančová D., Yilmaz A., Wielgus M., Dovčiak M., Straub O., Török G., 2022, arXiv e-prints, p. arXiv:2209.03713
Liska M. T. P., Musoke G., Tchekhovskoy A., Porth O., Beloborodov A. M., 2022, ApJ, 935, L1
Lohfink A. M., Reynolds C. S., Miller J. M., Brenneman L. W., Mushotzky R. F., Nowak M. A., Fabian A. C., 2012, ApJ, 758, 67
Madej J., Różańska A., 2000a, A&A, 356, 654
Madej J., Różańska A., 2000b, A&A, 363, 1055
Madej J., Różańska A., Majczyna A., Należyty M., 2017, MNRAS, 469, 2032
Magdziarz P., Blaes O. M., Zdziarski A. A., Johnson W. N., Smith D. A., 1998, MNRAS, 301, 179
Makishima K., Maejima Y., Mitsuda K., Bradt H. V., Remillard R. A., Tuohy I. R., Hoshi R., Nakagawa M., 1986, ApJ, 308, 635
Masnou J. L., Wilkes B. J., Elvis M., McDowell J. C., Arnaud K. A., 1992, A&A, 253, 35
Mehdipour M., et al., 2011, A&A, 534, A39
Merloni A., 2003, MNRAS, 341, 1051
Merloni A., Heinz S., di Matteo T., 2003, MNRAS, 345, 1057
Meyer-Hofmeister E., Liu B. F., Meyer F., 2012, A&A, 544, A87
Middleton M., Done C., Ward M., Gierliński M., Schurch N., 2009, MNRAS, 394, 250
Miniutti G., Piconcelli E., Bianchi S., Vignali C., Bozzo E., 2010, MNRAS, 401, 1315
Mishra B., Begelman M. C., Armitage P. J., Simon J. B., 2020, MNRAS, 492, 1855
Mondal S., Różańska A., De Marco B., Markowitz A., 2021, MNRAS, 505, L106
Muñoz-Darias T., Motta S., Belloni T. M., 2011, MNRAS, 410, 679
Müller-Sánchez F., Comerford J., Stern D., Harrison F. A., 2016, ApJ, 830, 50
Nakamura K., Osaki Y., 1993, PASJ, 45, 775
Nomura M., Ohsuga K., 2017, MNRAS, 465, 2873
Novikov I. D., Thorne K. S., 1973, in Black Holes (Les Astres Occlus). pp 343–450
Oda H., Machida M., Nakamura K. E., Matsumoto R., 2009, ApJ, 697, 16
Padovani P., et al., 2017, A&A Rev., 25, 2
Pal M., et al., 2021, Journal of Astrophysics and Astronomy, 42, 81
Parker E. N., 1953, ApJ, 117, 431
Pessah M. E., Psaltis D., 2005, ApJ, 628, 879
Petrucci P. O., et al., 2000, ApJ, 540, 131
Petrucci P.-O., et al., 2013, A&A, 549, A73
Petrucci P. O., Ursini F., De Rosa A., Bianchi S., Cappi M., Matt G., Dadina M., Malzac J., 2018, A&A, 611, A59

Petrucci P. O., et al., 2020, A&A, 634, A85
Pinto C., Middleton M. J., Fabian A. C., 2016, Nature, 533, 64
Pinto C., et al., 2017, MNRAS, 468, 2865
Ponti G., Papadakis I., Bianchi S., Guainazzi M., Matt G., Uttley P., Bonilla N. F., 2012, A&A, 542, A83
Ponti G., et al., 2013, A&A, 549, A72
Porquet D., Reeves J. N., O'Brien P., Brinkmann W., 2004, A&A, 422, 85
Porquet D., et al., 2018, A&A, 609, A42
Porquet D., Reeves J. N., Grosso N., Braito V., Lobban A., 2021, A&A, 654, A89
Porquet D., Hagen S., Grosso N., Lobban A., Reeves J. N., Braito V., Done C., 2024, A&A, 681, A40
Pounds K. A., Nandra K., Stewart G. C., George I. M., Fabian A. C., 1990, Nature, 344, 132
Poutanen J., Lipunova G., Fabrika S., Butkevich A. G., Abolmasov P., 2007, MNRAS, 377, 1187
Reeves J. N., Turner M. J. L., 2000, MNRAS, 316, 234
Remillard R. A., McClintock J. E., 2006, ARA&A, 44, 49
Ricci C., Walter R., Courvoisier T. J. L., Paltani S., 2011, A&A, 532, A102
Risaliti G., Young M., Elvis M., 2009, ApJ, 700, L6
Rodman P. E., Reynolds C. S., 2024, ApJ, 960, 97
Ross R. R., Fabian A. C., 2005, MNRAS, 358, 211
Różańska A., 1999, MNRAS, 308, 751
Rozanska A., Czerny B., 1996, Acta Astron., 46, 233
Różańska A., Czerny B., 2000, MNRAS, 316, 473
Różańska A., Dumont A. M., Czerny B., Collin S., 2002, MNRAS, 332, 799
Różańska A., Czerny B., Kunneriath D., Adhikari T. P., Karas V., Mościbrodzka M., 2014, MNRAS, 445, 4385
Różańska A., Malzac J., Belmont R., Czerny B., Petrucci P.-O., 2015, A&A, 580, A77
Rusinek-Abarca K., Sikora M., 2021, ApJ, 922, 202
Rybicki G., Lightman A., 2008, Radiative Processes in Astrophysics. Physics textbook, Wiley, https://books.google.pl/books?id=eswe2StAspsC
Salpeter E. E., 1964, ApJ, 140, 796
Salvesen G., Simon J. B., Armitage P. J., Begelman M. C., 2016, MNRAS, 457, 857
Schmidt M., 1963, Nature, 197, 1040
Schnittman J. D., Krolik J. H., Noble S. C., 2013, ApJ, 769, 156
Schurch N. J., Done C., 2006, MNRAS, 371, 81
Schurch N. J., Done C., 2008, MNRAS, 386, L1
Schurch N. J., Done C., Proga D., 2009, ApJ, 694, 1
Shakura N. I., Sunyaev R. A., 1973, A&A, 24, 337
Shakura N. I., Sunyaev R. A., 1976, MNRAS, 175, 613
Shapiro S. L., Lightman A. P., Eardley D. M., 1976, ApJ, 204, 187
Shemmer O., Brandt W. N., Netzer H., Maiolino R., Kaspi S., 2008, ApJ, 682, 81
Shields G. A., 1978, Nature, 272, 706
Simon J. B., Hawley J. F., Beckwith K., 2011, ApJ, 730, 94
Singh K. P., Garmire G. P., Nousek J., 1985, ApJ, 297, 633
Sobolewska M. A., Done C., 2007, MNRAS, 374, 150
Sunyaev R. A., Titarchuk L. G., 1980, A&A, 86, 121
Tripathi P., Dewangan G. C., Papadakis I. E., Singh K. P., 2021, ApJ, 915, 25
Turner T. J., Weaver K. A., Mushotzky R. F., Holt S. S., Madejski G. M., 1991, ApJ, 381, 85
Urry C. M., Padovani P., 1995, PASP, 107, 803
Uzdensky D. A., 2013, ApJ, 775, 103
Walter R., Fink H. H., 1993, A&A, 274, 105

Weymann R., 1960, ApJ, 132, 452
Wielgus M., et al., 2022, MNRAS, 514, 780
Xiang X., et al., 2022, MNRAS, 515, 353
Zanstra H., 1955, Vistas in Astronomy, 1, 256
Zdziarski A. A., Ghisellini G., George I. M., Svensson R., Fabian A. C., Done C., 1990, ApJ, 363, L1
Zdziarski A. A., Johnson W. N., Magdziarz P., 1996, MNRAS, 283, 193
Zdziarski A. A., Lubiński P., Smith D. A., 1999, MNRAS, 303, L11
Zel'dovich Y. B., 1964, Soviet Physics Doklady, 9, 195
Zhang S. N., Cui W., Chen W., Yao Y., Zhang X., Sun X., Wu X.-B., Xu H., 2000, Science, 287, 1239
Zhong X.-G., Wang J.-C., 2022, Research in Astronomy and Astrophysics, 22, 035002
Zhu Z., Stone J. M., 2018, ApJ, 857, 34
Życki P. T., Done C., Smith D. A., 1999, MNRAS, 309, 561

Chapter 2

Paper I: Warm and thick corona for a magnetically supported disk in galactic black hole binaries

---

A&A 633, A35 (2020)
https://doi.org/10.1051/0004-6361/201935033

Astronomy & Astrophysics

Warm and thick corona for a magnetically supported disk in galactic black hole binaries

D. Gronkiewicz and A. Różańska

Nicolaus Copernicus Astronomical Center, Polish Academy of Sciences, Bartycka 18, 00-716 Warsaw, Poland
e-mail: gronki@camk.edu.pl

Received 8 January 2019 / Accepted 4 September 2019

ABSTRACT

Context. We self-consistently model a magnetically supported accretion disk around a stellar-mass black hole with a warm optically thick corona based on first principles. We consider the gas heating by magneto-rotational instability dynamo.
Aims. Our goal is to show that the proper calculation of the gas heating by magnetic dynamo can build up the warm optically thick corona above the accretion disk around a black hole of stellar mass.
Methods. Using the vertical model of the disk supported and heated by the magnetic field together with radiative transfer in hydrostatic and radiative equilibrium, we developed a relaxation numerical scheme that allowed us to compute the transition form the disk to corona in a self-consistent way.
Results. We demonstrate here that the warm (up to 5 keV) optically thick (up to $10\,\tau_{\rm es}$) Compton-cooled corona can form as a result of magnetic heating. A warm corona like this is stronger in the case of the higher accretion rate and the greater magnetic field strength. The radial extent of the warm corona is limited by local thermal instability, which purely depends on radiative processes. The obtained coronal parameters are in agreement with those constrained from X-ray observations.
Conclusions. A warm magnetically supported corona tends to appear in the inner disk regions. It may be responsible for soft X-ray excess seen in accreting sources. For lower accretion rates and weaker magnetic field parameters, thermal instability prevents a warm corona, giving rise to eventual clumpiness or ionized outflow.

Key words. accretion, accretion disks – X-rays: binaries – radiative transfer – instabilities – magnetic fields – methods: numerical

1. Introduction

There is growing evidence that a warm optically thick corona exists in accreting black holes when an accretion disk is present. It is observed in different types of accreting black holes across various masses: active galactic nuclei (AGN; Pounds et al. 1987; Magdziarz et al. 1998; Mehdipour et al. 2011; Done et al. 2012; Petrucci et al. 2013, 2018; Keek & Ballantyne 2016) including quasars (Madau 1988; Laor et al. 1994, 1997; Gierliński & Done 2004; Piconcelli et al. 2005), ultraluminous X-ray sources (ULXs; Goad et al. 2006; Stobbart et al. 2006; Gladstone et al. 2009), and galactic black hole binaries (GBHBs; Gierliński et al. 1999; Zhang et al. 2000; Di Salvo et al. 2001). A warm corona is visible as a soft component (below 2 keV) in the X-ray spectra of these objects. It is generally characterized by an excess with respect to the extrapolation of a hard X-ray power law. This power law typically originates from a region called hot corona.

The observed spectral shape of the soft X-ray excess provides us some insight into the radiative cooling mechanism that operates in the warm corona. Assuming that the thermal Comptonization is the dominant cooling process, we can model the observed spectra with so-called slab model, where soft photons from the disk enter the warm corona that is located above the disk and undergo Compton scattering with amplification factor y. During the fitting procedure, the temperature and optical depth of a warm corona can be determined. Observations of many sources indicate that a corona like this has an optical depth ranging from 4 up to 40 in different objects (Zhang et al. 2000; Jin et al. 2012; Petrucci et al. 2013, 2018, and references therein).

Furthermore, observations constrain the amount of energy that is dissipated in corona, f, in comparison to the total energy released in the whole disk or corona system. Observations of GBHBs and AGNs show that $f \approx 1$ is required to explained the observed spectral index $\alpha = 0.9$ in some sources (Haardt & Maraschi 1991; Życki et al. 2001; Petrucci et al. 2013). Petrucci et al. (2018) set a lower limit of $f = 0.8$. This behavior is not universal because it depends on the object and its spectral state, but it shows that in some circumstances, much energy is released outside of an accretion disk.

The more fundamental question is how this warm optically thick slab of gas can be created above an accretion disk that has a lower temperature. The additional process that heats the warm corona and maintains it in steady state with disk is also unclear.

Many attempts have been made to determine the universal mechanism of energy dissipation in the warm corona, but the problem is still not fully solved. A strong corona, which is responsible for most of the thermal energy that is released increases the disk stability (Svensson & Zdziarski 1994; Kusunose & Mineshige 1994; Begelman & Pringle 2007). However, detailed computations of radiative transfer in illuminated accretion disk atmospheres show that the outer warm or hot skin cannot be optically thick and stable at the same time (Ballantyne et al. 2001; Nayakshin & Kallman 2001; Różańska et al. 2002, 2015; Madej & Różańska 2004). When the irradiation increases, the ionized skin becomes unstable and the gas most probably flows out in the form of wind (Proga & Waters 2015). Computations show that the warm or hot skin with an optical depth higher than 3 cannot be thermally stable (in pressure equillibrium) with a cold

accretion disk when the skin is heated only radiatively (Krolik & Kriss 1995; Nayakshin et al. 2000; Różańska et al. 2002, 2015, and references therein).

Additional heating of the warm corona layer by an accretion process has also been considered. However, Shakura & Sunyaev (1973) introduced the geometrically thin-disk model in their seminal paper, where the kinetic energy of accreting gas is locally converted into thermal energy. According to this, within the standard disk model all energy is dissipated deep inside the disk at the equatorial plane. Vertical profiles of energy dissipation clearly show the exponential decrease toward the disk surface.

The development of numerical simulations has shown the role of the magnetic field in the structure of the accretion disk (Hawley & Balbus 1991; Balbus & Hawley 1991; Tout & Pringle 1992; Hawley 2001; Stone et al. 2008). Many magnetohydrodynamic (MHD) simulations are available, but none of them specifies the optical depth of the warm corona because most of them do not take radiative cooling into account (e.g., Bai & Stone 2013; Penna et al. 2013). The simulations that contain simplified radiative cooling (e.g., Turner 2004; Hirose et al. 2009; Ohsuga & Mineshige 2011; Noble et al. 2011) only discuss a hot corona without constrains on its observational properties (i.e., Jiang et al. 2014; Sądowski et al. 2017). Highly advanced radiative transfer calculations are usually made a posteriori after general relativistic MHD simulations are completed (Schnittman et al. 2016).

Różańska et al. (2015, hereafter RMB15) have developed an analytic model for an optically thick uniformly heated Compton-cooled corona in hydrostatic equilibrium. The heating mechanism was not specified in the model, but it allowed the authors to integrate vertically both disk and warm corona, coupled by mechanical heating and radiative cooling. This allowed them to determine the relations between the optical depth of the warm layer and the disk-corona energy budget. Furthermore, the authors have shown that when some part of the gas pressure is replaced by magnetic pressure, the optical depth of the stable corona increases.

We here assume a geometrically thin and optically thick accretion disk around a black hole (see Fig. 1). We also assume that the accretion disk is magnetized and the magneto-rotational instability (MRI) is the primary source of viscosity and energy dissipation. Based on these assumptions, we develop the model of a slab-like warm corona that covers the accretion disk and adopt realistic heating of the gas by magnetic field reconnection, which in contrast to the standard disk increases toward the disk surface (Hirose et al. 2006). We directly use the analytic formula derived by Begelman et al. (2015, hereafter BAR15), where the vertical profile of the magnetic heating of the accretion flow is determined. In addition to this major assumption, the vertical structure of the disk together with the radiative transfer equation in a gray atmosphere are fully solved with the relaxation method proposed by Henyey et al. (1964). We have developed a new numerical scheme that allows solving nonlinear differential equations in a relatively short time, which keeps the integration error low. Furthermore, with our new method we are able to pass through the thermally unstable regions that may arise when nonuniform heating and cooling mechanisms take place.

As a result, we show for which range of parameters a warm corona can exist in case of a GBHB. We determine the optical depth of the warm layer, which is the main observable when X-ray data are analyzed. Detailed calculations of the vertical structure allow us to estimate the amount of energy that is dissipated in the corona in comparison to the total energy that is released by accretion at a given radius. We show the radial structure of an optically thick corona and give tight constraints for conditions for which this warm layer can exist. All results are compared with observations.

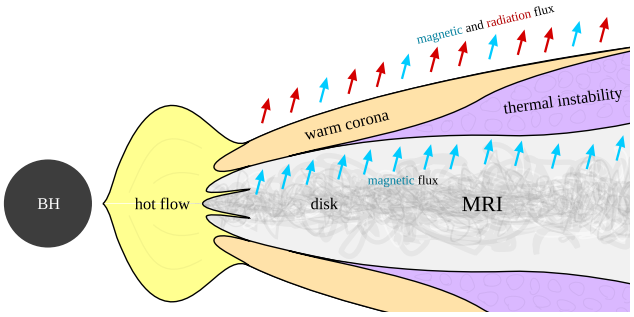

Fig. 1. Schematic illustration of a slice through the disk plane (only one side is shown due to symmetry). The black hole is shown as the circle on the left. The gray area represents the optically thick and geometrically thin disk where most of the accreting mass is located. The warm corona that covers the disk, in which the magnetic energy is released as radiation, is marked in orange. Magnetic and radiative energy flux are represented by blue and red arrows, respectively. The part of the corona that might collapse as a result of thermal instability is shown in magenta. The inner optically thin and geometrically thick hot flow that we did not consider is drawn in yellow for completion.

A warm corona is not the only possible model with which the soft X-ray excess can be explained. Other models assume relativistically smeared absorption (Gierliński & Done 2004) or reflection from an accretion disk that is illuminated by a hard X-ray continuum (García et al. 2019) or bulk Comptonization in a central Compton cloud (Shaposhnikov & Titarchuk 2006; Seifina et al. 2016). All of these models provide good fits to X-ray observations by incorporating an additional Comptonized component, but they do not explain the physical mechanism that feeds energy into the warm gas to compensate for the huge rate of the Compton cooling. Models that do provide the heating mechanism for a central compact corona exist and can successfully explain some observations without the need of involving the magnetic field (Seifina et al. 2018). However, we note that the role of the magnetic field in the accretion and jet formation process has been shown numerous times in the papers cited in this section, and we do not consider it a strong assumption. We show that an accretion disk with an operating magnetic dynamo is able to produce enough energy to heat the extended surface layer, whose physical parameters are consistent with those determined from spectral fitting of observations. Our results give a possible physical explanation for the phenomenon that was in most cases only considered from an observational perspective without analyzing the global energy budget. In order to verify whether our model can correctly reproduce the spectral features seen in X-ray sources, spectral modeling involving the redistribution function of Compton scattering must be performed. This is beyond the scope of this paper, however.

The structure of the paper is as follows: Sect. 2 presents the formalism of a magnetically heated corona and the disk-corona radiative transfer equation. It ends with a full description of the differential equations and the relaxation method we used to solve them. Section 3 presents the results of our numerical computations. We display the vertical structure of the disk-corona system, but we also show the radial limitation within which an optically thick corona can exist. Discussion and conclusions are given in Sect. 4.

2. Model setup

2.1. Magnetically heated corona

Begelman & Pringle (2007) and later BAR15 have proposed a vertical model of magnetically supported disks (MSDs) that are driven by the MRI dynamo. The MRI dynamo operating near the equatorial plane in the presence of an external poloidal magnetic field generates the toroidal magnetic flux, which converts the mechanical energy of the accretion into the electromagnetic energy that is stored as tangled magnetic field lines. The total rate of this energy deposition per unit height is $\alpha_{\rm B}\Omega P_{\rm tot}$, where $\alpha_{\rm B}$ is the toroidal magnetic field production parameter, Ω is the Keplerian angular velocity, and $P_{\rm tot}$ is the total pressure, which is the sum of gas, radiation, and magnetic pressure. Although the toroidal field production parameter $\alpha_{\rm B}$ does resemble the effective viscosity parameter $\alpha = t_{r\phi}/P$ (known from the classical thin-disk model) in the sense that it scales the energy release within the disk, its physical meaning is different, even though the expected values of both parameters are similar (Salvesen et al. 2016, hereafter SSAB16, Table 3).

The magnetic flux ropes that form near the midplane rise buoyantly toward the surface, and in the model by BAR15, the velocity is very coarsely approximated by

$$v_{\rm B}(z) = \eta\Omega z, \tag{1}$$

where $0 < \eta < 1$ is a dimensionless parameter. A similar process of a buoyant emergence of magnetic fields toward the surface is observed on the Sun, but the dynamical properties and the origin of the magnetic field are vastly different.

During the upward motion of the ropes, the magnetic field decays by various processes, releasing its accumulated energy into heating the gas. When we assume a purely toroidal flux that rises vertically with speed $v_{\rm B}(z)$, the energy dissipation rate due to the induced current, $\mathcal{H}_{\rm mag}$, can be derived from the elemental electrodynamics and yields

$$\mathcal{H}_{\rm mag} = -v_{\rm B}{\rm d}P_{\rm mag}/{\rm d}z. \tag{2}$$

This expression is consistent with intuitive reasoning: the energy loss is proportional to the magnetic energy density gradient times velocity.

Another process that may heat the gas is magnetic reconnection due to cyclic reversals of the toroidal field polarity that is observed in simulations of the MRI dynamo. The energy output of this process is proportional to the magnetic pressure $P_{\rm mag}$ and can be estimated as

$$\mathcal{H}_{\rm rec} = 2\xi\Omega P_{\rm mag}, \tag{3}$$

where ξ is a proportionality constant (Appendix A in BAR15). The rate of thermal energy release peaks in the proximity of the disk photosphere ($\tau = 1$), but its exact distribution may change depending on the model parameters. Alongside ξ, we also define, after BAR15, the reconnection efficiency parameter ν, which describes the ratio of reconnection process to the total magnetic viscosity: $\nu = 2\xi/\alpha_{\rm B}$, and it is very convenient to present our results (see Sect. 3.5).

One consequence of this picture is that the field outflow eventually reaches the point where heating becomes inefficient and some portion of the accretion energy may be carried away by the Poynting flux and is never released to heat the gas. This is contrary to nonmagnetic classical (neglecting advection) α-viscosity models where all accretion power is released as radiation. The magnetic outflow may be associated with the matter outflow, but this association is not trivial: because the outflow speed $v_{\rm B}$ is lower than the freefall speed $v_{\rm ff} = \Omega z$, most of the matter will probably slide down the magnetic flux tubes, and only a small amount is carried away by the outflow. In contrast, during the mass ejections in the solar corona, the eruption timescale is much shorter than the dynamical timescale, which results in much more efficient mass transport.

Numerical modeling shows that the process described above can be very complex, but this analytic approximation enables us to build and study the atmospheres of MSDs, which is the purpose of this paper.

Following BAR15, the accretion energy is injected into the Poynting flux and consumed for gas heating, in varying proportion. When we express the Poynting flux as $F_{\rm mag} = 2P_{\rm mag}v_{\rm B}$, the magnetic energy conservation equation can be written as

$$\begin{aligned}\alpha_{\rm B}\Omega P_{\rm tot} &= \frac{{\rm d}F_{\rm mag}}{{\rm d}z} + \mathcal{H}_{\rm rec} + \mathcal{H}_{\rm mag} \\ &= \frac{\rm d}{{\rm d}z}\left(2P_{\rm mag}v_{\rm B}\right) + \left(2\xi\Omega P_{\rm mag} - v_{\rm B}\frac{{\rm d}P_{\rm mag}}{{\rm d}z}\right).\end{aligned} \tag{4}$$

We substitute velocity and different energy rates by Eqs. (1)–(3) to obtain the final expression for the magnetic pressure gradient,

$$\eta\Omega z\frac{{\rm d}P_{\rm mag}}{{\rm d}z} = \alpha_{\rm B}\Omega P_{\rm tot} - (2\eta + \alpha_{\rm B}\nu)\Omega P_{\rm mag}. \tag{5}$$

Finally, we can use this equation to obtain the expression for the heating rate $\mathcal{H}$ [erg cm^{-3} s^{-1}] without using gradients,

$$\mathcal{H} = \mathcal{H}_{\rm rec} + \mathcal{H}_{\rm mag} = 2\left(\eta + \alpha_{\rm B}\nu\right)\Omega P_{\rm mag} - \alpha_{\rm B}\Omega P_{\rm tot}. \tag{6}$$

This heating rate describes the amount of released magnetic energy that heats the gas and can then be converted into radiation. In this paper we neglect advection and assume that the system is fully cooled by radiation, as specified in the next section.

2.2. Radiative transfer in the disk-corona system

We consider a gray plane-parallel optically thick atmosphere, which is additionally heated by dissipation of the magnetic field. We include free-free process and Compton scattering in our model and neglect synchrotron radiation, which is not important in this regime of magnetic pressure (see Sect. 3.1 for exact numbers). To determine the temperature structure, we consider three equations: a radiative equilibrium equation, a transfer equation, and an Eddington approximation.

The radiative equilibrium equation for a small-matter volume heated by various dissipation processes at rate $\mathcal{H}$ and by the local radiation field of mean intensity J_ν and cooled by the radiation emissivity j_ν reads

$$4\pi\int_\nu \kappa_\nu\rho J_\nu{\rm d}\nu + \mathcal{H} = 4\pi j_{\rm bol}, \tag{7}$$

where $j_{\rm bol} \equiv \int_\nu j_\nu{\rm d}\nu$, and ρ is gas density in g cm^{-3}. Here, we assumed that the entire dissipated thermal energy is locally converted into radiation (neglecting advection).

In an optically thick regime, when true absorption processes dominate scattering, the radiation field is fully thermalized and strictly local, therefore for matter at temperature T, we have $J_\nu = B_\nu(T)$, where $B_\nu(T)$ is the Planck function for temperature T. However, because a corona is a strongly scattering medium, this is not the case (particularly near the surface), and the actual radiation field intensity may deviate from a Planck distribution toward a Wien distribution. The further deviation from the Planck law is caused by non-coherent inverse Compton scattering. We still assume that the spectrum of mean radiation intensity

J_ν within the disk can be approximately described by the Planck function with temperature $T_{\rm rad}$, that is, $J_\nu \approx B_\nu(T_{\rm rad})$. With these assumptions, we can define our frequency-averaged quantities

$$B = \int_0^\infty B_\nu {\rm d}\nu = \int_0^\infty B_\nu(T){\rm d}\nu = \sigma T^4/\pi, \tag{8}$$

$$J = \int_0^\infty J_\nu {\rm d}\nu = \int_0^\infty B_\nu(T_{\rm rad}){\rm d}\nu = \sigma T_{\rm rad}^4/\pi. \tag{9}$$

Even when we assume that the radiation field has a Planck distribution, we do not equal gas and radiation temperatures because the corona is strongly dominated by scattering.

For the gray atmosphere we considered in this paper, we used both Rosseland and Planck averages, the latter denoted with a "P" superscript. The following values for electron scattering and free-free opacities were assumed:

$$\kappa_{\rm es} = 0.34\,{\rm g}^{-1}{\rm cm}^2, \tag{10}$$

$$\kappa_{\rm ff}^{\rm P} = 37\cdot\kappa_{\rm ff} = \kappa_{\rm ff,0}^{\rm P}\cdot\rho T^{-7/2}\ {\rm g}^{-1}{\rm cm}^2, \tag{11}$$

where $\kappa_{\rm ff,0}^{\rm P} = 37\times6.21\times10^{22}$ is a constant from Kramers opacity approximation in cgs units. Through this paper, we denote the total Rosseland mean opacity as $\kappa = \kappa_{\rm es} + \kappa_{\rm ff}$, while $\kappa^{\rm P} = \kappa_{\rm es} + \kappa_{\rm ff}^{\rm P}$ is the total Planck opacity.

Using the gray approximation, we can rewrite the radiative equilibrium Eq. (7) as

$$\mathcal{H} = 4\pi\left(j_{\rm bol} - \kappa^{\rm P}\rho J\right) \equiv \Lambda_{\rm rad}(\rho, T, T_{\rm rad}). \tag{12}$$

We refer to the function $\Lambda_{\rm rad}(\rho, T, T_{\rm rad})$ as the *net* radiative cooling rate.

To estimate the effect of inverse Compton scattering, we used the standard formula given by Rybicki & Lightman (2008), where by $J_{\rm C}$ we mean all incident photons that were scattered with thermalized electrons of the gas temperature T:

$$J'_{\rm C} - J_{\rm C} = J_{\rm C}\frac{4kT\langle\varepsilon\rangle - \langle\varepsilon^2\rangle}{\langle\varepsilon\rangle m_e c^2}. \tag{13}$$

In this formula $J'_{\rm C} - J_{\rm C}$ is the energy passed to the radiation from electrons by the inverse Compton scattering. The mean photon energy $\langle\varepsilon\rangle$ and mean squared energy $\langle\varepsilon^2\rangle$ depend on the photon energy distribution, and their ratio has the following values:

$$\langle\varepsilon^2\rangle = \begin{cases} 3.83kT_{\rm rad}\cdot\langle\varepsilon\rangle & \text{for a Planck spectrum} \\ 4kT_{\rm rad}\cdot\langle\varepsilon\rangle & \text{for a Wien spectrum.} \end{cases} \tag{14}$$

Although we assumed that the radiation has a Planck spectrum everywhere in the atmosphere, for a strongly scattering medium with a Compton-cooled corona, the radiation spectrum is shifted toward slightly higher energies, and we find the approximation $\langle\varepsilon^2\rangle = 4kT_{\rm rad}\cdot\langle\varepsilon\rangle$ satisfactory for our model. When the temperatures are low, density is high, and free-free absorption dominates, this term is negligible and does not change the result. Therefore we replace $J_{\rm C} = \kappa_{\rm es}J$ to obtain the Compton term for the emission function,

$$j_{\rm IC} = \kappa_{\rm es}J\frac{4k(T - T_{\rm rad})}{m_e c^2}. \tag{15}$$

Finally, by taking into account all relevant opacities, we obtain the emission function $j_{\rm bol}$ of the following form:

$$j_{\rm bol} = \kappa_{\rm ff}^{\rm P}B + \kappa_{\rm es}J + j_{\rm IC} = \kappa_{\rm ff}^{\rm P}B + \kappa_{\rm es}J\left[1 + \frac{4k(T - T_{\rm rad})}{m_e c^2}\right]. \tag{16}$$

We can now substitute the expressions for B, J, and $j_{\rm bol}$ into the cooling function $\Lambda_{\rm rad}$ to obtain its final form,

$$\Lambda_{\rm rad}(\rho, T, T_{\rm rad}) \equiv 4\sigma\rho\left[\kappa_{\rm ff}^{\rm P}\left(T^4 - T_{\rm rad}^4\right) + \kappa_{\rm es}T_{\rm rad}^4\frac{4k\,(T - T_{\rm rad})}{m_e c^2}\right]$$

$$= 4\sigma\rho\,(T - T_{\rm rad})\left[\kappa_{\rm ff}^{\rm P}\,(T + T_{\rm rad})\left(T^2 + T_{\rm rad}^2\right) + \kappa_{\rm es}\frac{4kT_{\rm rad}^4}{m_e c^2}\right]. \tag{17}$$

The net cooling rate can be split into two terms: $\Lambda_{\rm rad} = \Lambda_{\rm B} + \Lambda_{\rm C}$, describing the contributions of bremsstrahlung and Compton scattering,

$$\Lambda_{\rm B} = 4\sigma\rho\kappa_{\rm ff}^{\rm P}\left(T^4 - T_{\rm rad}^4\right), \tag{18}$$

$$\Lambda_{\rm C} = 4\sigma\rho\kappa_{\rm es}T_{\rm rad}^4\frac{4k\,(T - T_{\rm rad})}{m_e c^2}. \tag{19}$$

We solve here the frequency-integrated radiative transfer equation (Eq. (4) in RMB15), where the zeroth moment of this equation reads

$$\frac{{\rm d}H}{{\rm d}z} = j_{\rm bol} - \kappa^P\rho J. \tag{20}$$

When we average this over the frequencies and replace the Eddington flux with a physical flux $4\pi H_{\rm Edd} = F_{\rm rad}$, we obtain the expected result that the energy gained by the radiative flux is equal to the rate of radiative gas cooling,

$$\frac{{\rm d}F_{\rm rad}}{{\rm d}z} = \Lambda_{\rm rad}\,(\rho, T, T_{\rm rad})\,. \tag{21}$$

Because we are interested in the optically thick regime, we assume the Eddington approximation, that is, $J = 3\,{\rm K}$, where K is the second moment of specific intensity. We therefore solve the first moment of the radiative transfer equation as

$$\frac{1}{3}\frac{{\rm d}J}{{\rm d}z} = \frac{{\rm d}K}{{\rm d}z} = -\kappa\rho H_{\rm Edd}. \tag{22}$$

Taking into account Eq. (9) and the connection of the Eddington flux with the physical flux, this equation yields

$$16\sigma T_{\rm rad}^3\frac{{\rm d}T_{\rm rad}}{{\rm d}z} = -3\kappa\rho F_{\rm rad}. \tag{23}$$

Radiative transfer should be always coupled with the gas structure. We assume that the whole disk-corona system is in hydrostatic equilibrium, that is,

$$\frac{{\rm d}P_{\rm gas}}{{\rm d}z} + \frac{{\rm d}P_{\rm mag}}{{\rm d}z} = \frac{\kappa\rho}{c}F_{\rm rad} - \Omega^2\rho z, \tag{24}$$

where the gas pressure typically is $P_{\rm gas} = k/\mu m_H T\rho$, and the first part on the right side denotes the radiation pressure $P_{\rm rad}$. This equation is consistently implemented into a full set of equations that is solved simultaneously from the midplane to the surface of the corona. This treatment proves that we do not treat the disk-corona system as a two-slab model, but solve the full gas structure together with proper heating processes and radiative cooling taken into account.

2.3. Equation set and boundary conditions

We solved the following set of five equations: (5), (12), (21), (23), and (24), using the expression for the heating rate given by Eq. (6) and that for the cooling function given by Eq. (17). The full numerical procedure of our numerical code is presented in Appendix A. We integrated them from the disk equatorial plane ($z = 0$) to the upper bound of the computational range ($z = z_{\rm max}$). We estimated $z_{\rm max}$ by solving Eq. (38) in BAR15 for the height at which the magnetic pressure reaches $p = 10^{-5}$ of the magnetic pressure at the midplane,

$$z_{\rm max} = H_{\rm SS73}\sqrt{\left(4+\frac{\alpha_{\rm B}\nu}{\eta}\right)(p^{-2/\tilde{q}}-1)}, \tag{25}$$

where $H_{\rm SS73}$ is the disk height derived from the α-disk model (Shakura & Sunyaev 1973) and

$$\tilde{q} \equiv 2+\frac{\alpha_{\rm B}(\nu-1)}{\eta}. \tag{26}$$

The requirement of hydrostatic equilibrium gives the balance between all pressures: magnetic, radiation, and gas pressure, and the gravity force in vertical direction. We determined the gas temperature by solving the balance equation between magnetic heating and Compton cooling in order to determine whether and in which circumstances the corona can form.

We show that the problem is better solved when other radiative processes, such as free-free emission, are taken into account. We analyzed two cases: case A, when $\Lambda_{\rm rad} \equiv \Lambda_{\rm B}+\Lambda_{\rm C}$ is given by the full Eq. (17) above, and case B, when $\Lambda_{\rm rad} \equiv \Lambda_{\rm C}$ and thus the free-free term is set to zero, and the atmosphere is only cooled by Compton scattering.

In the case B, Eq. (17) is linear and we obtain exactly one temperature solution in each point of the vertical structure, as opposed to case A, for which multiple solution can exist. However, in case B, the cooling rate is decreased, therefore the gas temperature in the transition region between the disk and corona is overestimated. Despite this, because the density in the corona depends mostly on magnetic pressure gradient and becomes bounded to the gas pressure only in extremely weakly magnetized cases, case B allows us to obtain almost the exact density value compared to case A.

We adopted the following procedure: We solved the entire model using case B. Now to correct the temperature in the transition region where case B performs worst, we solved the Eq. (21) again, but kept the density fixed, which guarantees a unique solution. Because we corrected the temperature but did not update the density or gas pressure, we deviate slightly from hydrostatic equilibrium. However, the corona is dominated by the magnetic field pressure gradient, and this deviation is negligible and does not change the overall structure of the atmosphere. At this little cost, we are able to overcome the instability and investigate the influence of disk magnetization on its presence and strength.

We adopted boundary conditions appropriate for a cylindrical geometry of the accretion disk. The radiative flux carried through the midplane ($z = 0$) must vanish due to symmetry,

$$F_{\rm rad} = 0. \tag{27}$$

Following BAR15, we also assumed that the magnetic pressure gradient at the equatorial plane must be zero. Therefore, from Eq. (5) we obtain

$$P_{\rm tot} = \left(\frac{2\eta}{\alpha_{\rm B}}+\nu\right)P_{\rm mag}. \tag{28}$$

If the radiation pressure is neglected, the relation derived by BAR15 between the parameters $\alpha_{\rm B}$, η, ν, and the magnetic parameter ($\beta = P_{\rm gas}/P_{\rm mag}$) at the equatorial plane β_0 is

$$\beta_0 = \frac{2\eta}{\alpha_{\rm B}}+\nu-1. \tag{29}$$

At the top of the atmosphere ($z \to \infty$), we assumed that the sum of the flux carried away by radiation and of the magnetic field is equal to the flux obtained by Keplerian disk theory,

$$F_{\rm rad}+F_{\rm mag} = F_{\rm acc} = \frac{3}{8\pi}\frac{GM\dot{M}}{R^3}\left(1-\sqrt{\frac{3R_{\rm Schw}}{R}}\right), \tag{30}$$

where G is the gravitational constant, M is the black hole mass, $\dot{M}$ is the accretion rate, and R is the radial distance from black hole. Typically, $R_{\rm Schw}$ denotes the Schwarzschild radius, which is given as $2GM/c^2$. We also used the standard boundary condition for radiative transfer, $J = 2H$, which guarantees that the disk is not externally illuminated. Expressed in our convention, the boundary condition at $z_{\rm max}$ takes the form

$$F_{\rm rad}-2\sigma T_{\rm rad}^4 = 0. \tag{31}$$

This gives a total of four boundary conditions, which complete our set of five equations because Eq. (12) is not a differential equation, and Eqs. (5), (21), (23), and (24) are first-order nonlinear ordinary differential equations.

Our numerical computations are parameterized by six input quantities: three magnetic, $\alpha_{\rm B}$, η and ν, and three disk parameters: black hole mass, radial distance, and the accretion rate. For better convenience, we used the accretion rate $\dot{m} = \dot{M}\kappa_{\rm es}c/48\pi GM$, given in units of the Eddington rate with an accretion efficiency for a Newtonian potential.

3. Vertical structure of the disk with corona

3.1. Parameter regime

Throughout this paper we consider the case of GBHB with $M = 10\,M_\odot$. The results are presented for a wide range of accretion rates from $\dot{m} = 10^{-3}$ up to 1 and for radial distances from a marginally stable orbit up to $R/R_{\rm Schw} = 400$. The value of the disk outer radius we adopted was taken from the fact that for larger distances corona does not exist at all or it is very weak.

The parameters $\alpha_{\rm B}$, η, and ν used in our computations have been determined by SSAB16 from numerical simulations for several runs of a varying net poloidal magnetic flux value, which resulted in different degrees of disk magnetization. Their results are plotted in Fig. 2 by points.

For strongly magnetized case, simulations show that $\alpha_{\rm B} \approx \eta \simeq 0.3$, $\beta_0 \simeq 1$ and $\xi \simeq 0$, which gives the reconnection efficiency parameter $\nu = 0$. This means that the field production is efficient, the outflow is at a high rate, and dissipation by reconnection is low. On the other hand, for the weakly magnetized case, simulations result in $\alpha_{\rm B} \simeq 0.02$, $\eta \simeq 0.04$, $\beta_0 \simeq 50$, and due to frequent dynamo reversals, $\xi \simeq 0.5$. For this case, the reconnection efficiency parameter $\nu \simeq 50$. On the other hand, SSAB16 concluded that models with ν higher than a few tend to overestimate the magnetic field gradient for weakly magnetized models and that $\nu = 0$ describes the magnetic pressure descent more accurately for these cases (see Fig. 13 from SSAB16). This means that it would be more consistent to assume the ν parameter to have relatively low values, on the order of a few, to be in agreement with the vertical shape of the magnetic pressure.

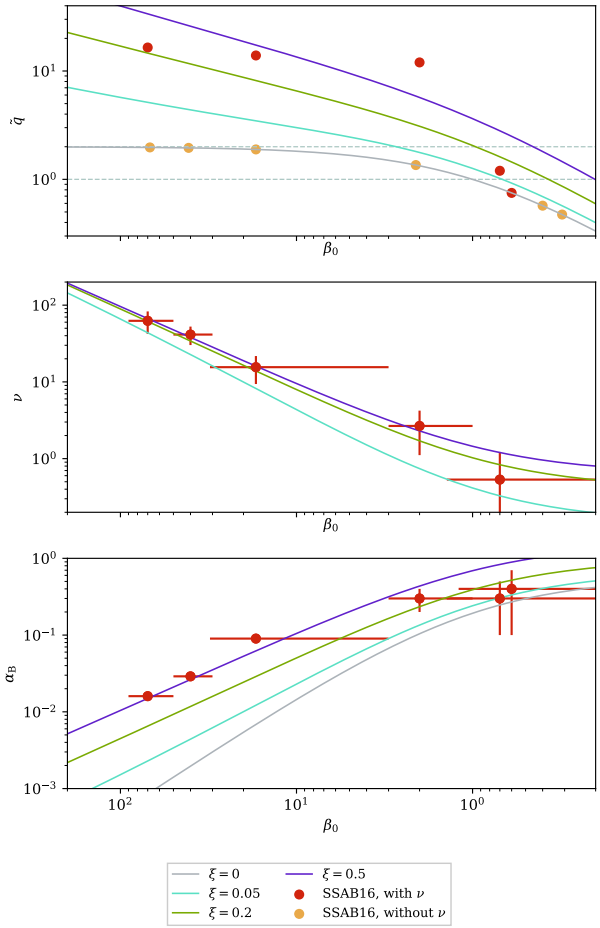

Fig. 2. Dependence of model parameters: toroidal field production efficiency, α_B (*lower panel*), reconnection efficiency, ν (*middle panel*), and the magnetic field gradient parameter, $\tilde{q}$ (*upper panel*) on the magnetic parameter in the disk midplane β_0. Points denote values obtained from numerical simulations in SSAB16 and lines are our results from the power-law relation between α_B and η (Eq. (33)) for four values of ξ.

To reduce the number of magnetic parameters to consider, we assumed a constant value of ξ and made the simplification that α_B and η are tied by a power law relation. Using Eq. (29), we recomputed α_B , which is consistent with an assumed value of ξ and η^{sim} and β_0^{sim} taken from Tables 2 and 3 of the SSAB16 paper,

$$\alpha_B = \frac{\eta^{sim} + \xi}{\beta_0^{sim} + 1} \tag{32}$$

We then performed a power-law fit and found that for $\xi = 0.05$ the relation that best fits the six data points is

$$\eta = 1/3\alpha_B^{7/18} . \tag{33}$$

The dependence of the magnetic parameters on the use of these analytical formulae is plotted by lines in Fig. 2 for comparison with simulations. The figure shows that we can adopt the values of magnetic parameters, which are consistent with simulations.

The upper panel of Fig. 2 shows the magnetic pressure gradient, which is an important quantity influencing the magnetic energy release. The magnetic pressure gradient can be derived

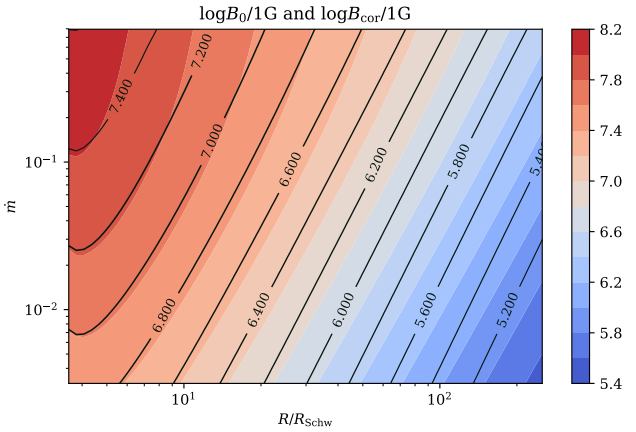

Fig. 3. Toroidal magnetic field at the equatorial plane B_0 and in the corona B_{cor} at optical depth τ_{cor} (see text for definition) in Gauss units. Logarithmic values of the magnetic field are plotted in the radius (R/R_{schw}) – accretion rate ($\dot{m}$) parameter plane.

from Eq. (5) and yields

$$q = -\frac{d \ln P_{mag}}{d \ln z} = 2 + \frac{\alpha_B}{\eta}\left(\nu - \frac{P_{tot}}{P_{mag}}\right) . \tag{34}$$

In the corona, when $P_{gas} + P_{rad} \ll P_{mag}$, we can substitute $P_{tot}/P_{mag} \simeq 1$. The value of q is then constant, and when we express it in terms of model parameters only, we obtain a result that is compatible with Eq. (37) in BAR15:

$$q \approx \tilde{q} = 2 + \frac{\alpha_B\,(\nu - 1)}{\eta} = \frac{2\beta_0}{1 + \beta_0 - \nu} . \tag{35}$$

With α_B remaining the only free magnetic parameter in our model, the value that we find most suitable for potentially interesting disks is $\alpha_B = 0.1$. For this parameter, the radial distribution of the toroidal magnetic field at the equatorial plane B_0 and at the base of the corona B_{cor} (where the gas temperature achieves minimum), depending on the accretion rate and the distance from black hole, is given in Fig. 3. The magnetic field in our computations never approached values of 10^8 G.

3.2. Characteristics of the vertical profile

The typical structure of the disk-corona system for $\dot{m} = 0.05$ and $R/R_{Schw} = 10$ is shown in Fig. 4. The results are presented with respect to the height above the disk midplane z/H, where half of the disk thickness is given by

$$H = \sqrt{\frac{\int_0^\infty \rho z^2 dz}{\int_0^\infty \rho dz}} . \tag{36}$$

Furthermore, to better present the results, we defined the total optical depth of the system according to the standard formula $d\tau = -\kappa^P \rho\, dz$, where the electron scattering optical depth is denoted as $d\tau_{es} = -\kappa_{es}\rho\, dz$, and the density number per unit of volume is $n_H = \rho/m_H$.

In our model the transition in vertical structure between the disk and warm corona occurs naturally, therefore we show the location of the photosphere $\tau = 2/3$ and thermalization depth $\tau^\star = 1$, where the seed photons originate (see Rybicki & Lightman 2008, Sect. 1.7), by the vertical lines in Fig. 4.

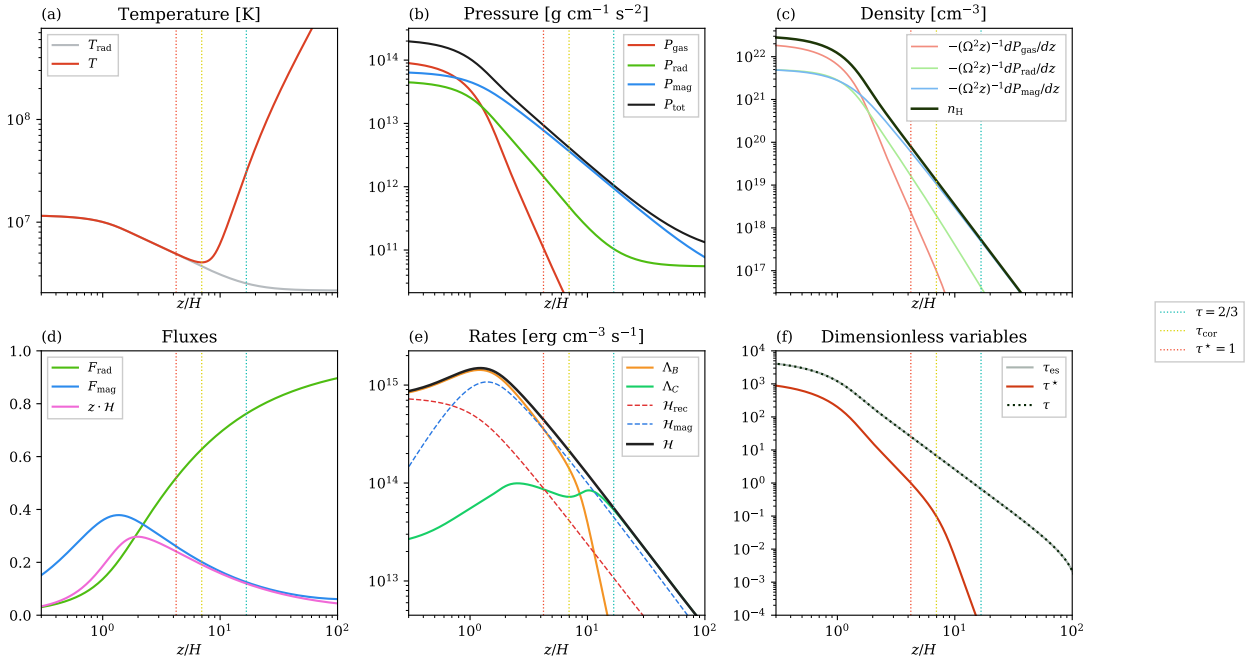

Fig. 4. Vertical structure of the disk-corona system computed at the single radius $R = 10\,R_{Schw}$ for $\dot{m} = 0.05$. The horizontal axis is the height above the disk midplane given in scale height H defined by Eq. (36). Three significant locations are marked with vertical dotted lines: the photosphere (green), the temperature minimum (dark yellow), and the thermalization depth (red). The following panels display (*a*) radiation and gas temperature; (*b*) gas, radiation, magnetic, and total pressure; (*c*) gas density and pressure gradients; (*d*) radiative energy flux, magnetic (Poynting) flux, and gas heating rate all normalized to the total accretion flux F_{acc}; (*e*) net radiative cooling terms (Λ_B and Λ_C) and gas magnetic heating rates; and (*f*) electron scattering and total and effective optical depths.

The thermalization depth is equivalent to the effective optical depth, which in our case was computed using Planck opacities (see Sect. 2.2). We took the temperature minimum as the inner boundary of the corona, and we refer to electron scattering optical depth of the temperature minimum as τ_{cor}, which is also marked by a vertical line in all panels of Fig. 4.

Although the geometrical proportions and physical parameters can vary when the model input changes, we almost universally obtain a structure in which three distinct regions can be observed that directly correspond to the gas pressure structure: (i) the accretion disk, where most of the matter is located, characterized by high density near the midplane, the gas temperature that exactly follows the radiation temperature, and domination of the gas and radiation pressure over the magnetic pressure; panels a and b. (ii) The transition region, where bremsstrahlung is still an important cooling mechanism and the gas temperature is coupled to the radiation field temperature, but the magnetic pressure takes over in supporting the structure and slows the density decrease with height; panel c. (iii) The corona, where the density is low and therefore the temperature must increase with height so that the disk remains in energy equilibrium; matter is cooled mainly by the inverse Compton scattering, while the density structure is fully supported by the magnetic pressure; panels b and c. In the case presented in Fig. 4, the following regions extend within $0 \lesssim z/H \lesssim 3$, $3 \lesssim z/H \lesssim 7$, and $7 \lesssim z/H$, respectively. A noticeable increase in temperature appears in the transition region, when the warm corona starts to form due to the magnetic heating.

The overall magnetic pressure profile (see panel b) is in agreement with that obtained by BAR15, which confirms the correctness of our calculations. The density profile of the outermost coronal layers is fully shaped by pressure gradients, of which the magnetic pressure gradient is the largest (see panel c).

When we solve the vertical structure of the MSD, the magnetic energy flux F_{mag} needs to be considered in addition to the radiative energy flux F_{rad}, the latter being the only energy transport channel in a classical α-disk. Both fluxes normalized to F_{acc} are shown in Fig. 4d and are equal to zero in the disk midplane. In contrast to the α-disk, where the heating is mostly located near the disk midplane, we obtained a heating distribution that peaks at a few scale heights, although still below the temperature inversion point; see Fig. 4e. This behavior is mostly the effect of purely magnetic heating $\mathcal{H}_{mag}$, which depends on the magnetic pressure gradient. Heating by reconnection $\mathcal{H}_{rec}$ is proportional to the magnetic pressure (rather than its gradient) and peaks around the midplane.

The total optical depth of the disk-corona system is about 10^4. The differences between various optical depth profiles are visible in panel f of Fig. 4. For the above example, the whole corona is dominated by electron scattering, that is, $\tau_{es} = \tau$. The corona starts at $\tau_{cor} \sim 10$, and the total optical depth $\tau \sim 20$ where full thermalization occurs, for instance, $\tau^\star = 1$. The corona is optically thick, which agrees with recent observations.

3.3. Thermal instability of the intermediate layer

Thermal instability in the medium can occur if under given conditions the cooling rate does not increase with temperature. The thermal balance equation then has three solutions, and if the matter is on the unstable branch, a thermal runaway or collapse occurs, following a small deviation from equilibrium. The coronal thermal instability in accretion disks has been investigated

for many years (Krolik et al. 1981; Kusunose & Mineshige 1994; Nakamura & Osaki 1993; Różańska & Czerny 1996; Różańska et al. 1999), but it has never been treated in the presence of magnetic field.

Considering the static vertical structure of the accretion disk, it is reasonable to assume that any thermal collapse is an isobaric process. The condition for thermal instability reads

$$\mathcal{L}_{\rm rad} \equiv \left.\frac{{\rm d}\ln\Lambda_{\rm rad}}{{\rm d}\ln T}\right|_{\delta P_{\rm gas}=0} < 0\,. \tag{37}$$

When we split the cooling into $\Lambda_{\rm B}$ and $\Lambda_{\rm C}$ contributions and substitute the opacities given by Eqs. (10) and (11), we obtain

$$\left.\frac{{\rm d}\Lambda_{\rm B}}{dT}\right|_{\delta P_{\rm gas}=0} = 2\sigma\frac{\kappa^{\rm P}_{\rm ff}}{T}\left(11T^4_{\rm rad} - 3T^4\right)\,, \tag{38}$$

$$\left.\frac{{\rm d}\Lambda_{\rm C}}{dT}\right|_{\delta P_{\rm gas}=0} = 16\sigma\frac{\kappa_{\rm es}\rho}{T}\frac{kT^5_{\rm rad}}{m_e c^2}\,. \tag{39}$$

Depending on the contributions from these two terms, we distinguish tree cases: i when $\Lambda_{\rm B} \ll \Lambda_{\rm C}$, the solution is always thermally stable because Eq. (39) has positive sign, ii when $\Lambda_{\rm B} \gg \Lambda_{\rm C}$, instability occurs for

$$T \geq \sqrt[4]{\frac{11}{3}}T_{\rm rad} \approx 1.38T_{\rm rad}, \tag{40}$$

and finally, iii when $\Lambda_{\rm B} \approx \Lambda_{\rm C}$ and $T > T_{\rm rad}$, radiative heating by bremsstrahlung is negligible, and the criterion for instability reads

$$\rho^2 T \geq \left[\frac{8}{3}\frac{\kappa_{\rm es}}{\kappa^{\rm P}_{\rm ff,0}}\frac{kT^5_{\rm rad}}{m_e c^2}\right]^2 \approx 4.30\times10^{-9}\left(\frac{T_{\rm rad}}{10^6\ {\rm K}}\right)^{10}. \tag{41}$$

In the isobaric regime, when $\delta P_{\rm gas} = 0$ or $\rho T = $ const., this defines the upper limit for the temperature for which thermal instability occurs. The transition between these regimes ii and iii occurs for the density

$$\rho = \frac{8}{3}\sqrt[8]{\frac{3}{11}}\frac{\kappa_{\rm es}}{\kappa^{\rm P}_{\rm ff,0}}\frac{kT^{9/2}_{\rm rad}}{m_e c^2} \approx 5.58\times10^{-35}T^{9/2}_{\rm rad}. \tag{42}$$

In order to show the transition between stable and unstable corona, the net cooling function in MSD for three slightly varying accretion rates 0.35, 0.50, and 0.72 is presented in Fig. 5 for the radiation temperature $T_{\rm rad} = 10^6$K. The three models vary mainly by the shift in density; the highest density corresponds to the lowest accretion rate.

Each model starts at the disk midplane where $T \approx T_{\rm rad}$, and only when the transition to the corona starts does the gas temperature diverge from the radiation temperature. When the density is higher than that given by Eq. (42), the model will inevitably enter the zone defined by Eq. (40). Otherwise, for hotter disks, the contribution of Compton cooling will yield at least half of the total cooling, and the model might graze the instability boundary defined by Eq. (41) but never exceed it. This means that all but the Compton-dominated disks will be affected by thermal instability of the transition region. The only stable solution is possible for relatively rare disks for the low cooling rate, that is, the left-hand side of the white thick solid line.

The same three models are shown Fig. 6. In order to identify all thermal equilibrium solutions for each height above the disk midplane, the fraction of Compton cooling, the energy balance, and the cooling function gradient $\mathcal{L}_{\rm rad}$ are shown depending on

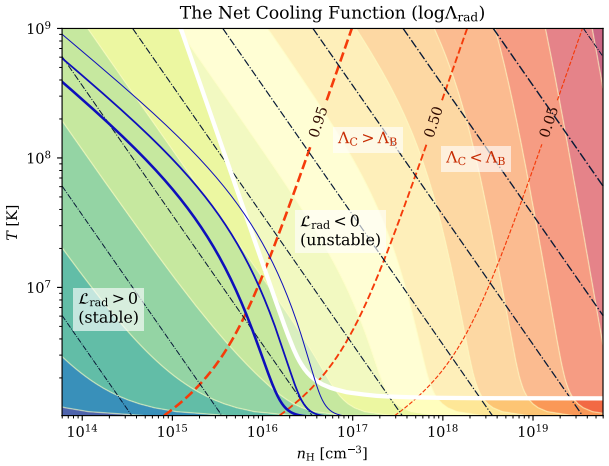

Fig. 5. Logarithm of the net cooling rate $\Lambda_{\rm rad}$ (Eq. (17)), plotted in the $n_{\rm H} - T$ parameter plane ranging from blue (low rate) to red (high rate). The points of constant pressure are connected with black dash-dotted lines. The red dotted contours show the contribution of the Compton cooling to the total cooling. The solid white line shows where the cooling function is constant in isobaric perturbation, and separates the area of unstable solutions where the gradient of the cooling function $\mathcal{L}_{\rm rad} < 0$. Dark blue lines of increasing width represent the vertical structure for three accretion rates 0.035, 0.050, and 0.072.

the gas temperature T while maintaining constant gas pressure. For the hottest model (highest accretion rate), there is an unambiguous solution in each point. This changes when the temperature decreases: although the main continuous solution is still stable (compared to Fig. 5), two cooler solutions appear. The middle solution lies within the unstable zone (pink area in the third column), but the coldest solution is stable. This means that because this area is dominated by magnetic pressure, an abrupt density change would not greatly affect the hydrostatic equilibrium and the existence of two-phase matter is possible. Finally, for the lowest accretion rate (upper panels of Fig. 6), no numerically consistent stable solution exists. We expect that matter in this region would remain cold, but above the unstable region, a corona might still form. This corona would be hot and optically thin, and in the example we discussed, the transition would occur at about $z/H \sim 20$.

Equations (40) and (41) define the lower and upper limits for the temperature that allows the occurrence of thermal instability. This is clearly shown in Fig. 5, as each isobaric contour slices the instability boundary in exactly two points. These solutions are also plotted in Fig. 6 with orange lines. They indeed suffice to describe the instability in most of the vertical structure of the disk.

3.4. Local properties of the corona

The disk-corona transition at the given radius depends on the value of the local temperature and density. We present here the evolution of the selected disk parameters with an accretion rate and magnetization state with the aim to demonstrate better how the warm corona can arise at radius $R = 10\,{\rm R_{Schw}}$. For this purpose we define here two additional quantities related to the radiation pressure because the radiation energy is the main observable of the accretion disk-corona systems. The first such quantity is the so-called radiation efficiency, that is, the ratio of the radiation flux to the total flux that is dissipated locally at a certain

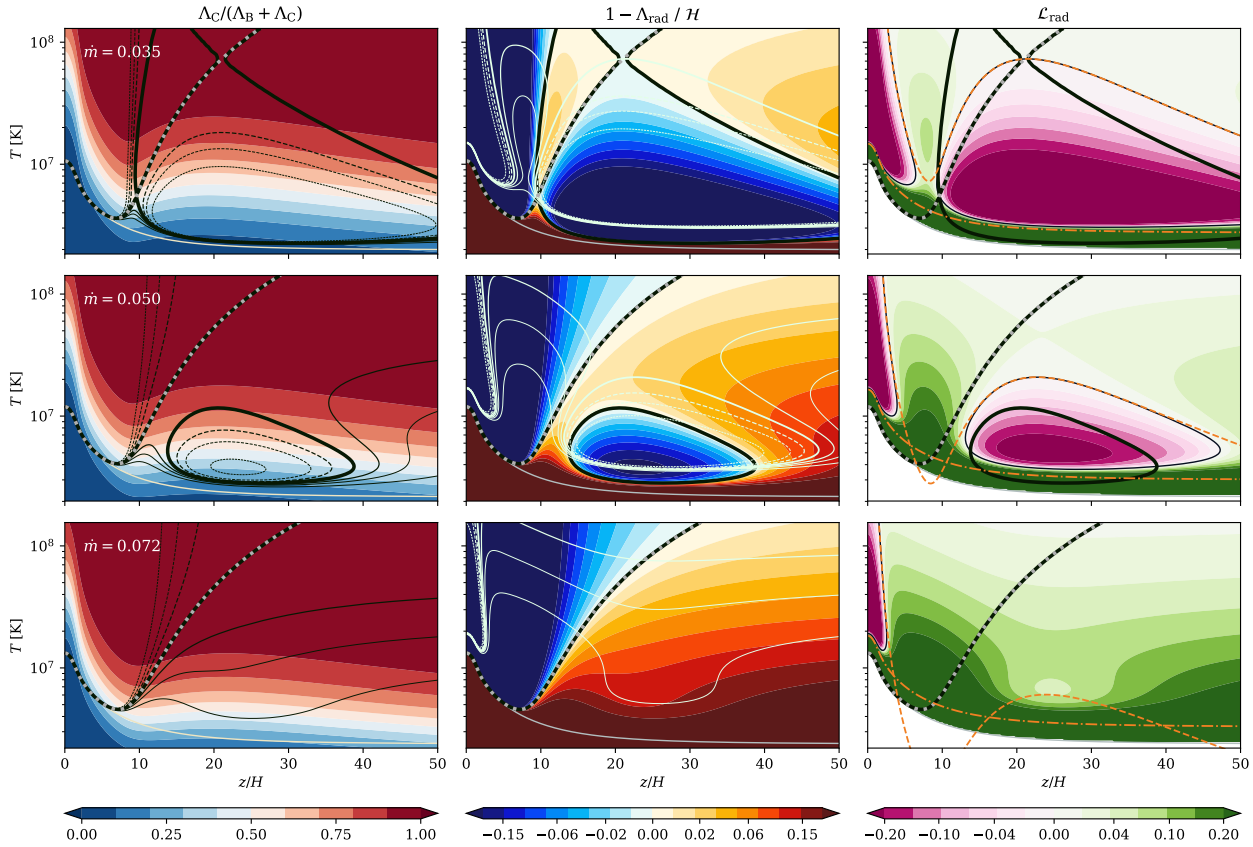

Fig. 6. Onset of thermal instability in a low-temperature disk, $\dot{m} = 0.035$ shown in the *top panels*, and its stabilization with the increase of the temperature, $\dot{m} = 0.05$ and 0.072 shown in the *middle and bottom panels*. Other disk parameters are as given in Sect. 3.1. In each panel the vertical axis represents the possible gas temperature T assuming constant gas pressure ($\delta P_{\rm gas} = 0$), and the horizontal axis is the height above the disk midplane given in scale height H (Eq. (36)). The possible solutions that satisfy the radiative energy balance are shown with thick black contours, while the solution obtained from our numerical computations is additionally marked with light gray dots. A thinner gray line is used to show the radiation temperature, $T_{\rm rad}$. Color maps in the first panels column show the contribution from Compton scattering to the total cooling. In the second column, the overall heating-cooling balance is shown: the yellow-orange areas are where the heating dominates cooling, and blue areas show where the cooling rate exceeds the heating. The third column presents the stability diagnostic, i.e., the cooling function gradient $\mathcal{L}_{\rm rad}$ (Eq. (37)), with green areas marking the stable regions and violet areas the unstable regions. Two limit solutions according to Eqs. (40) and (41) are plotted with orange lines (dash-dotted and dashed, respectively) and show excellent agreement with the numerical solution. Additionally, the content of neighboring plots (*from right panels to the middle*, and *from middle to the left*) are superimposed as thin contours for the sake of clarity.

point of the vertical structure due to magnetic field reconnection $F_{\rm rad}/F_{\rm acc}$, while the second quantity is the ionization parameter Ξ (Krolik et al. 1981), which is defined as

$$\Xi = \frac{P_{\rm rad}}{P_{\rm gas}} \,. \tag{43}$$

In Figs. 7 and 8 we show the structure of the temperature, the magnetic field gradient, the radiation efficiency, the cooling function gradient, the contribution of Compton cooling to the total cooling, and the ionization parameter in panels a to f, respectively. For all cases of the accretion rate we achieve a hot outermost layer at the top of the inner accretion disk.

The temperature of the corona is very stable with respect to the accretion rate, but the optical depth for which the disk-corona transition occurs increases with accretion rate and reaches the value of ≈ 10 for $\dot{m} = 0.71$. In contrast, the accretion rate determines the density of the disk, and consequently, the value of the magnetic pressure gradient that saturates in the disk at the highest value for the lowest accretion. At the point of disk-corona transition, the magnetic pressure slightly decreases, but the rate of the radiative energy release is roughly the same, see panel c. We conclude that the primary factors causing the optical depth of the corona to vary are the changes in disk temperature (and the transition region, consequently).

Panel e partly explains this behavior: for lower accretion rates, cooling in the disk is dominated by bremsstrahlung, which switches off at around $\tau \sim 1$, causing an abrupt temperature gradient in the corona boundary. At the same time, the cooling function gradient also becomes negative for these cases (panel d). We conclude here that this contribution from bremsstrahlung also causes the formation of an unstable region, as discussed in Sect. 3.3. For higher accretion rates, the contribution from bremsstrahlung is not that significant, and the transition from the disk to the corona is almost seamless. The ionization parameter presented in panel f does not indicate a thermally unstable region. It shows the inversion with optical depth, which is shallower for Compton-dominated cases (high accretion rate). Finally, Ξ is larger for hotter and rarer disks.

The changes in the corona are much more dramatic when the dependence on the magnetic field is examined, as shown in Fig. 8. Panel a shows that corona optical depth and temperature are radically different for weak and strong magnetic fields. For

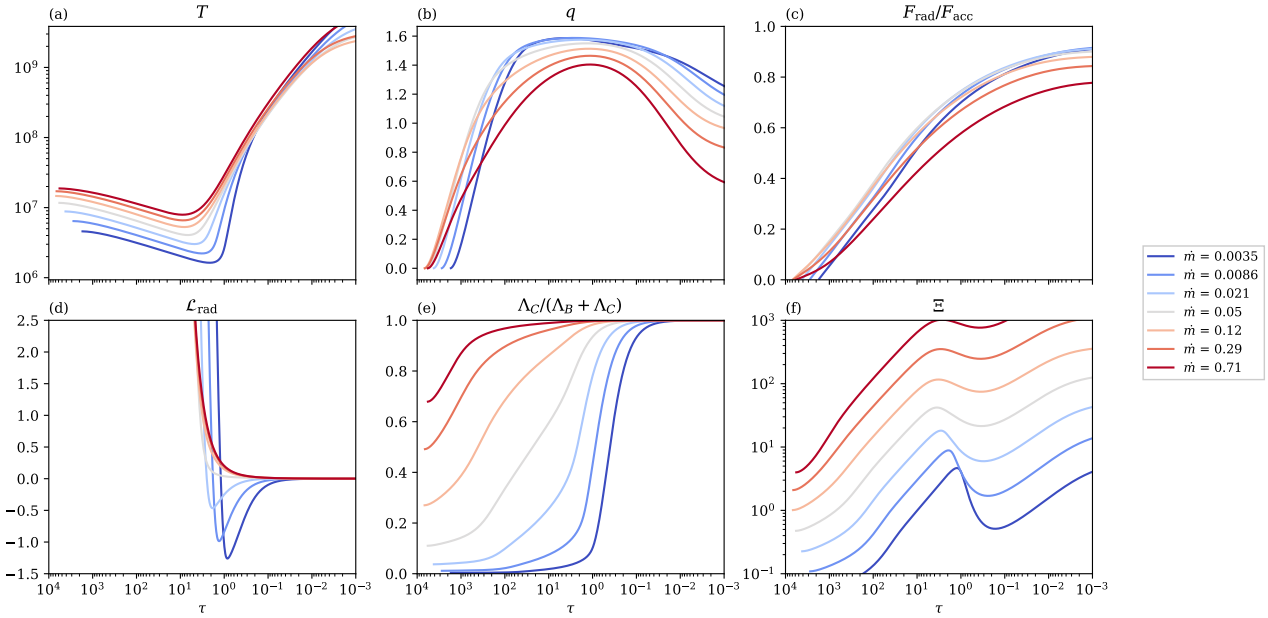

Fig. 7. Vertical structure of the disk-corona models computed at $R = 10\,R_{\rm Schw}$ for different values of the accretion rate ($\dot{m}$), plotted against the total optical depth τ. The panels show (*a*) the gas temperature, (*b*) the gradient of the magnetic pressure (Eq. (34)), (*c*) the radiative energy flux normalized to the total accretion flux $F_{\rm acc}$, (*d*) the cooling function gradient (Eq. (37)), (*e*) the contribution of Compton cooling to the total cooling, and (*f*) the ionization parameter Ξ (Eq. (43)).

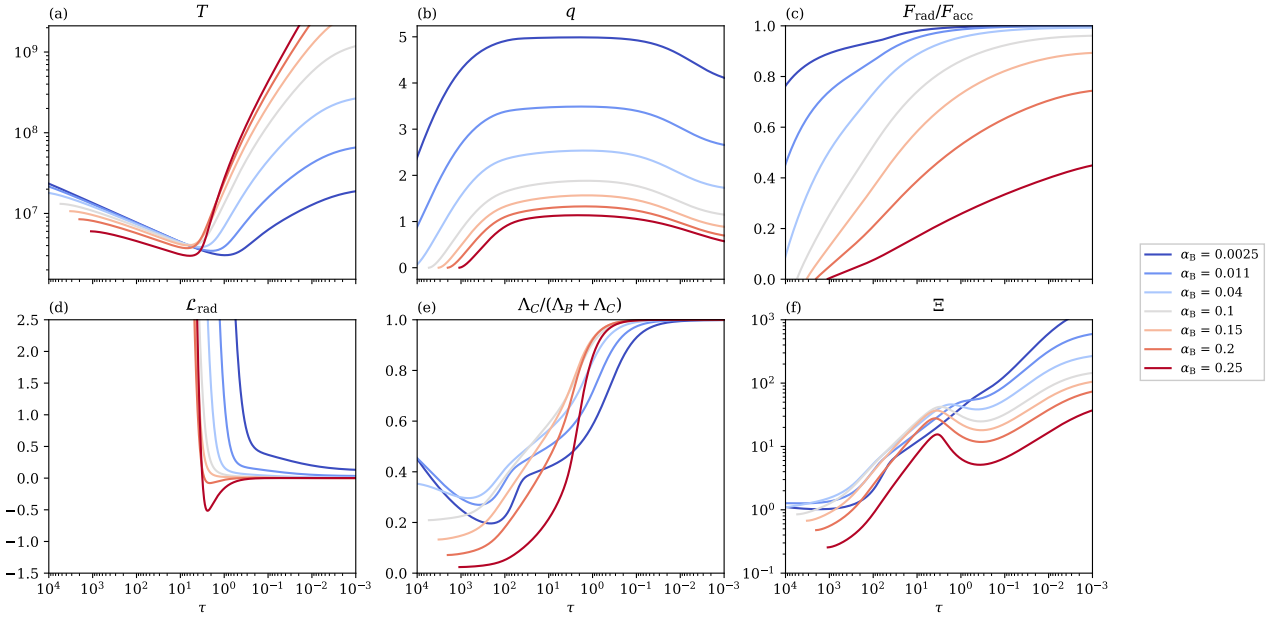

Fig. 8. Same as in Fig. 7, but for different values of the magnetic parameter $\alpha_{\rm B}$.

the weak field, the disk is much hotter and the radiation flux almost saturates to its maximum value well inside the disk (panel c), blue line, in contrast to the strong field case, where the disk is much colder, and more than half of the thermal energy is released in the corona above $\tau = 1$ (panel c), red line. For the corona the temperature behavior is exactly opposite.

When magnetic pressure play a dominant role in the corona, it changes as $P_{\rm mag} \propto z^{-\tilde{q}}$, the density changes as $\rho \propto z^{-(\tilde{q}+1)}$, and the heating rate changes as $\mathcal{H} \propto z^{-\tilde{q}}$. High values of q mean a very steep decline in magnetic field strength and gas heating rate, which in turn means that most of the energy will be dissipated within the disk, and the corona will be weak. This behavior is nicely demonstrated in panel b of Fig. 8. A stronger magnetic field adds to the effective disk cooling and consequently results in the appearance of thermal instability in disk-corona transition (panel d). Despite large temperature differences, Ξ within the disk remains almost constant (panel e), while in the corona it decreases with magnetization even if the coronal temperature is higher.

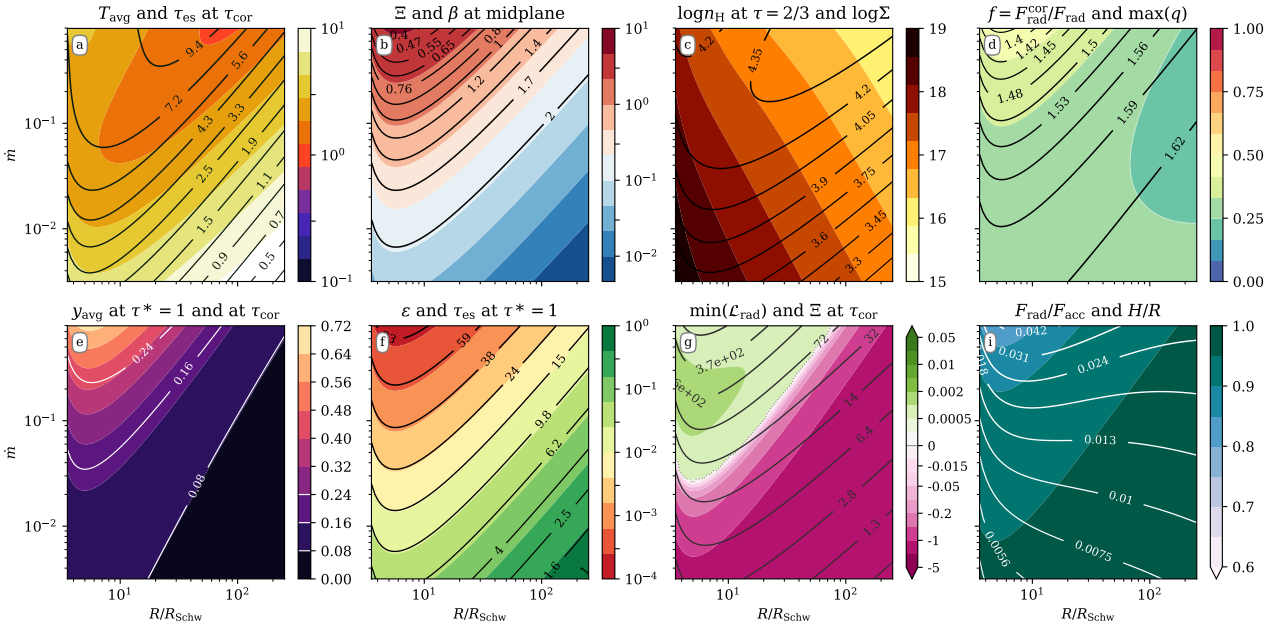

Fig. 9. Properties of the corona on the radius (R/R_{schw}) – accretion rate ($\dot{m}$) parameter plane. All models are calculated for $M_{BH} = 10M_{\odot}$, $\alpha_B = 0.1$, and $\xi = 0.05$. The panels display (*a*) the average temperature of the corona (Eq. (44)) in keV (colors) and τ_{cor} (contours); (*b*) the ionization parameter Ξ (colors) and magnetic β parameter (contours), both at the disk midplane; (*c*) the number density at $\tau = 2/3$ (colors) and the total column density Σ in g cm^2 (contours); (*d*) the fraction of radiative energy produced by the corona f (Eq. (45), colors), the maximum value of the magnetic field gradient q (Eq. (35), contours); (*e*) the y parameter of the warm corona (Eq. (46)), computed up to the thermalization layer $\tau^{\star} = 1$ (colors) and to τ_{cor} (contours); the (*f*) photon destruction probability $\epsilon = \kappa^{P}_{ff}/\kappa^{P}$ (colors) and electron scattering optical depth (τ_{es}) (contours) at the thermalization layer; (*g*) the minimum value of $\mathcal{L}_{rad}$ (Eq. (37)) throughout the disk height (colors), here, green areas are stable disks, and magenta areas indicate thermal instability in the corona, the gray dotted line corresponds to $\mathcal{L}_{rad} = 0$, and the ionization parameter Ξ at the corona base (contours); and (*h*) the radiative energy flux normalized to the total accretion flux (colors), and the disk scale ratio H/R (contours).

3.5. Global properties of the corona

To analyze the global behavior of our model within the parameter space, we define below several diagnostic quantities as proxies for various properties of the disk-corona system. We intended to select these quantities so that they can be compared to observables. The maps in Figs. 9–11 present these diagnostics depending on distance from the black hole R/R_{schw}, accretion rate $\dot{m}$, and α_B parameter.

Similarly to RMB15, and opposite to most models, our corona does not have a constant temperature, but changes with the optical depth, reaching temperature minimum at τ_{cor}. From X-ray spectral fitting we measure some averaged temperature of the warm medium cooled by Comptonization, therefore it is useful to define the average temperature of the corona as

$$T_{avg} = \tau^{-1} \int_0^{\tau_{cor}} T \mathrm{d}\tau' \tag{44}$$

with the aim to compare it with observations. Both quantities T_{avg} and τ_{cor} are shown in each panel a of three maps. A warm optically thick corona tends to form above the inner strongly magnetized disk of high accretion rate.

Analogously to Haardt & Maraschi (1991), we denote the fraction of thermal energy released in the corona (versus total thermal energy) as

$$f = \frac{F^{cor}_{rad}}{F^{tot}_{rad}} = 1 - \frac{F^{disk}_{rad}}{F^{tot}_{rad}} \cdot \tag{45}$$

$f = 0$ corresponds to the passive corona, and $f = 1$ corresponds to passive disk. This parameter is shown in panel d and is tightly correlated with the magnetic field gradient q (Eq. (35)), plotted with contours. Because f is dependent only on magnetic parameters, we suggest that a strong magnetic field is required to obtain the high values of f that are reported by observations. Although we never approach $f \approx 1$ and therefore cannot reproduce the passive-disk scenario discussed by Petrucci et al. (2013, 2018) for the case of AGN, we show that up to half of the total accretion energy can be dissipated in the corona.

Another useful quantity is the Compton y parameter, which can also be determined from observations. To derive the y value for our corona, we used the following definition, which incorporates an additional term that accounts for optically thick medium:

$$y_{avg} = \int_0^{\tau_{es}} \frac{4k(T - T_{rad})}{m_e c^2} (1 + 2\tau'_{es}) \mathrm{d}\tau'_{es}. \tag{46}$$

The value of this parameter is shown in panels e of Figs. 9–11 and can range between 0 and 0.5. This is consistent with the values obtained from observations of X-ray binaries: $y \approx 0.3$ (Życki et al. 2001), $y \approx 0.4$ (Goad et al. 2006), and up to $y \sim 1$ (Zhang et al. 2000).

All these quantities (τ_{cor}, T_{avg}, f , and y_{avg}) positively correlate both the with magnetic field strength and with the released accretion power. This means that the most prominent corona would be observed in the case of a high accretion rate and a strong field. However, above some threshold of disk magnetization (around $\alpha_B = 0.2$, which corresponds to $q \approx 1.3$), the trend reverses, and magnetic flux escapes without releasing all of its energy into radiation, as is shown in panel i of Figs. 10 and 11.

In the case of GBHBs, where the disk temperatures are generally high, the optical depth of the corona τ_{cor} is not usually

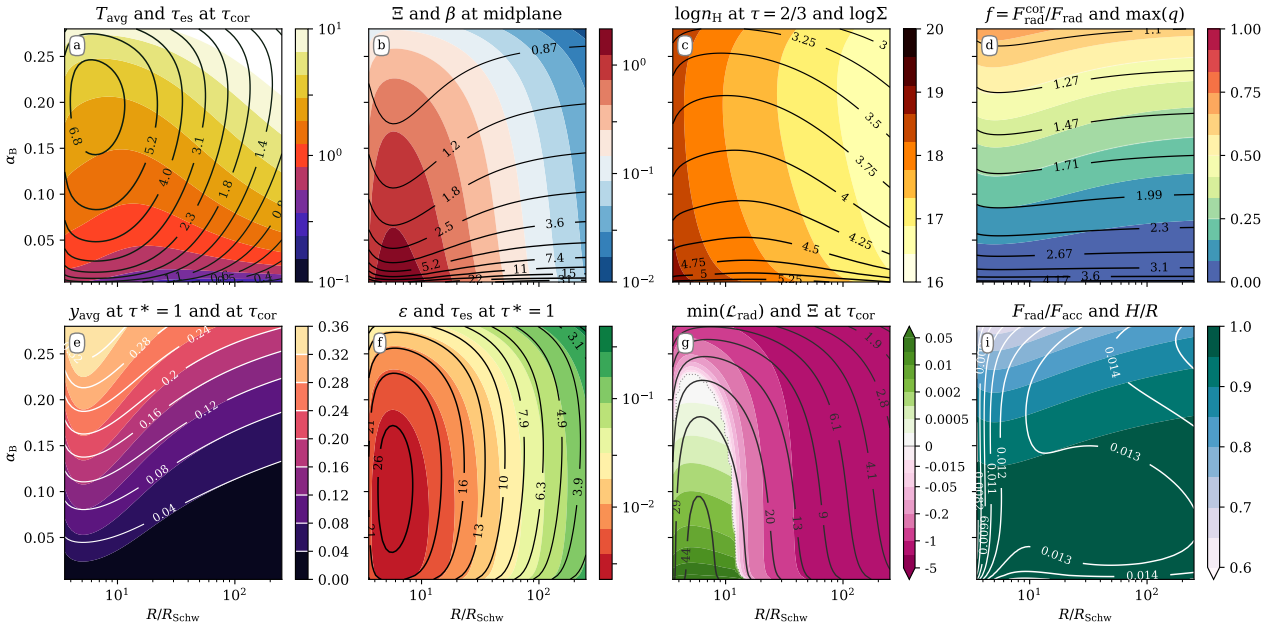

Fig. 10. Same as in Fig. 9, but on the radius (R/R_{schw}) – toroidal field production parameter (α_B) plane.

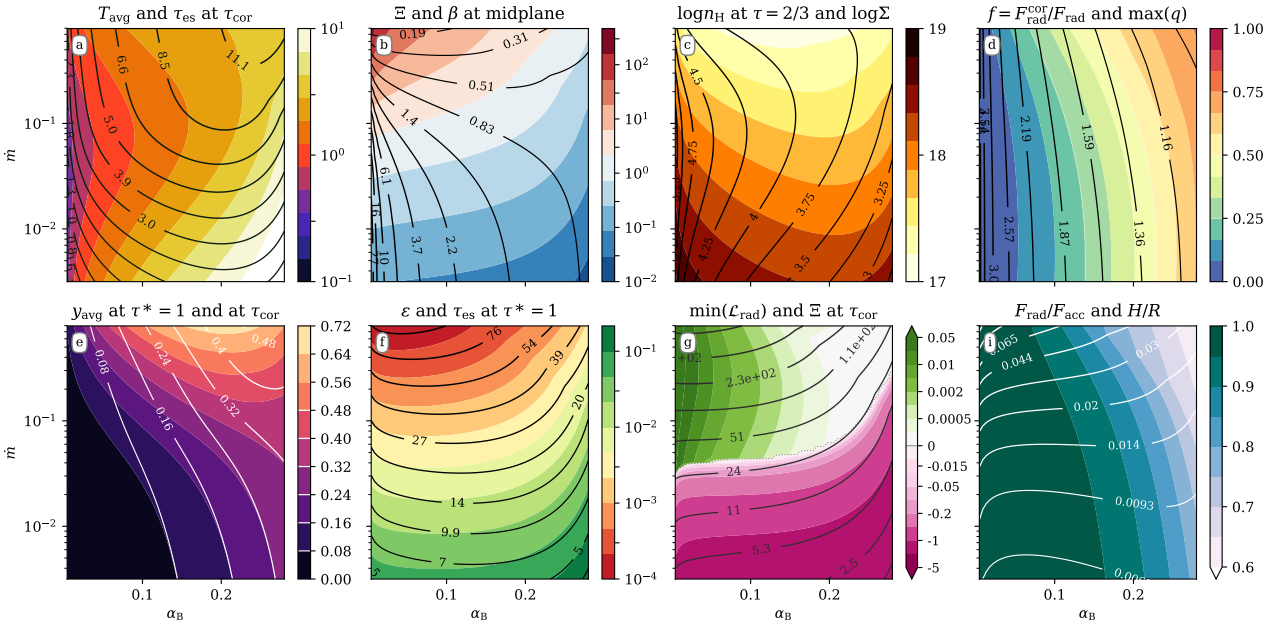

Fig. 11. Same as Fig. 9, but on toroidal field production parameter (α_B) – accretion rate ($\dot{m}$) plane.

limited by a thermalization layer $\tau^\star = 1$ because the medium is strongly scattering dominated, as presented in panel f of Fig. 9. The electron-scattering optical depth of this layer is usually ten times higher than τ_{cor} for the parameters considered here. Photons become thermalized due to high free-free absorption, as we show in comparison to the total Planck opacity in the same panel.

Even if the corona might exist as a solution, thermal instability will occur in many cases, as discussed in Sects. 3.3 and 3.4. Panels g of Figs. 10 and 11 show the stability of the warm corona solutions. The dependence on accretion power is very abrupt and almost switch-like: if the matter becomes too cold or too dense and the contribution of bremsstrahlung cooling accordingly increases, thermal instability occurs, and the corona cannot exist as a stable uniform layer (magenta regions). The same effect is obtained when the magnetic field strength increases and the disk becomes colder (compare with Fig. 8), but the transition is less sensitive and more gradual. The instability appears mostly in cold disk regions, that is, for a low accretion rate and a high magnetic field, and will remove only the optically thick skin when bremsstrahlung contribution is significant, and will most likely not affect the optically thin hot corona, which will

still be present, even if its optical depth may vary with radius and accretion rate. This result, particularly the existence of the corona only around the zone of the maximum energy dissipation rate (around $R/R_{\rm schw} = 10$) is consistent with Kusunose & Mineshige (1994).

The disk thickness $d = H/R$, where H is defined by Eq. (36), is shown in panels i of the figure maps. It ranges between 10^{-3} and 10^{-1}, which means that we still remain in thin-disk regime, consistent with the assumption. It is important to note that the disk thickness changes mostly with the accretion rate. The increase in magnetic field strength does not inflate the disk (Fig. 11i) when the radiative pressure is included, as the fraction of energy that is dissipated within the disk decreases (panel d), and a disk core that is supported by radiative pressure (as in a classical α-disk) is not present, as shown by the radiative to gas pressure ratio Ξ in panel b. Similarly, the total column density Σ, shown by contours in panels c, is decreased because the magnetic fields take over the role of supporting the disk structure.

4. Discussion and conclusions

A disk with an optically thick corona is a frequently used satisfactory representation of the accretion sources in the soft state, and we self-consistently modeled this structure here, based on first principles. Using a semi-analytical static model of the magnetically supported disk (MSD) with radiation, we developed a new relaxation numerical code to calculate the disk-corona transition. The relaxation method designed by us and described in Appendix A is general (Henyey et al. 1964) and solves any set of linear differential equations with assumed boundary conditions. For the case of an accretion disk with a corona, we solved a set of five equations, four of which are differential and one is algebraic, with four boundary conditions (Sect. 2.3).

Our code fully solves the vertical structure, taking into account that part of the magnetic energy generated in the MRI process is converted into radiation and can be dissipated in the warm Compton-cooled corona. The remaining part of the magnetic flux is channeled into a toroidal magnetic field and escapes from the system, as introduced by BAR15. The original model proposed by BAR15 included no energy balance checking or radiative transfer, however, which allowed reducing the model to dimensionless equations. In this paper, we combined the MSD of these authors with solving the radiation transfer through the gray atmosphere in radiative and hydrostatic equilibrium. Additional mean opacities due to free-free absorption are taken into account.

In case of GBHBs with a black hole of stellar mass, we were able to reproduce both an optically thick and thin corona, which is commonly detectable in observations of accreting sources. In contrast to our previous paper (RMB15), where coronal heating was artificially assumed and kept constant with height, here we obtained a self-consistent transition through all three layers: (i) a deep accretion disk up to a few scale heights that is dense and fully thermalized, (ii) a warm corona, where magnetic pressure slows the density decrease and the temperature slowly starts to increase, and (iii) a hot Corona where the density is low. Compton cooling is fully taken into account in all layers, but it strives against free-free cooling depending on the local physical gas conditions (see panel e in Figs. 7 and 8).

The base of the corona at temperature minimum $\tau_{\rm cor}$ may reach 10 electron scattering optical depths, while the thermalization zone can be even 60 times $\tau_{\rm es}$ (panels a and f in Figs. 9–11). This agrees with some observations of a warm Compton-thick corona (Zhang et al. 2000; Życki et al. 2001). The temperature, optical depth, and energetic output of the corona are dependent on distance from the black hole, accretion rate, and toroidal magnetic field strength. A high accretion rate and a strong toroidal field are favorable conditions for the development of a warm $\sim 5\,$keV and optically thick $\tau_{\rm cor} \sim 11$ corona, as shown in the upper left corner of panel a in Fig. 11 .

The magnetic field strength, β_0, seems to have a leading role in regulating the formation of the corona because the energy is stored very efficiently in the poloidal magnetic field near the equatorial plane, and the Poynting flux, $F_{\rm mag}$, quickly increases, reaching its maximum value at approximately $z/H \sim 2$ for the case presented in Fig. 4, panel d. At this point, the magnetic energy stored in the outflowing field is gradually released by heating the gas. Farther out in the atmosphere, this heating rate exceeds the magnetic energy gain from the toroidal field production (MRI). Asymptotically, the Poynting flux will fully convert into the radiation flux, but practically, this convergence may be very slow in some cases (particularly for strongly magnetized disks, where the magnetic pressure declines slowly with height). Therefore, the magnetic pressure gradient q (Eq. (34)) is an important quantity that influences the release of magnetic energy and in consequence, the formation of the corona (see panel b) in Figs. 7 and 8. A stronger toroidal field, that is, a lower β_0, implies a milder gradient and more accretion energy that is transported from the disk to the atmosphere by Poynting flux. This is nicely demonstrated in panel b of Fig. 11, where the values of β_0 are lowest, and where the warm corona has the highest optical thickness (panel a) of the same figure. On the other hand, the radiative flux $F_{\rm rad}$ will never saturate asymptotically to a constant value for $q \leq 1$ (see panels d) and i in Fig. 11.

However, an optically thick corona may be subject to local thermal instability caused by contribution of free-free opacity in the transition layer. These instabilities have been problematic in radiative transfer computations of accretion disk atmospheres of AGN for decades (Krolik & Kriss 1995; Nayakshin et al. 2000; Różańska et al. 2002, 2015). We were expecting that in case of hotter disks around black holes of stellar mass those instabilities would be absent, and in addition, magnetic heating might remove them. Our results show the opposite, however: a stronger field expands in the corona vertically and at the same time prevents formation of a very hot disk that is supported by radiation pressure, which might be sensitive to thermal instabilities. When this happens, two outcomes are possible: the sharp transition between cold and hot phase will be smoothed out by thermal conduction and form a relatively plain and regular atmosphere (Różańska 1999), or prominence-like clumps of dense matter will form, and will coexist at the same level with hot medium, similar to lower solar corona. The clumps could condense or simply emerge from the disk, pulled by magnetic field buoyancy (Fig. 1 in Jiang et al. 2014). Given the violent and turbulent nature of an assumed engine that powers the disk (MRI), the clumpy two-phase medium interpretation seems more likely, but also poses a huge challenge for spectrum modeling. Variations of this scenario that often consider not only a corona but an entire disk that is clumpy have been discussed in the literature (Schnittman & Krolik 2010; Yang et al. 2015; Wu et al. 2016). Regardless of the interpretation, we show that thermal instability occurs in very many cases, even though GBHB disks are hot and dense and not as prone to it as AGN disks.

Although thermal instability affects the very same transition region that is responsible for producing optically thick corona, our model places constraints on the parameters for which a warm or hot corona can exist. For this purpose, we drew the radial extension of the corona base determined by the usual temperature minimum when no thermal instability is present, or by the

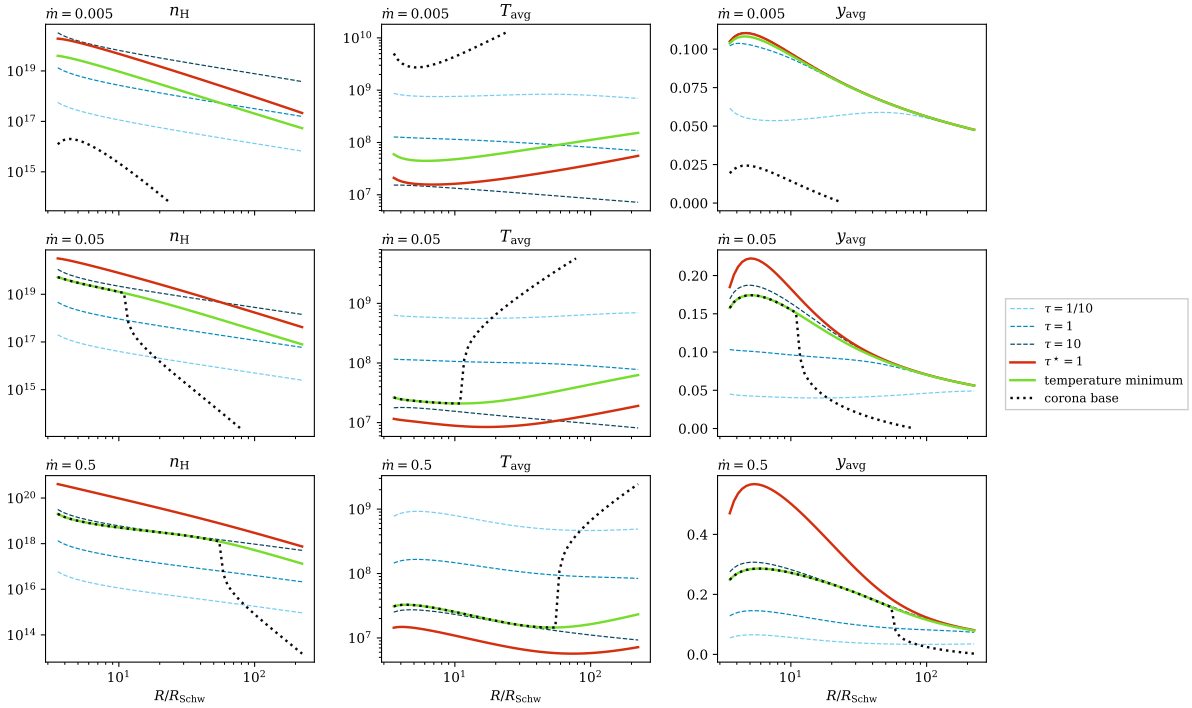

Fig. 12. Radial profiles of selected quantities: gas density ρ [cm^{-3}], average temperature T_{avg} [K] , and average Compton y_{avg} (Eq. (46)), measured at different depths in the disk atmosphere. Values at $\tau = 0.1$, $\tau = 1$, and $\tau = 10$ are shown by dashed blue lines, at temperature minimum (τ_{cor}) by the green line, at thermalization depth by the red line, and at the corona base (determined by temperature minimum or thermal instability in case it is developed) with the black dotted line.

temperature of the upper stable branch where thermal instability starts to developed (the cross point in the upper panels of Fig. 6) with the black dotted line in Fig. 12. The gas density, average temperature, and the radial profiles of the Compton parameter at selected optical depths for three accretion rates are shown in Fig. 12.

When the accretion rate is low, thermal instability arises at each distance from the black hole and only a hot corona appears, which is four orders of magnitude less dense than the disk atmosphere (three upper panels of Fig. 12). A corona like this would be optically thin, and the transition between disk and corona occurs at about $z/H \sim 20$, as demonstrated in the upper panels of Fig. 6. For $\dot{m} = 0.05$, a warm stable corona can form up to $R \sim 10\,R_{Schw}$, and this corona is dense and optically thick, reaching at the base almost $\tau_{es} \sim 10$ (three middle panels of Fig. 12). Nevertheless, farther out from the black hole, thermal instability arises and a stable corona is again very hot and rare. Such a hot and rare outer corona dissipates only about 1% of the local energy and cannot be associated with the usual hard X-ray corona observed in accreting sources. Finally, for a high accretion rate $\dot{m} = 0.5$, the radial extent of the warm corona is the largest $\sim 60\,R_{Schw}$ and optical depth $\tau_{es} = 10$. Thermal instability and a hot stable corona appear farther away from the black hole. Our results strongly indicate that a warm optically thick corona tends to develop in the innermost disk regions, while the outer disk is covered only by a rare hot corona. Furthermore, a warm corona is more radially extended for disks of high accretion rates. This feature explains why we see soft X-ray excess only in the most luminous accreting sources.

Our model predicts a corona formation that is adjusted self-consistently by model parameters, therefore it places constraints on several quantities that can be directly compared with observations. The fist straightforward outcome is that the value of the temperature T_{avg} is in the range from 0.1–10 keV. The second constrained parameter is the density of the warm corona, which arises from the dense disk atmosphere. The predicted density from our model is about 10^{16-20} cm^{-3}. This density is very high, but it agrees with the density of the ionized outflow in accreting black holes that was determined from observations by Miller et al. (2014). Our model supports the scenario that eventually, a disk wind can arise from the upper dense layers of a magnetically driven accretion disk atmosphere.

The most important observable is the ratio of the thermal energy that is released in the corona f in comparison to the total energy that is generated in the system. This ratio is always higher than zero because we computed a Compton-cooled atmosphere, which is characterized by typical temperature inversion with increasing optical depth (Różańska et al. 2011). In the frame of our model, we showed that up to half of the total accretion energy can be dissipated in the corona in case of GBHBs (up to f = 0.75 for the highest value of α_B), therefore we are not able to reproduce the passive-disk scenario discussed by Petrucci et al. (2013, 2018) for the case of AGN. This is a natural consequence of our assumed heating mechanism, which can transport a large portion of energy to the corona, but requires very effective magnetic coupling with gas down to the equatorial plane. The value of the Compton parameter averaged over the optical depth of the warm corona we determined with our model is consistent with the values determined from X-ray observations of several GBHBs: $y \approx 0.3$ (Życki et al. 2001), $y \approx 0.4$ (Goad et al. 2006), up to $y \sim 1$ (Zhang et al. 2000).

One of the main postulates of the BAR15 model is that it can explain the spectral state transition of the X-ray binary that is observed in many sources (e.g., Yamada et al. 2013) by a smooth

transition from the soft to hard state by introducing an intermediate dead zone between the disk and the coronal accretion flow. They used the condition for MRI shutoff when the gas energy is not high enough to sustain the dynamo (Pessah & Psaltis 2005). In our model, we considered only one zone where MRI is always operating. We suggest here that the spectral state transition should occur depending on the strength and radial extension of the warm optically thick corona rather than the full MRI shutoff. In the frame of our model we did not consider the transition from optically thick disk to inner advection-dominated accretion flow.

As discussed in BAR15 and SSAB16, one of the key features of MSDs is that they require a strong global poloidal magnetic field for the magnetic dynamo to operate and generate the toroidal field that supports the disk. In case of our typical model $\alpha_{\rm B} = 0.1$, the toroidal magnetic field in the equatorial plane and at the base of corona typically is about 10^8 G in the inner disk region and of 10^5 G for radii above $70\,R_{\rm Schw}$. These values are lower than those detected in pulsars, but they fully agree with the prediction for the poloidal magnetic filed value that is required for the jet-launching mechanism.

Studies suggest that a poloidal magnetic fields is important in jet-launching mechanisms (see also Beckwith et al. 2009; McKinney et al. 2012; Liska et al. 2018). Zhang et al. (2000) noted that in both objects where an optically thick corona was observed, jets were also present. Our study shows that the most prominent warm corona will occur in a state when the dynamo is very effective (high $\alpha_{\rm B}$) and the contribution of the magnetic field to the disk structure is high (low β_0). On the other hand, no jet was observed in Mrk 509 (Petrucci et al. 2013). Nevertheless, the case of AGN will be presented in a forthcoming paper.

Acknowledgements. We thank Bożena Czerny for all comments and helpful discussion. This research was supported by Polish National Science Center grants No. 2015/17/B/ST9/03422 and 2015/18/M/ST9/00541.

References

Anderson, E., Bai, Z., Dongarra, J., et al. 1990, in Proceedings of the 1990 ACM/IEEE Conference on Supercomputing, Supercomputing '90 (Los Alamitos, CA, USA: IEEE Computer Society Press), 2
Bai, X.-N., & Stone, J. M. 2013, ApJ, 767, 30
Balbus, S. A., & Hawley, J. F. 1991, ApJ, 376, 214
Ballantyne, D. R., Ross, R. R., & Fabian, A. C. 2001, MNRAS, 327, 10
Beckwith, K., Hawley, J. F., & Krolik, J. H. 2009, ApJ, 707, 428
Begelman, M. C., & Pringle, J. E. 2007, MNRAS, 375, 1070
Begelman, M. C., Armitage, P. J., & Reynolds, C. S. 2015, ApJ, 809, 118
Di Salvo, T., Done, C., Życki, P. T., Burderi, L., & Robba, N. R. 2001, ApJ, 547, 1024
Done, C., Davis, S. W., Jin, C., Blaes, O., & Ward, M. 2012, MNRAS, 420, 1848
García, J. A., Kara, E., Walton, D., et al. 2019, ApJ, 871, 88
Gierliński, M., & Done, C. 2004, MNRAS, 349, L7
Gierliński, M., Zdziarski, A. A., Poutanen, J., et al. 1999, MNRAS, 309, 496
Gladstone, J. C., Roberts, T. P., & Done, C. 2009, MNRAS, 397, 1836
Goad, M. R., Roberts, T. P., Reeves, J. N., & Uttley, P. 2006, MNRAS, 365, 191
Haardt, F., & Maraschi, L. 1991, ApJ, 380, L51
Hawley, J. F. 2001, ApJ, 554, 534
Hawley, J. F., & Balbus, S. A. 1991, ApJ, 376, 223
Henyey, L. G., Forbes, J. E., & Gould, N. L. 1964, ApJ, 139, 306
Hirose, S., Krolik, J. H., & Stone, J. M. 2006, ApJ, 640, 901
Hirose, S., Krolik, J. H., & Blaes, O. 2009, ApJ, 691, 16
Jiang, Y.-F., Stone, J. M., & Davis, S. W. 2014, ApJ, 784, 169
Jin, C., Ward, M., Done, C., & Gelbord, J. 2012, MNRAS, 420, 1825
Keek, L., & Ballantyne, D. R. 2016, MNRAS, 456, 2722
Krolik, J. H., & Kriss, G. A. 1995, ApJ, 447, 512
Krolik, J. H., McKee, C. F., & Tarter, C. B. 1981, ApJ, 249, 422
Kusunose, M., & Mineshige, S. 1994, ApJ, 423, 600
Laor, A., Fiore, F., Elvis, M., Wilkes, B. J., & McDowell, J. C. 1994, ApJ, 435, 611
Laor, A., Fiore, F., Elvis, M., Wilkes, B. J., & McDowell, J. C. 1997, ApJ, 477, 93
Liska, M. T. P., Tchekhovskoy, A., & Quataert, E. 2018, ArXiv e-prints [arXiv:1809.04608]
Madau, P. 1988, ApJ, 327, 116
Madej, J., & Różańska, A. 2004, MNRAS, 347, 1266
Magdziarz, P., Blaes, O. M., Zdziarski, A. A., Johnson, W. N., & Smith, D. A. 1998, MNRAS, 301, 179
McKinney, J. C., Tchekhovskoy, A., & Blandford, R. D. 2012, MNRAS, 423, 3083
Mehdipour, M., Branduardi-Raymont, G., Kaastra, J. S., et al. 2011, A&A, 534, A39
Meurer, A., Smith, C. P., Paprocki, M., et al. 2017, PeerJ Comput. Sci., 3, e103
Miller, J. M., Raymond, J., Kallman, T. R., et al. 2014, ApJ, 788, 53
Nakamura, K., & Osaki, Y. 1993, PASJ, 45, 775
Nayakshin, S., & Kallman, T. R. 2001, ApJ, 546, 406
Nayakshin, S., Kazanas, D., & Kallman, T. R. 2000, ApJ, 537, 833
Noble, S. C., Krolik, J. H., Schnittman, J. D., & Hawley, J. F. 2011, ApJ, 743, 115
Ohsuga, K., & Mineshige, S. 2011, ApJ, 736, 2
Penna, R. F., Kulkarni, A., & Narayan, R. 2013, A&A, 559, A116
Pessah, M. E., & Psaltis, D. 2005, ApJ, 628, 879
Petrucci, P.-O., Paltani, S., Malzac, J., et al. 2013, A&A, 549, A73
Petrucci, P. O., Ursini, F., De Rosa, A., et al. 2018, A&A, 611, A59
Piconcelli, E., Jimenez-Bailón, E., Guainazzi, M., et al. 2005, A&A, 432, 15
Pounds, K. A., Stanger, V. J., Turner, T. J., King, A. R., & Czerny, B. 1987, MNRAS, 224, 443
Proga, D., & Waters, T. 2015, ApJ, 804, 137
Różańska, A. 1999, MNRAS, 308, 751
Różańska, A., & Czerny, B. 1996, Acta Astron., 46, 233
Różańska, A., Czerny, B., Życki, P. T., & Pojmański, G. 1999, MNRAS, 305, 481
Różańska, A., Dumont, A.-M., Czerny, B., & Collin, S. 2002, MNRAS, 332, 799
Różańska, A., Madej, J., Konorski, P., & Sądowski, A. 2011, A&A, 527, A47
Różańska, A., Malzac, J., Belmont, R., Czerny, B., & Petrucci, P.-O. 2015, A&A, 580, A77
Rybicki, G., & Lightman, A. 2008, Radiative Processes in Astrophysics, Physics Textbook (New York: Wiley)
Salvesen, G., Simon, J. B., Armitage, P. J., & Begelman, M. C. 2016, MNRAS, 457, 857
Sądowski, A., Wielgus, M., Narayan, R., et al. 2017, MNRAS, 466, 705
Schnittman, J. D., & Krolik, J. H. 2010, ApJ, 712, 908
Schnittman, J. D., Krolik, J. H., & Noble, S. C. 2016, ApJ, 819, 48
Seifina, E., Titarchuk, L., & Shaposhnikov, N. 2016, ApJ, 821, 23
Seifina, E., Chekhtman, A., & Titarchuk, L. 2018, A&A, 613, A48
Shakura, N. I., & Sunyaev, R. A. 1973, A&A, 24, 337
Shaposhnikov, N., & Titarchuk, L. 2006, ApJ, 643, 1098
Stobbart, A.-M., Roberts, T. P., & Wilms, J. 2006, MNRAS, 368, 397
Stone, J. M., Gardiner, T. A., Teuben, P., Hawley, J. F., & Simon, J. B. 2008, ApJS, 178, 137
Svensson, R., & Zdziarski, A. A. 1994, ApJ, 436, 599
Tange, O. 2011, The USENIX Magazine, 36, 42
Tout, C. A., & Pringle, J. E. 1992, MNRAS, 259, 604
Turner, N. J. 2004, ApJ, 605, L45
Wu, M.-C., Xie, F.-G., Yuan, Y.-F., & Gan, Z. 2016, MNRAS, 459, 1543
Yamada, S., Torii, S., Mineshige, S., et al. 2013, ApJ, 767, L35
Yang, Q.-X., Xie, F.-G., Yuan, F., et al. 2015, MNRAS, 447, 1692
Zhang, S. N., Cui, W., Chen, W., et al. 2000, Science, 287, 1239
Życki, P. T., Done, C., & Smith, D. A. 2001, MNRAS, 326, 1367

Appendix A: Numerical procedure

The solution of the set of five equations with four boundary conditions described in the previous sections allows determining the density ρ, gas temperature $T_{\rm gas}$, radiation pressure $P_{\rm rad}$, radiative flux $F_{\rm rad}$, and magnetic pressure $P_{\rm mag}$ at each point of the vertical profile. The requirement of satisfying four boundary conditions, two on each side of the computational interval, requires multiple iterations when shooting methods such as a Runge-Kutta scheme are used. Moreover, the equations are highly nonlinear, and keeping the integration error low requires a high number of grid points (up to 10^5), even using a fourth-order Runge-Kutta scheme. Although the computation time using a shooting method is still less than a few minutes, it becomes a problem when the global behavior over the parameter space is investigated, which requires computing thousands of models for different disk and magnetic parameters. Therefore, to solve this issue, we developed a variant of the relaxation method that was originally described by Henyey et al. (1964) for stellar evolution problems.

The relaxation methods are iterative, when iterations are made for the functions defined in the whole argument space. In the first step, some approximate solution for the functions, which might be close to the exact solution, is needed. Then by applying the procedure described below, the correction to the entire profile is obtained and added to the original solution. Because we have many strongly nonlinear terms in our equations while the method is intrinsically linear, we applied a reduction factor for these corrections in the first few iterations to avoid overshooting. The new solution was then used as input to the next step and the iteration continued until the mean relative value of the obtained correction fell below 10^{-7}, which we consider a convergence criterion.

To apply the relaxation method to our problem, define a grid of N points, in each we have five physical quantities. We introduce the following notation: the quantity $j = 1 \dots 5$ in point $i = 1 \dots N$ is denoted X_i^j. We can also represent it as a vector with five components:

$$\boldsymbol{X}_i \equiv \left[\rho_i, T_i^{\rm gas}, T_i^{\rm rad}, F_i^{\rm rad}, P_i^{\rm mag}\right]. \tag{A.1}$$

Then we discretize the set of all five equations together with the boundary conditions. For nondifferential equations (balance equation and boundary conditions), we evaluate them at the respective grid points, that is, $X^j(z) \to X_i^j$. For all four differential equations we replace quantities with midpoint values and their spatial derivatives with finite differences. As they are evaluated at midpoints, there are only $N - 1$ terms,

$$X^j(z) \to \frac{X_i^j + X_{i+1}^j}{2} \equiv X_{i+1/2}^j, \tag{A.2}$$

$$\left.\frac{dX^j}{\mathrm{d}z}\right|_z \to \frac{X_{i+1}^j - X_i^j}{z_{i+1} - z_i} \equiv Y_{i+1/2}^j. \tag{A.3}$$

The core of the problem is to perturb the entire profile to obtain a new one that is closer to the solution. Using the chain rule, we can express the computed profile in terms of perturbations to actual physical quantities:

$$\delta A_i^k = \sum_{j=1}^{5} \sum_{l=1}^{N} \frac{\partial A_i^k}{\partial X_l^j} \delta X_l^j = -A_i^k, \tag{A.4}$$

where $i = 1 \dots N - 1$ and $k = 1 \dots 5$. Most of the terms in this sum are zero because equations evaluated at point i depend only on quantities in points i and $i + 1$, thus $l \in \{i, i + 1\}$. The goal of the relaxation method is to transform all equations where $A_i^k = 0$, which means that each of the equations $k = 1 \dots 5$ is satisfied in each point $i = 1 \dots N$. However, having started from some initial guess, this is more likely not true, and the remainder $A_i^k \neq 0$.

Analogically, we do the same for boundary conditions. When we denote the remaining lower boundary conditions as L and upper boundary conditions as U, the expansions in terms of perturbations with respect to variables yield

$$\delta L^k = \sum_{j=1}^{5} \frac{\partial L^k}{\partial X_1^j} \delta X_1^j = -L^k \quad \text{where } k = 1, 2, \tag{A.5}$$

$$\delta U^k = \sum_{j=1}^{5} \frac{\partial U^k}{\partial X_N^j} \delta X_N^j = -U^k \quad \text{where } k = 1, 2. \tag{A.6}$$

At this point we have a mathematically well-defined problem: we must solve Eqs. (A.4)–(A.6) to obtain the profile corrections $\delta X_{1\dots N}^{1\dots 5}$. We can express it as the perturbation vector $\delta \boldsymbol{X}$, remainder vector $\boldsymbol{R}$ and Jacobian matrix $\mathbf{M}$:

$$\mathbf{M} \cdot \delta \boldsymbol{X} = -\boldsymbol{R}. \tag{A.7}$$

We arrange our five variables and five equations into a vector using the following layout:

$$X_{5i-5+j} = X_i^j \quad \text{where } j = 1 \dots 5 \text{ and } i = 1 \dots N, \tag{A.8}$$

$$R_k = L^k \quad \text{where } k = 1, 2, \tag{A.9}$$

$$R_{5i-3+k} = A_i^k \quad \text{where } k = 1 \dots 5 \text{ and } i = 1 \dots N, \tag{A.10}$$

$$R_{5N-2+k} = U^k \quad \text{where } k = 1, 2. \tag{A.11}$$

Now the remaining issue is to fill the matrix accordingly. For linear equations, to evaluate all nonzero matrix terms for $i = 1 \dots N$, $j = 1 \dots 5$, $k = 5$ and $l = i$, we directly use the formula

$$M_{pq} = \frac{\partial A_i^k}{\partial X_l^j}, \quad \text{where} \quad \begin{array}{l} p = 5i - 3 + k \\ q = 5l - 5 + j. \end{array} \tag{A.12}$$

For differential equations, each point depends on two consecutive points, and we evaluate these terms for $i = 1 \dots N - 1$, $j = 1 \dots 5$, $k = 1 \dots 4$ and $l \in \{i, i + 1\}$ using the chain rule:

$$\frac{\partial A_i^k}{\partial X_i^j} = \frac{\partial X_{i+1/2}^j}{\partial X_i^j} \frac{\partial A_i^k}{\partial X_{i+1/2}^j} + \frac{\partial Y_{i+1/2}^j}{\partial X_i^j} \frac{\partial A_i^k}{\partial Y_{i+1/2}^j} \tag{A.13}$$

$$= \frac{1}{2} \frac{\partial A_i^k}{\partial X_{i+1/2}^j} - \frac{1}{z_{i+1} - z_i} \frac{\partial A_i^k}{\partial Y_{i+1/2}^j}, \tag{A.14}$$

$$\frac{\partial A_i^k}{\partial X_{i+1}^j} = \frac{\partial X_{i+1/2}^j}{\partial X_{i+1}^j} \frac{\partial A_i^k}{\partial X_{i+1/2}^j} + \frac{\partial Y_{i+1/2}^j}{\partial X_{i+1}^j} \frac{\partial A_i^k}{\partial Y_{i+1/2}^j} \tag{A.15}$$

$$= \frac{1}{2} \frac{\partial A_i^k}{\partial X_{i+1/2}^j} + \frac{1}{z_{i+1} - z_i} \frac{\partial A_i^k}{\partial Y_{i+1/2}^j}. \tag{A.16}$$

Finally, for boundary conditions, we evaluate the matrix coefficients at lower (L) and upper (U) boundary as

$$M_{kj} = \frac{\partial L^k}{\partial X_1^j} \quad \text{where} \quad k = 1, 2, \tag{A.17}$$

$$M_{pq} = \frac{\partial U^k}{\partial X_N^j} \quad \text{where} \quad \begin{array}{l} k = 1, 2 \\ p = 5N - 2 + k \\ q = 5N - 5 + j. \end{array} \tag{A.18}$$

The relaxation method provides excellent precision even for very few computational points because the method adjusts the entire profile at once, allowing us to investigate even marginally stable cases. The method is also clearly expandable for higher-order derivatives.

Its major disadvantage is the requirement that the partial derivatives of the left-hand sides of all equations (and boundary conditions) need to be evaluated with respect to all variables and their spatial derivatives. This makes the code very difficult to modify and error prone. We solved this problem using a symbolic computation techniques within the *sympy* framework (Meurer et al. 2017), which also allowed us to generate ready-to-compile procedures to evaluate the matrix coefficients that we included in our code, which is written in Fortran 2008. We then solved the system of linear equations using the `DGBSV` procedure from *LAPACK* (Anderson et al. 1990) and obtained corrections to all five variables at each point. This method is very fast and allows us to obtain a precise solution in less than half a second on a typical desktop computer.

Chapter 3

Paper II: Thermal instability as a constraint for warm X-ray corona in AGN

A&A 675, A198 (2023)
https://doi.org/10.1051/0004-6361/202244410

Astronomy & Astrophysics

Thermal instability as a constraint for warm X-ray coronas in active galactic nuclei

Dominik Gronkiewicz[1], Agata Różańska[1], Pierre-Olivier Petrucci[2], and Renaud Belmont[3]

[1] Nicolaus Copernicus Astronomical Center, Polish Academy of Sciences, Bartycka 18, 00-716 Warsaw, Poland
e-mail: agata@camk.edu.pl
[2] Université de Grenoble Alpes, IPAG, 621 avenue Centrale, 38400 Saint-Martin-d'Hères, France
[3] Université Paris Cité, Université Paris-Saclay, CEA, CNRS, AIM, 3 rue Joliot Curie, Bâtiment Breguet, 91190 Gif-sur-Yvette, France

Received 1 July 2022 / Accepted 16 May 2023

ABSTRACT

Context. Warm coronas offer a plausible explanation behind the soft X-ray excess in active galactic nuclei (AGNs). This paper presents the self-consistent modeling of an accretion disk with an optically thick corona, where the gas is heated by magneto-rotational instability dynamo (MRI) and is simultaneously cooled by radiation which undergoes free-free absorption and Compton scattering.
Aims. We determined the parameters of a warm corona in an AGN using disk-corona structure model that takes into account magnetic and radiation pressure. We aim to show the role of thermal instability (TI) as a constraint for warm, optically thick X-ray coronas in AGNs.
Methods. With the use of relaxation code, we calculated the vertical solution of the disk driven by MRI, together with radiative transfer in hydrostatic and radiative equilibrium. This has allowed us to point out how TI affects the corona for a wide range of global parameters.
Results. We show that magnetic heating is strong enough to heat the upper layers of the accretion disk atmosphere, which form the warm corona covering the disk. Magnetic pressure does not remove TI caused by radiative processes operating in X-ray emitting plasma. TI disappears only in case of accretion rates higher than 0.2 of Eddington, and high magnetic field parameter $\alpha_{\rm B} > 0.1$.
Conclusions. TI plays the major role in the formation of the warm corona above magnetically driven accretion disk in an AGN. The warm, Compton cooled corona, responsible for soft X-ray excess, resulting from our model typically exhibits temperatures in the range of 0.01–2 keV and optical depths of even up to 50, in agreement with recent observations.

Key words. accretion, accretion disks – radiative transfer – galaxies: nuclei – magnetic fields – instabilities – methods: numerical

1. Introduction

Soft X-ray excess is commonly observed in large majority of active galactic nuclei (AGN; e.g., Pounds et al. 1987; Walter & Fink 1993; Bianchi et al. 2009; Mehdipour et al. 2011; Done et al. 2012; Petrucci et al. 2013, 2018; Keek & Ballantyne 2016) and this includes quasars (Madau 1988; Laor et al. 1994, 1997; Gierliński & Done 2004; Piconcelli et al. 2005). It appears as an excess in emission, when extrapolating the 2–10 keV power law of an AGN to the soft X-ray band.

The origin of this spectral component is still under debate, but two major scenarios are currently under consideration. The first scenario posits that soft X-ray excess is a result of blurred ionized reflection (Crummy et al. 2006; Walton et al. 2013; García et al. 2019), but such a model will produce many lines that are not observed in the soft X-ray band and extreme blurring is generally required to wash them out. Recently, detailed radiative transfer analyses in the warm corona proved that those lines cannot be easily created due to the full domination of internal heating and Compton scattering over the line transitions (Petrucci et al. 2020; Ballantyne 2020).

The second scenario relies on the fact that soft X-ray excess is produced due to the Comptonization in optically thick ($\tau \sim 10-20$) warm corona, which is reasonable assumption while fitting the data (e.g., Magdziarz et al. 1998; Jin et al. 2012; Petrucci et al. 2013, 2018; Porquet et al. 2018, and references therein). Nevertheless, from the data fitting, both scenarios above require the existence of a warm layer that is additionally heated – not only by radiation, but also by a mechanical process – and the warm layer is located next to the accretion disk. On the other hand, none of those models consider how this warm layer is physically caused and only the constant heating over gas volume of the warm corona is assumed and included in model computations as a free parameter (Petrucci et al. 2020; Ballantyne 2020).

Analytically, we have predicted that high optical depth and high temperature of the warm, Compton-cooled corona is possible when additional pressure component and mechanical heating are taken into account (Różańska et al. 2015). Recently, we extended this analytical model by numerical calculations of magnetically heated disk with free-free processes taken into account in addition to Compton scattering in case of the accretion disk around black hole of stellar mass, namely, Galactic black hole binaries (GBHB; Gronkiewicz & Różańska 2020, hereafter GR20). For such sources, an accretion disk is already quite hot, visible in X-rays, and slightly warmer layer can form on different distances from black hole. In GR20, we shown that the warm corona, which is physically fully coupled with the cold, magnetically supported disk (MSD), arises naturally due to magnetic heating. Such corona is cooled mostly by Compton scattering, in agreement with the observations. We clearly

demonstrated that the classical thermal instability (TI; Field 1965; Różańska & Czerny 1996), caused by gas cooling processes, cannot be removed by magnetic pressure and it shapes the radial distance of the warm corona in those objects.

However, the case of AGNs is different, since the disk temperature is relatively cool, on the order of 10^{4-5} K, and the transition to the warm, 10^7 K, X-ray corona is accompanied by strong changing of gas global parameters, such as density and pressure. On the other side, a physically consistent model of a warm corona, responsible for the soft X-ray excess, is desirable, as we have a growing collection of observed sources indicating such a feature obtained with modern X-ray satellites. In this paper, we adopt GR20 model to the case of AGNs, where the geometrically thin and optically thick accretion disk is around the supermassive black hole (SMBH). We assume that the accretion disk is magnetized and the magneto-rotational instability (MRI) is the primary source of viscosity and energy dissipation. We directly use the analytic formula derived by Begelman et al. (2015, hereafter BAR15), where the vertical profile of magnetic heating of the accretion flow is determined. On the top of this assumption, the disk vertical structure together with the radiative transfer equation in gray atmosphere are fully solved with the relaxation method proposed originally by Henyey et al. (1964).

As a results of our computations, we obtained the optical depth and temperature of the warm corona in AGN, which are the main observables when analyzing X-ray data. The specific heating of a warm corona formed in our model, was computed self consistently based on MRI and reconnection. The value of this heating together with the magnetic pressure change in the vertical direction, which is a big improvement with regard the constant heating warm corona slab used in recent calculations of energy spectrum from the warm corona (Petrucci et al. 2020; Ballantyne 2020). The next improvement of our analytical model (Różańska et al. 2015) is the use of free-free radiative process which is crucial for TI to appear. We show, that in the case of AGNs, the magnetic pressure is high enough to produce a stable branch in a classical TI curve obtained under constant gas and radiation pressure condition. A MSD with a warm corona is dominated by magnetic pressure that makes the radiative cooling gradient always positive when computed under constant gas plus magnetic pressure. Therefore, an initially thermally unstable zone, through which the radiative cooling gradient under constant gas pressure is negative, is frozen in the magnetic field, thus allowing the corona to exist. All the results we obtained were then compared with observations of unabsorbed type 1 AGNs (Jin et al. 2012; Petrucci et al. 2013; Ursini et al. 2018; Middei et al. 2019, and references therein) and with models computed in case of GBHB (GR20). We show that the measured parameters agree with those obtained by our numerical computations. Our solutions are prone to TI in a wide range of global parameters, indicating that TI plays a crucial role in soft corona formation in AGN.

The structure of the paper is as follows. Section 2 presents the method of our computations, while the model parameters in case of AGNs are given in Sect. 2.1. The implementation of MRI-quenching and the role of magnetic pressure is discussed separately in Sect. 2.2. The radiation pressure supported solution is analyzed in Sect. 2.4. The results of our numerical computations are presented in Sect. 3, where we display the vertical structure of disk and corona system, but we also show the radial limitation at which optically thick corona can exist. For our comparison with the observations, we used models generated in our scheme of random choice, as described in Sect. 3.4 and the measurements are described in Sect. 3.5. Our discussion and conclusions are given in Sects. 4 and 5, respectively.

2. Model set-up

We further investigated the model developed by GR20, adapted for the case of AGNs, where an accretion disk is located around a SMBH. The code solves the vertical structure of a stationary, optically thick accretion disk, with radiation transfer assuming gray medium and temperature determined by solving balance between total heating and cooling, including magnetic reconnection and radiative processes. The gas heating is powered by the magnetic field, according to the analytic formula given by BAR15, and the disk is magnetically supported over it's whole vertical extent. As an output, we can determine the vertical profile of magnetic heating of the accretion disk, as well as of the corona that forms at the top of the disk. For the purposes of this paper, we considered Compton scattering and free-free emission and absorption as radiative processes that balance the magnetic heating. Our approach is innovative because it connects the magnetically supported disk (BAR15) with transfer of radiation in optically thick and warm medium and in thermal equilibrium (Różańska et al. 2015). Such approach allows us to verify if the warm corona can be formed above the MSD and stay there in the optically thick regime, which will prove consistent with many observational cases.

The following set of five equations is solved:

$$z\frac{\mathrm{d}P_{\mathrm{mag}}}{\mathrm{d}z} + \left(2 + \frac{\alpha_{\mathrm{B}}\nu}{\eta}\right)P_{\mathrm{mag}} - \frac{\alpha_{\mathrm{B}}}{\eta}\left(P + P_{\mathrm{mag}}\right) = 0, \tag{1}$$

$$\mathcal{H} = 2(\eta + \alpha_B\nu)\Omega P_{\mathrm{mag}} - \alpha_B\Omega\left(P + P_{\mathrm{mag}}\right) = \Lambda(\rho, T, T_{\mathrm{rad}}), \tag{2}$$

$$\frac{\mathrm{d}F_{\mathrm{rad}}}{\mathrm{d}z} = \Lambda(\rho, T, T_{\mathrm{rad}}), \tag{3}$$

$$\frac{\mathrm{d}T_{\mathrm{rad}}}{\mathrm{d}z} + \frac{3\kappa\rho}{16\sigma T_{\mathrm{rad}}^3}F_{\mathrm{rad}} = 0, \tag{4}$$

$$\frac{\mathrm{d}P_{\mathrm{gas}}}{\mathrm{d}z} + \frac{dP_{\mathrm{mag}}}{\mathrm{d}z} + \rho\left[\Omega^2 z - \frac{\kappa F_{\mathrm{rad}}}{c}\right] = 0, \tag{5}$$

where the first two equations describe the magnetic field structure and magnetic heating as presented by BAR15. Magnetic pressure vertical gradient $\mathrm{d}P_{\mathrm{mag}}/\mathrm{d}z$ depends on magnetic parameters: total magnetic viscosity, α_{B}, magnetic buoyancy parameter, η, and reconnection efficiency parameter, ν (see: GR20, for definition), and the sum of gas and radiation pressure, $P = P_{\mathrm{gas}} + P_{\mathrm{rad}}$. At each point of the disk-corona vertical structure, the local magnetic heating, $\mathcal{H}$, is balanced by net radiative cooling rate $\Lambda(\rho, T, T_{\mathrm{rad}})$, where the latter is calculated from the frequency-integrated radiative transfer equation (see GR20 for the exact formulae).

Equations (3) and (4) describe how the radiation flux is locally generated and transported by the gas. The fifth equation is the momentum equation in stationary situation, namely, hydrostatic equilibrium, where ρ is gas the density, κ is the Rosseland mean opacity, Ω is the Keplerian angular velocity, and c is the light velocity. The gas and radiation pressure in our model can locally be described as $P_{\mathrm{gas}} = \frac{k}{\mu m_{\mathrm{H}}}\rho T$ and $P_{\mathrm{rad}} = \frac{4\sigma}{3c}T_{\mathrm{rad}}^4$ which is typical in case of gray atmosphere with k being the Boltzmann constant, σ as the Stefan-Boltzmann constant, and μ as the mean molecular weight.

To formulate our net radiative cooling function, we assume Compton electron scattering and free-free absorption and emission as radiative processes that occur in the medium. The radiative cooling function is calculated at each point of the MSD's vertical structure and here it takes the following form:

$$\Lambda\left(\rho, T, T_{\rm rad}\right) \equiv 4\sigma\rho\left[\kappa_{\rm ff}\left(T^4 - T_{\rm rad}^4\right) + \kappa_{\rm es}T_{\rm rad}^4\frac{4k\left(\gamma T - T_{\rm rad}\right)}{m_{\rm e}c^2}\right], \tag{6}$$

where $\gamma = 1 + 4kT/(m_{\rm e}c^2)$ accounts for relativistic limit in Compton cooling, $\kappa_{\rm es}$ is the electron scattering opacity, and $\kappa_{\rm ff}$ is the Planck-averaged free-free opacity. In principle, more processes can be included (Różańska et al. 1999), as long as the Planck-average opacities are known. However, in this paper, we clearly show that free-free absorption is efficient enough to onset of TI on the particular optical depth in magnetically supported accretion disk atmosphere. Usually, TI is connected with ionization and recombination processes, which we have not taken into account. We show here that ionization is not necessary to study TI, but it will be valuable in the future for testing how ionization and recombination processes influence the width of an thermally unstable region, which (as we show below) are connected with strength of the warm corona. We plan to do it in our future work, since it would require a substantial extension of our numerical code.

The set of equations and the associated boundary conditions are solved using a relaxation method, where the differential equations are discretized and then iteratively solved for convergence (Henyey et al. 1964, GR20). We adopted typical boundary conditions as appropriate for a cylindrical geometry of an accretion disk namely: the radiative flux at the mid-plane must be zero, but there is non-zero magnetic pressure at the equatorial plane. The value of magnetic parameter at the disk mid-plane $\beta_0 = P_{\rm gas}/P_{\rm mag}$ can be derived from three magnetic input parameters (described in Sect. 2.1 below). At the top of atmosphere of the MSD, we assume that the sum of the flux carried away by radiation and of the magnetic field is equal to the flux obtained by Keplerian disk theory. We also take into account standard boundary condition for radiative transfer, namely, a mean intensity of $J = 2H$, where the Eddington flux, H, connects to the radiative flux as $4\pi H = F_{\rm rad}$. For the full numerical procedure and boundary conditions of our code we refer the reader to GR20 paper Appendix A. The numerical program in FORTRAN, Python and Sympy that we developed for these purposes is available online[1].

2.1. Model parameters

The model is parameterized by six parameters. The first three are associated with an accretion disk, namely,: black hole mass, $M_{\rm BH}$, accretion rate, $\dot{m}$, and distance from the nucleus, R. Wherever it is not specified, we assume $M_{\rm BH} = 10^8\,M_\odot$, $\dot{m} = 0.1$ in the units of Eddington accretion rate, and $R = 6R_{\rm Schw}$, where $R_{\rm Schw} = 2GM/c^2$, with G being the gravitational constant, as our canonical model named: CM. Those parameters were chosen only for the representation of our results, nevertheless, we are able to compute the models for other typical parameters within the broad range.

The next three parameters, namely, magnetic viscosity, $\alpha_{\rm B}$, magnetic buoyancy parameter, η, and reconnection efficiency parameter, ν, define the local vertical structure of the MSD. We know how those parameters depend on each other, but there is no one good way of determining what values they should take. In our previous paper, GR20, we made an effort to compare magnetic structure with the one obtained from MHD simulations by Salvesen et al. (2016), and we adjusted those parameter relations to fit the simulation results. However, this is only one of the assumptions that can be made about the relation between $\alpha_{\rm B}$, η, and ν, and, in this paper, we chose to follow a slightly different approach. First, we require that the vertically averaged ratio of magnetic torque over magnetic pressure, marked as A, should be roughly constant in the disk, consistent with simulations reported by Jiang et al. (2014) and Salvesen et al. (2016). It can be proven that this is true if the value A is constant for any $\alpha_{\rm B}$, since

$$t_{r\phi}\Omega^{-1} = \alpha_{\rm B}P_{\rm tot} = \alpha_{\rm B}\frac{P_{\rm tot}}{P_{\rm mag}}P_{\rm mag} = 2AP_{\rm mag}, \tag{7}$$

where

$$A = \frac{1}{2}\alpha_{\rm B}\nu + \eta. \tag{8}$$

With this information, we can simplify our parametrization of the magnetic torque by making η and ν depend on $\alpha_{\rm B}$, since the simulations by Salvesen et al. (2016) show that there is some correlation between three parameters for different magnetic field strengths (see: Fig. 2 in GR20).

We first eliminate η by introducing the constant p, and assuming that it depends on $0 < \alpha_{\rm B} < 2A$ as follows:

$$\eta\left(\alpha_{\rm B}\right) = A\left(\frac{\alpha_{\rm B}}{2A}\right)^p. \tag{9}$$

Next, we transform the relation in Eq. (8) and substitute the expression in Eq. (9) to obtain ν

$$\nu\left(\alpha_{\rm B}\right) = 2\frac{A-\eta}{\alpha_{\rm B}} = \frac{1-\left(\frac{\alpha_{\rm B}}{2A}\right)^p}{\frac{\alpha_{\rm B}}{2A}}. \tag{10}$$

The above relations are the basis of our assumptions for this study and were formulated in the process of understanding what really influences the magnetic heating vertical structure. For instance, we have tested that our results are not sensitive to the selection of A and p; therefor, we kept those values constants for the results of this paper, namely, $A = 0.3$ and $p = 0.3$.

Therefore, keeping constant A and p, the two extremes of our magnetic viscosity parameter range are realized where $\alpha_{\rm B} \approx 2A$, which is a strongly magnetized disk, and where $\alpha_{\rm B} \approx 0$ for weakly magnetized disk (Eq. (7)). Furthermore, magnetic buoyancy parameter – η and reconnection efficiency parameter, ν, can be automatically provided by Eqs. (9) and (10) for an assumed value of $\alpha_{\rm B}$. Such convention may seem a bit complicated, but it offers an intuitive clue about the values of the efficiency of other processes, such as magnetic buoyancy strength and reconnection efficiency. In the case of a strongly magnetized disk, the above equations lead to $\eta \approx A$ and $\nu \approx 0$, which means that such a disk has both very few dynamo polarity reversals and low recconection efficiency. A weakly magnetized disk yields $\eta \approx 0$ and $\nu \gg 1$, realized when frequent polarity reversals cause the majority of the energy to be dissipated by magnetic reconnection.

2.2. Implementation of MRI-quenching

The vertical support in the disk is caused by the toroidal field produced by MRI dynamo in the presence of vertical net energy

[1] https://github.com/gronki/diskvert

field, and the efficiency of this process is described by the magnetic viscosity parameter $\alpha_{\rm B}$. However, when the magnetic field becomes too strong compared to kinetic force of the gas, the MRI is inefficient, and the dynamo is quenched (BAR15). That causes the decrease in toroidal field production in some areas of the vertical structure and reduces the magnetic support. The approximate condition for this efficiency limit is given by Pessah & Psaltis (2005) and can be written as a limit to magnetic pressure:

$$P_{\rm mag} \leq P_{\rm mag,max} = \sqrt{\frac{5}{3}\rho P_{\rm gas}}\ \Omega R. \tag{11}$$

Since the limit on the magnetic pressure depends on density and gas pressure, it becomes particularly significant in AGN disks, where the contribution of gas pressure compared to radiation pressure is lower than in stellar-mass black hole accretion disks. That is to say that the domination of radiation pressure is seen for broader ranges of accretion rates and extends to larger distances from black holes (Kato et al. 2008).

We can implement this condition by limiting the $\alpha_{\rm B}$ parameter:

$$\alpha'_{\rm B} = \alpha_{\rm B}\ T(P_{\rm mag,max}/P_{\rm mag}) = \alpha_{\rm B}\, T(x), \tag{12}$$

where $T(x) = x^4/(1+x^4)$ is a smooth threshold-like function with values close to 0 for $x < 1$ and close to 1 for $x \gg 1$. Using this method, we were able to obtain a gradual transition between the zones where MRI dynamo operates and zones where it is quenched. We checked that the final results of our model are not sensitive on the choice of the particular shape of threshold function.

We note that our model fully depends on parametrization and we consider that MRI can be operated by a strong magnetic field. In the current parametrization, we cannot turn off the magnetic field, since the transition would lead to a viscous standard viscous α-disk (Shakura & Sunyaev 1973). Also, we do not consider how the MRI would be influenced by the convective instability, since we found it would be complicated at this point in the model demonstration. The magnetic field was never measured from accretion disk around SMBH, and, therefore, we have no constraints on how it should be. Only the simulations can provide some clues and we have checked that our resulted vertical magnetic field distribution agrees with the simulations (see GR20). Even if the BR15 model is assumed, the energy released in magnetically heated disk has the comparable value to the energy generated by viscosity and presents a good way of replicating the energy production by MRI and the transfer of this energy into gas. Below, we show how this magnetic pressure affects radiative processes in accretion disks around SMBH.

2.3. Thermal instability

To determine the temperature of the gas, we need to solve the thermal balance equation. On one side, we have the heating terms and on the other side, there is the radiative cooling function. This equation normally has one solution and the cooling rate should have a positive derivative with respect to temperature. In some circumstances this problem has more than one solution, that is, there are typically three, with one of them being unstable. For that unstable solution, assuming that the heating is roughly independent on gas parameters, the condition for instability is expressed as:

$$\frac{d\ln\Lambda}{d\ln T} = \frac{\partial\ln\Lambda}{\partial\ln T} - a\frac{\partial\ln\Lambda}{\partial\ln\rho} \leq 0, \tag{13}$$

where a is a numerical constant, depending on the constraining regime. Some typical values are: $a = 1$ for $\delta P_{\rm gas} = 0$, $a = 0$ for $\delta\rho = 0$ and $a = \frac{\beta}{\beta+2}$ for $\delta P_{\rm gas} + \delta P_{\rm mag} = 0$, where $\beta = P_{\rm gas}/P_{\rm mag}$ (Field 1965).

Usually, $\delta P_{\rm gas} = 0$ is the assumed thermodynamic constraint for the instability and if only Compton scattering and free-free cooling are taken into account, this limits the density of the gas, according to the formula given in GR20:

$$n/n_0 < (T/T_{\rm rad})^{-1/2}, \tag{14}$$

where

$$n_0 = 4\times10^{16}\left(\frac{T_{\rm rad}}{10^6\ {\rm K}}\right)^{9/2}. \tag{15}$$

If we assume that around the base of the corona, we have $T \approx T_{\rm rad}$, this condition becomes $n < n_0$, and we can estimate the approximate limit for optical depth of the corona.

The estimate for density given in Eq. (15) assumes that gas pressure is constant. In magnetically dominated corona, however, the density in hydrostatic equilibrium is mostly imposed by magnetic field gradient. For that case, we might assume that the constant-density model is more relevant than the constant-pressure model. Thankfully, in an isochoric regime, the condition for instability is never satisfied and when magnetic pressure is added, even small values are enough to completely eliminate the instability.

2.4. Radiation-pressure supported solutions

For SMBHs (as opposed to black holes of stellar mass), the radiation pressure displays a large contribution in comparison to the gas pressure in supporting the disk structure. This is important because radiation pressure-dominated disks are considered unstable for the certain range of parameters (Lightman & Eardley 1974; Shibazaki & Hōshi 1975; Shakura & Sunyaev 1976; Begelman 2006; Janiuk & Czerny 2011). When solving the vertical structure of a geometrically thin accretion disk, this radiation pressure instability manifests itself as a "blown up" solution, where the density is roughly constant over a large height of the disk structure; however, it may be the case that the density is larger around the photosphere than in the disk mid-plane. In a non-magnetic disk, this would satisfy the criterion for the convective instability and the density gradient would be restored (Różańska et al. 1999).

In our models, we did not include convection, as it might be restricted by the magnetic field, which shapes the disk structure. Instead, we compute of the pressure gradient, $\propto\frac{d\ln\rho}{d\ln z}$, and check its minimal value. The negative value means that the density inversion occurs and the model might not be stable. We mark these models clearly while presenting results of our computations. Nevertheless, since we were not aiming to solve time-dependent radial equations (Szuszkiewicz & Miller 1997), we were not able to compare changes caused by TI to those generated by radiation pressure instability front (i.e., when we expect that the earlier moves in the vertical direction and the later in the radial one. We plan to address this analysis in a future work.

3. Results

For an opimal visualization of the physical conditions occurring on the border of disk and warm corona, we are plotting several quantities describing the processes that take place in magnetically supported and radiatively cooled accretion disks. From the

X-ray spectral fitting, we measured an averaged temperature of the warm corona cooled by Comptonization as:

$$T_{\rm avg} = \tau^{-1} \int_0^{\tau_{\rm cor}} T d\tau \,. \tag{16}$$

We note that, for the purposes of this paper, we adopted τ to be the Thomson optical depth measured from the surface toward the mid-plane. This is due to the fact that electron scattering optical depth is commonly measured during data analysis, when soft X-ray excess is fitted by a Comptonization model. We defined the base of the corona $\tau_{\rm cor}$ as τ for which the temperature reaches minimum. In some figures displaying vertical structure, we also marked the position of photosphere, where total optical depth is: $\tau + \tau^{\rm P}_{\rm ff} = 1$ or the thermalization zone, where the effective optical depth is $\tau^* = \sqrt{\tau^{\rm P}_{\rm ff}(\tau + \tau^{\rm P}_{\rm ff})} = 1$, where $\tau^{\rm P}_{\rm ff}$ is the mean Planck opacity for free-free absorption.

To trace TI, the important quantity is the well-known ionization parameter (Krolik et al. 1981; Adhikari et al. 2015), defined as:

$$\Xi = \frac{P_{\rm rad}}{P_{\rm gas}}. \tag{17}$$

Although we did not compute the ionization states of the matter, the above parameter indicates the place in the disk structure where the TI physically starts (Różańska & Czerny 1996; Różańska 1999). The TI appears exactly when the gradient of the cooling function, that is, the so-called stability parameter computed under constant gas pressure, becomes negative:

$$\mathcal{L}_{\rm rad} \equiv \left.\frac{d\ln\Lambda}{d\ln T}\right|_{\delta P_{\rm gas}=0} < 0 \,, \tag{18}$$

which we also visualize in our figures below. Our computations allowed us to indicate the Thompson optical depth, $\tau_{\rm min}$, for which the above stability parameter is minimal. In addition, we calculated the value of net cooling rate gradient over temperature under constant gas plus the magnetic pressure to show how magnetic pressure affects stability of the disk heated by MRI.

To estimate the importance of the magnetic pressure versus gas pressure at each depth of the disk, the commonly used magnetic pressure parameter is defined as:

$$\beta = \frac{P_{\rm gas}}{P_{\rm mag}}. \tag{19}$$

For the purposes of this paper, analogously to the ionization parameter, we define the magnetic ionization parameter as:

$$\Xi_{\rm m} = \frac{P_{\rm rad}}{P_{\rm mag} + P_{\rm gas}}, \tag{20}$$

which helps us to show the domination of radiation pressure across the disk vertical structure. Furthermore, we demonstrated in GR20 that the density of the corona depends mostly on the magnetic field gradient:

$$q = -\frac{d\ln P_{\rm mag}}{d\ln z}. \tag{21}$$

We note that all parameters change with disk-corona vertical structure and we marked them with a "0", when defined at the mid-plane. We also defined the magnetic dissipation rate as follows:

$$q_{\rm h} = \left(\frac{m_{\rm H}}{\rho}\right)^2 \mathcal{H}, \tag{22}$$

in erg cm^3 s^{-1}, so it can be compared to other heating and cooling rates from the literature that are given the same units. As an outcome of our computations, we can also deliver information about the total surface density Σ in g cm^{-2} of the disk-corona system, which is the density integrated over the total height.

Finally, the properties of the Compton cooled surface zone were observationally tested with the use of Compton parameter as follows:

$$y_{\rm avg} = \int_0^{\tau_{\rm cor}} \frac{4k(T - T_{\rm rad})}{m_{\rm e}c^2} (1 + 2\tau)\, d\tau \,, \tag{23}$$

and in the section below we determine such a parameter either up to thermalization layer of $\tau^\star$ or up to the corona base of $\tau_{\rm cor}$.

In analogy to Haardt & Maraschi (1991), we denote the fraction of the energy released in the corona versus total thermal energy $F_{\rm rad}$ as:

$$f = \frac{F^{\rm cor}_{\rm rad}}{F_{\rm rad}} = 1 - \frac{F^{\rm disk}_{\rm rad}}{F_{\rm rad}}, \tag{24}$$

where $f = 0$ corresponds to the passive corona, while $f = 1$ corresponds to passive disk. In the case of a magnetically supported disk, f depends only on the magnetic parameters, and both fluxes, $F^{\rm cor}_{\rm rad}$ and $F^{\rm disk}_{\rm rad}$, are not assumed, but (instead) numerically calculated in our model. The division between disk and corona is taken at the layer when coronal temperature reaches minimum, that is, at $\tau_{\rm cor}$. All quantities listed in this section were self-consistently derived as an outcome of our model. We present them to check the model correctness and compare them with the observations.

3.1. Vertical structure

In order to elucidate the formation scenario of a warm corona, we show the vertical structure of our CM model in Fig. 1. In all panels, the horizontal axis is the height above the mid-plane of the disk in units of cm. Each figure panel represents the structure of parameter given in the panel's title. Three models for various magnetic parameters are given by different line colors described in the box above figure caption. The model called M1 stands for a highly magnetic disk with value of $\alpha_{\rm B} = 0.5$, while the model M3 stands for low magnetic disk – with $\alpha_{\rm B} = 0.02$.

The gas temperature of the disk (panel a solid lines), in all three models, follows the trend with warmer center and cooler photosphere which eventually undergoes an inversion and forms a corona being much hotter than the center of the disk. The inversion occurs roughly at $z = 10^{13}$ cm. The temperature of the corona rises sharply but gradually with height as z^2, even though the heating rate per volume, plotted by solid lines at the panel f of Fig. 1, decreases as z^{-q}. Closer to the equator, the temperature rise typically present in case of standards viscous α-disk (Shakura & Sunyaev 1973) saturates due to magnetic heating being distributed much further away from the equatorial plane, resulting in lower radiative flux and less steep temperature gradient.

The radiation pressure is large in the core, between two and three orders of magnitude higher than the gas pressure, and it can be of comparable magnitude to the magnetic plus gas pressure (panel b). While it fully dominates at the atmosphere where the warm corona is formed and where both ionization parameters, Ξ and $\Xi_{\rm m}$, increase by two orders of magnitude with the height towards the surface. In addition, the inversion of both parameters is present, regardless of the value of magnetic pressure. Such a

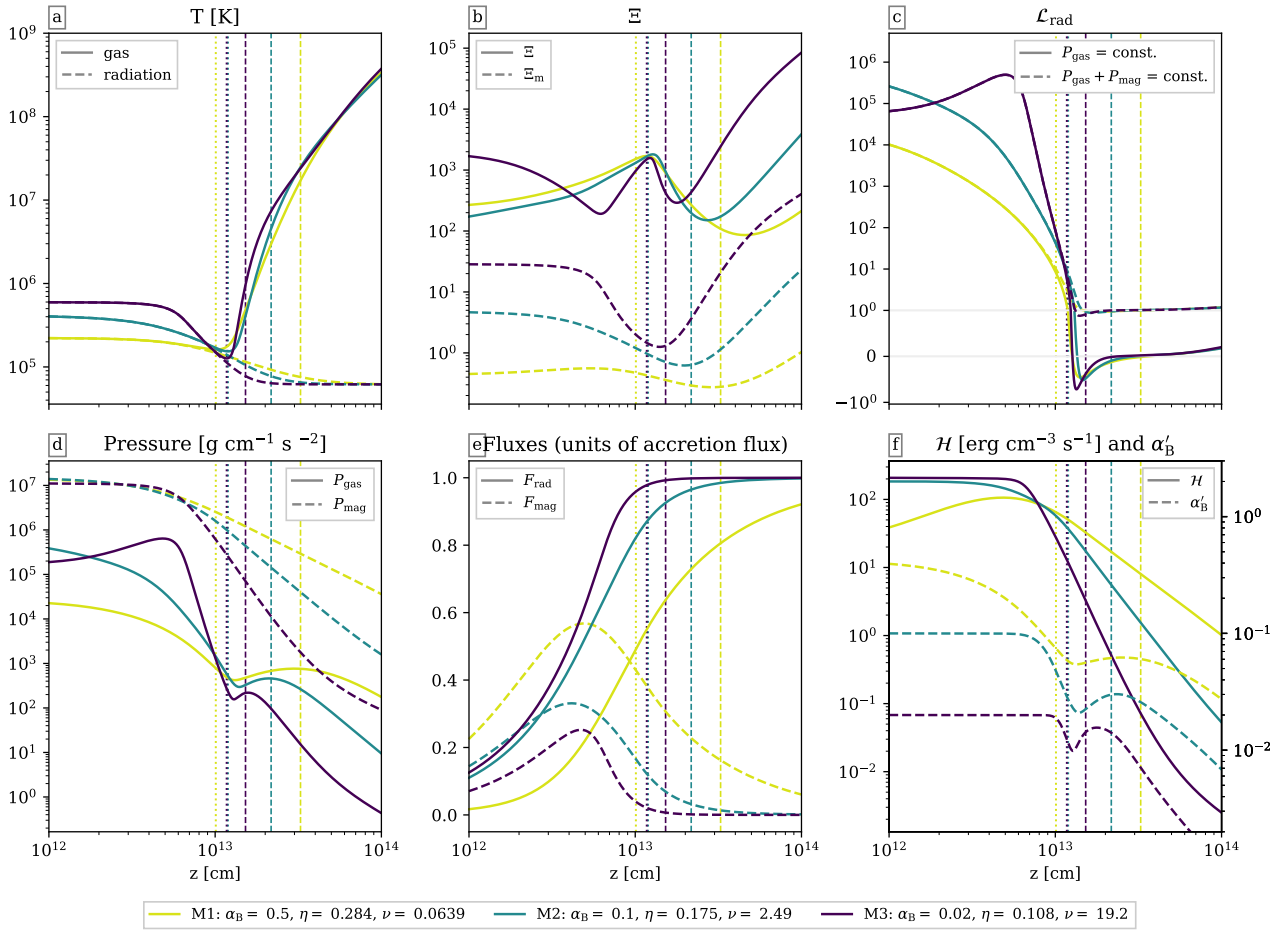

Fig. 1. Vertical structure of an accretion disk for our CM model versus z in cm measured from disk mid-plane ($z = 0$) up to the surface (right side of the figure panels), and for three different sets of magnetic parameters ranging from the strongest (M1, as a yellow line) to the weakest (M3, as a black line) magnetic field, and listed in the box below the figure. The local temperature, ionization parameter (Eqs. (17) and (20)), and stability parameter (Eq. (18)) are plotted in the top row, while pressures, fluxes relative to the total dissipated flux, and heating rate are plotted in the bottom row, respectively. In addition, the value of $\alpha'_{\rm B}$ according to Eq. (12) is shown in the last panel of second row, by dashed lines. The positions of corona base $\tau_{\rm cor}$ are marked by vertical dotted lines, and the positions of photosphere are shown as dashed lines for each model, respectively.

course of Ξ and $\Xi_{\rm m}$ is connected with the structure of stability parameter, presented in panel c of Fig. 1, which is negative even for the most stringent condition of constant gas pressure. Although it is not large in a geometric sense, this area actually constitutes a large part of the optically thick corona.

The gas pressure (panel d) is roughly constant in the center (due to radiation pressure) and decreases as $z^{-(q+2)}$, with exception of the model M3 which has the weakest magnetic field. In that model, the region of lesser gas pressure forms in the core of the disk, due to radiation pressure acting as a primary support for the disk structure; this is because the convection that would remove this inversion is absent in our model. In the region of the photosphere the gas pressure levels out, just to enter a sharp decrease in the magnetic pressure-dominated corona. It is worth noting that the magnetic pressure is dominating significantly over gas pressure in our model at all points of the vertical structure.

The radiative and magnetic fluxes are released at a comparable rate inside the disk (panel e). We note that the fluxes are given in relation to the total flux released by accretion. In the magnetically dominated corona, the magnetic flux is quickly depleted in sub-inversion area and it is almost zero when it enters the corona, except in the case of strongly magnetized models.

The magnetic heating in the corona is decreasing sharply with height (panel f), except for the strongest magnetic field case M1, where the peak heating occurs in the transition region and then $\mathcal{H}$ gently decreases. In this model, the MRI process begins to quench at around $z = 10^{12}$cm, which is ten times lower than other models and can be seen as a decrease in $\alpha'_{\rm B}$, (given by the dashed lines at the same panel) slightly above the equatorial plane. By $z = 3 \times 10^{13}$cm, the MRI becomes almost completely inactive, due to a rise in the gas pressure in the corona. To produce such a corona, the value of toroidal magnetic field at the equatorial plane is $\log B_0 = 4.25$, 4.28, and 4.22 G, for considered models: M1, M2, and M3, respectively, and it is three orders of magnitude lower than in case of GBHB (GR20).

To follow the vertical extension of the TI zone, we present the temperature structure versus ionization parameter (defined by Eq. (17)) in the left panel of Fig. 2, for our three models M1, M2, and M3 of different magnetizations. In case of each model, we mark the corona base, $\tau_{\rm cor}$, by a triangle. The part of stability curve with negative slope is clearly present in each of the model,

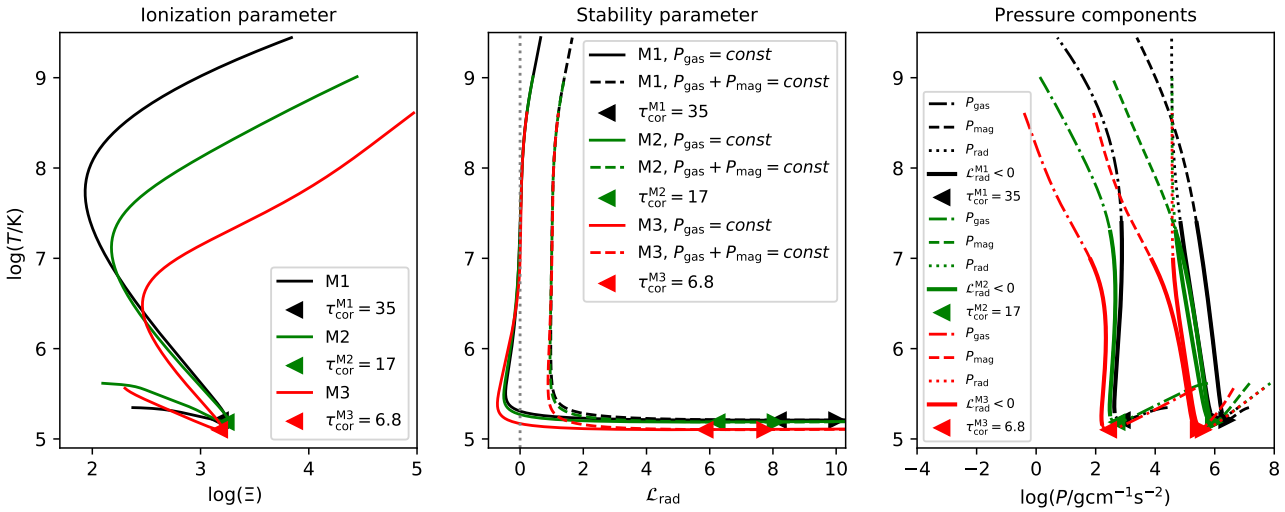

Fig. 2. Temperature structure of an accretion disk for our CM model versus ionization parameter (left panel), stability parameter (middle panel) and all three pressure components (right panel). Gas pressure structure is given by dashed-dotted line, magnetic pressure by dashed line, and radiation pressure by dotted line. Three models of different magnetization are defined as in Fig. 1, and given by colors: M1 – black, M2 – green, and M2 – red. At each panel, the position of temperature minimum is clearly indicated by a triangle of the same color. Gray dotted line in the middle panel marks the limit of negative value of stability parameter. Thick solid lines in the right panel cover values of pressure and temperature for which classical stability parameter (under constant gas pressure) is negative.

which clearly shows that magnetic heating does not remove TI in regions of high temperatures, on the order of 1 keV, and high densities, on the order of 10^{12} cm^{-3}, cooled by radiative processes. Interestingly, such a TI is created only for Compton and free-free absorption and emission. For descending temperatures, below the corona base, there is another turning point. Below this point, the gas stabilizes due to magnetic heating. This can be first deduced from the fact that going toward the equatorial plane, the disk temperature increases, which is clearly presented in panel a of Fig. 1.

In order to show how magnetic pressure affects the warm heated layer above cold disk, we plot the stability parameter in Fig. 2 (middle panel), for all three models in two versions. The solid line presents a classical cooling rate gradient under constant gas pressure, while the dashed line shows the same gradient under constant gas plus magnetic pressure. It is clear that a negative value of the stability parameter occurs only in the case of classical assumption of constant gas pressure. Magnetic pressure directly makes cooling rate gradient to be always positive, acting as a freezer for eventual evolution of gas due to TI. For all three models, the base of the corona occurs below the TI zones under the classical constant gas pressure condition. In the forthcoming paper, we plan to calculate proper timescales for TI evolution and for the existence of magnetically heated corona.

In magnetically supported disk, the radiation pressure dominates in the disk interior, while it becomes comparable to magnetic pressure in thermally unstable zones. This is clearly demonstrated on the right panel of Fig. 2, where solid lines cover pressure plots for regions where the classical stability parameter is negative. Gas pressure, which reflects the gas structure, is always at least four orders of magnitude lower than magnetic pressure. It is worth noting that going from the surface towards corona base, the gas temperature decreases while all three pressure components tend to increase. After passing τ_{cor}, the temperature starts to increase with depth and with the increase of all three pressure components. Small negative slopes in the vertical structure of gas pressure do not affect the overall stability of the disk, since the gas distribution is mostly maintained by the magnetic pressure.

3.2. Warm corona across the parameter space

The dependence of the coronal parameters derived from our model on the accretion rate and on the magnetic field strength for the black hole mass of $M_{BH} = 10^8\,M_\odot$ and at a radius of $R = 6\,R_{Schw}$ is shown in Fig. 3. We adopt that the corona extends from the zone where the gas temperature reaches minimum, as visible at panel a of Fig. 1, up to the top of an atmosphere. The optical depth, τ_{cor}, is greater for higher accretion rate and stronger magnetic viscosity parameter. On the other hand, the temperature, T_{avg}, averaged over τ from the surface down to τ_{cor}, seems to be mainly dependent on the magnetic field strength.

As may be gleaned from the ratios of radiation, the gas and magnetic pressures (displayed in panel b of Fig. 3, plotting Ξ as color maps and β as contours at the corona base, the disk is dominated by the radiation pressure for the whole parameter space. In addition, magnetic pressure overwhelms the gas pressure and this is the main reason that we obtain an optically thick soft corona layer as predicted by Różańska et al. (2015). The magnetic pressure is limited by the condition in Eq. (11), which occurs as a sharp transition in all global parameters at around $\dot{m} > 0.01$. For such a high accretion rate, the contribution of radiation pressure is very high and if the magnetic support is not strong enough, the solution becomes unstable (see Sect. 2.4) as marked as a black overlay in all panels. This effectively restricts the solutions for high accretion rates only to models where the magnetic field is sufficiently strong ($\alpha_B > 0.05$).

The gas density at the base of corona (panel c of Fig. 3) is the highest for both high accretion rate and high magnetic parameter. Decreasing the magnetic field also has a global stability effect on the disk. For a thin accretion disk, the quantity $d\Sigma/d\dot{m}$ should be positive, otherwise we encounter a problem with well-known stability of standard viscous α-disk (Shakura & Sunyaev 1973). For a weak magnetic field, this value is negative even for

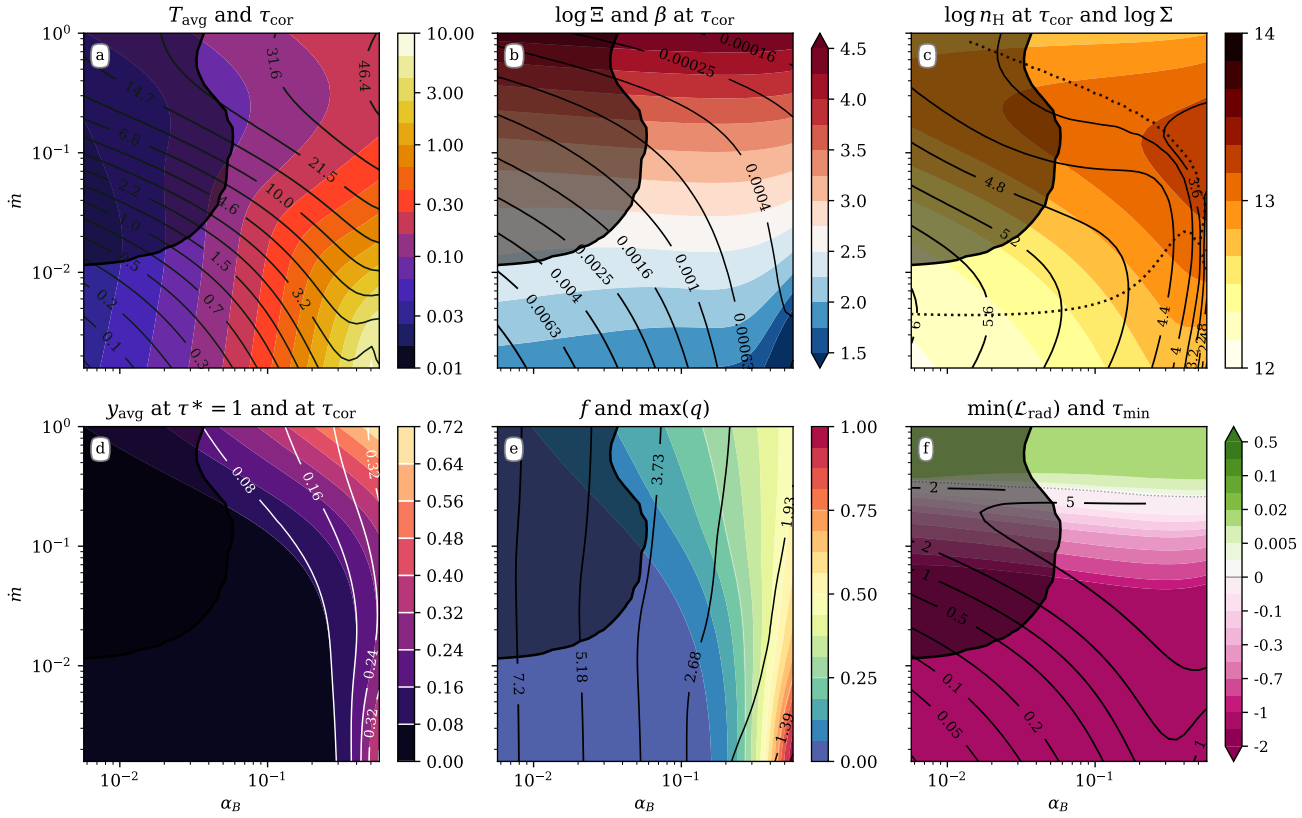

Fig. 3. Properties of the warm corona on the accretion rate-magnetic viscosity parameter plane. All models have been calculated for $M_{BH} = 10^8\,M_\odot$ and $R = 6\,R_{Schw}$. Upper panels show: a) average temperature, T_{avg}, of the corona in keV (colors) and optical depth of the base of the warm corona τ_{cor} (contours); b) Ξ (colors) and magnetic pressure parameter β (contours) both at τ_{cor}; and c) number density n_H in cm^{-3} (colors) at τ_{cor} and total column density Σ in g cm^{-2} (contours). Dotted contour here shows where $d\Sigma/d\dot{m} = 0$. Bottom panels display: d) y_{avg} parameter of the warm corona at the thermalization zone, namely, $\tau^* = 1$ (colors), and at the base of the corona, τ_{cor} (contours); e) fraction of radiative energy produced by the corona f (colors) and the maximum value of magnetic field gradient q (contours); and f) the minimum value of $\mathcal{L}_{rad}$ throughout the disk height (colors) and Thomson optical depth, τ_{min}, for which it occurs (contours), green areas are stable disks, whereas magenta areas indicate thermal instability in the corona, the gray dotted line corresponds to $\mathcal{L}_{rad} = 0$. In all panels, the dark contour indicates the parameter sub-space affected by the density inversion.

$\dot{m} = 0.003$, as indicated by the region enclosed by the dotted contour in panel c of Fig. 3. If we introduce a stronger magnetic field, however, the band of accretion rate where this criterion is met, is narrowed down considerably.

Investigating the y_{avg} parameter (panel d of Fig. 3) and comparing it to corona-to-total flux ratio, f (panel e of Fig. 3), we find similar behavior, where the largest values of both parameters are obtained for $\alpha_B > 0.3$. Nevertheless, the Compton parameter has his largest values for high accretion rate, while the amount of energy generated in the corona is largest for low values of accretion rate.

The magnetic field gradient parameter, q, is mostly imposed by the model parameters, but it is worth seeing that its value only drops below 2 for the most magnetized models (panel e). On the other hand, the value of stability parameter, $\mathcal{L}_{rad}$, presented in panel f is almost exclusively dependent on the accretion rate, while the optical depth τ_{min}, can reach values up to 5.

3.3. Radial structure of the warm corona

Figure 4 shows the radial dependence of global parameters of the warm corona for our canonical BH mass $M_{BH} = 10^8\,M_\odot$ and for three strengths of the magnetic field, namely, M1, M2, and M3 models, with the same magnetic parameters α_B, η, ν as in Fig. 1. Upper panels show maps of T_{avg} given by Eq. (16), and contours of τ_{cor}. Dotted line contour separates thermally stable regions for high accretion rates and thermally unstable for low accretion rates by the condition $\mathcal{L}_{rad} = 0$. Bottom panels present maps of the density number of the warm corona and contours indicate the total column density Σ computed from the top down to the mid-plane. In case of M3 model, with the lowest magnetization, we clearly indicate sub-space affected by classical radiation pressure instability marked by dark contours.

The overall radial dependence of the warm corona parameters follows the trend that corona is hotter and more optically thick for strongly magnetized disk (M1 model on left panels). Higher accretion rate makes the corona cooler (i.e., lower T_{avg}) but optically thicker. In the case of high accretion rate, such a warm and optically thick corona is rather more dense then in case of hotter corona appeared for low accretion rate. However, for the model with a strong field, the quantity $d\Sigma/d\dot{m}$, which is associated with stability of viscous accretion disk, is positive in all but a narrow stripe in the parameter space marked by dotted lines at bottom panels of Fig. 4. On the other hand, for a weak-field M3 model, there is a maximum column density for around $\dot{m} = 0.03$, above which Σ decreases.

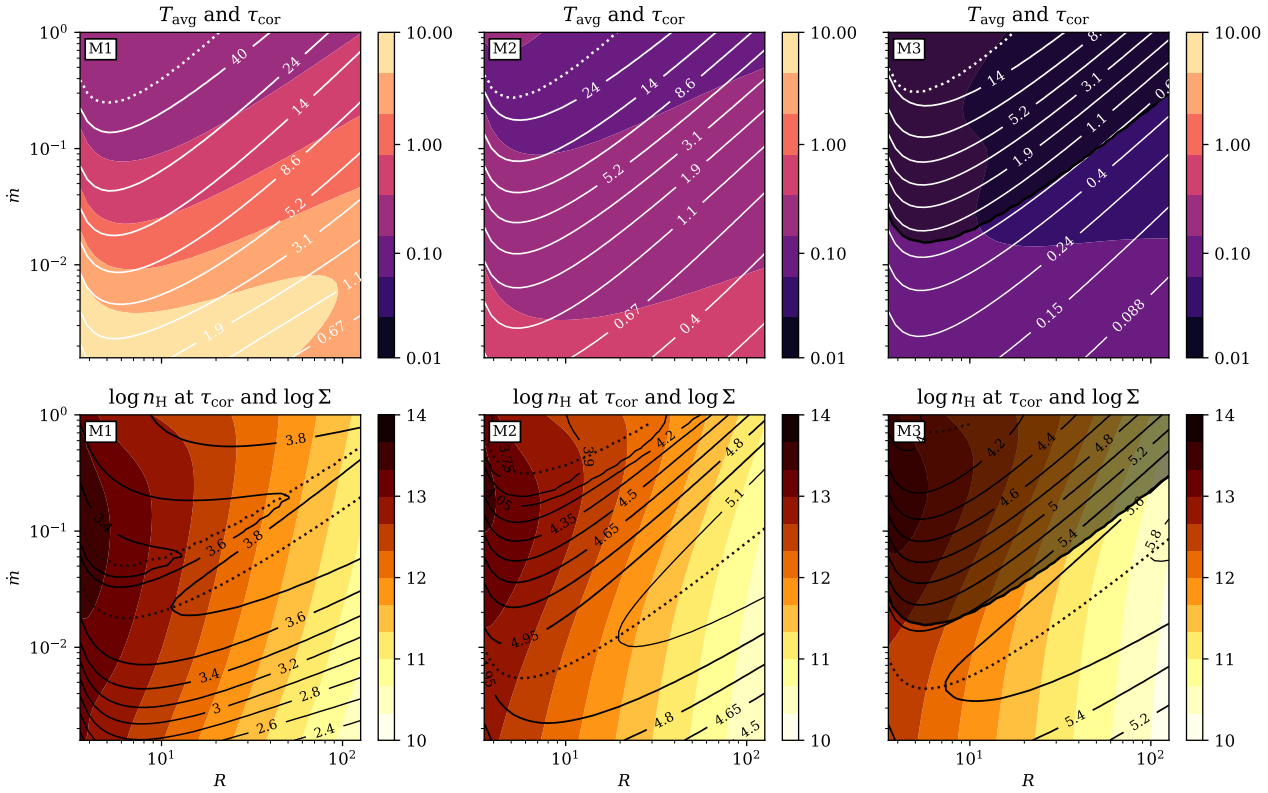

Fig. 4. Properties of the warm corona on accretion rate-radius plane given in units of R_{Schw}. All models have been calculated for $M_{BH} = 10^8\,M_\odot$, and magnetic parameters are corresponding M1 (left), M2 (middle), and M3 (right) panel columns with values given under Fig. 1. Upper panels display average temperature T_{avg} of the corona in keV (colors) and optical depth of the base of the warm corona τ_{cor} (contours). Dotted contours at upper panels indicate where $\mathcal{L}_{rad} = 0$ under constant gas pressure. Bottom panels show number density n_H in cm^{-3} (colors) at τ_{cor} and total column density Σ in g cm^{-2} (contours). Dotted contours at bottom panels show where $d\Sigma/d\dot{m} = 0$. Dark contours in case of M3 model, indicate the parameter sub-space affected by the density inversion.

In order to specify how TI, caused by gas cooling processes, affects the existence of the warm corona, we plotted the vertical extent of thermally unstable zones versus distance from the black hole in Fig. 5 for three different magnetic parameters and three accretion rates. The extent of the TI zone is presented as a pink-filled area. The base of the corona is clearly marked by thick black solid line. The optical depth of the corona base is larger for higher accretion rate. As shown in the previous section, TI – indicated by negative values of the stability parameter is present for the broad range of parameters under the assumption of constant gas pressure – but it disappears when it is computed over a constant sum of gas and magnetic pressure.

Furthermore, it is produced by radiative processes, such as Comptonization and free-free emission and absorption, being the only cooling processes in the models considered in this paper. Ionization and recombination may influence the extend of TI (Różańska & Czerny 1996), but the final result cannot be analytically predicted. Further computations are needed to show whether ionization or recombination decreases or increases the thermally unstable zone. It's only for high values of the accretion rate (i.e., higher than 0.2) and in the inner regions of an accretion disk within $20R_{Schw}$, the existence of thermally stable warm coronas with classical condition of constant gas pressure is possible. We claim here that in case of the MSD, the condition of thermal stability under constant total namely, gas plus magnetic pressure should be used in order to estimate if the TI zone is frozen into a magnetic field. In a forthcoming paper, we plan to calculate relevant timescales for this kind of radiative cooling in the magnetically supported plasma.

3.4. Random models sample

Our numerical code (GR20) allows us to calculate a huge number of models in a finite time. In order to put constraints on basic observational parameters resulting from our model: temperature of the corona and its optical depth, we have selected results from random distribution of six input parameters for our calculations described in Sect. 2.1, to account for their uncertainty. We use a notation whereby $U(a, b)$ is a random variable with a uniform distribution between a and b and $N(\mu, \sigma)$ is a normal distribution with expected value μ and spread σ. We use a fixed radius $R = 6R_{Schw}$, while black hole mass, M_{BH}, and accretion rate, $\dot{M}$, (in g s^{-1}) are selected in the way to mimic the distribution of the same quantities in the sample of 51 AGN for which the warm corona was observed (Jin et al. 2012, see section below). The random walk overdoes through the following distribution:

$$\log(M_{BH}) = N(7.83, 0.63), \tag{25}$$

$$\log(\dot{M}) = 0.27\,(\log(M_{BH}) - 8) + N(25.83, 0.52), \tag{26}$$

where the expected and spread values were estimated from the observed sample. After running the code and solving the structure, we reject the models that satisfy the radiation pressure criteria described in Sect. 2.4.

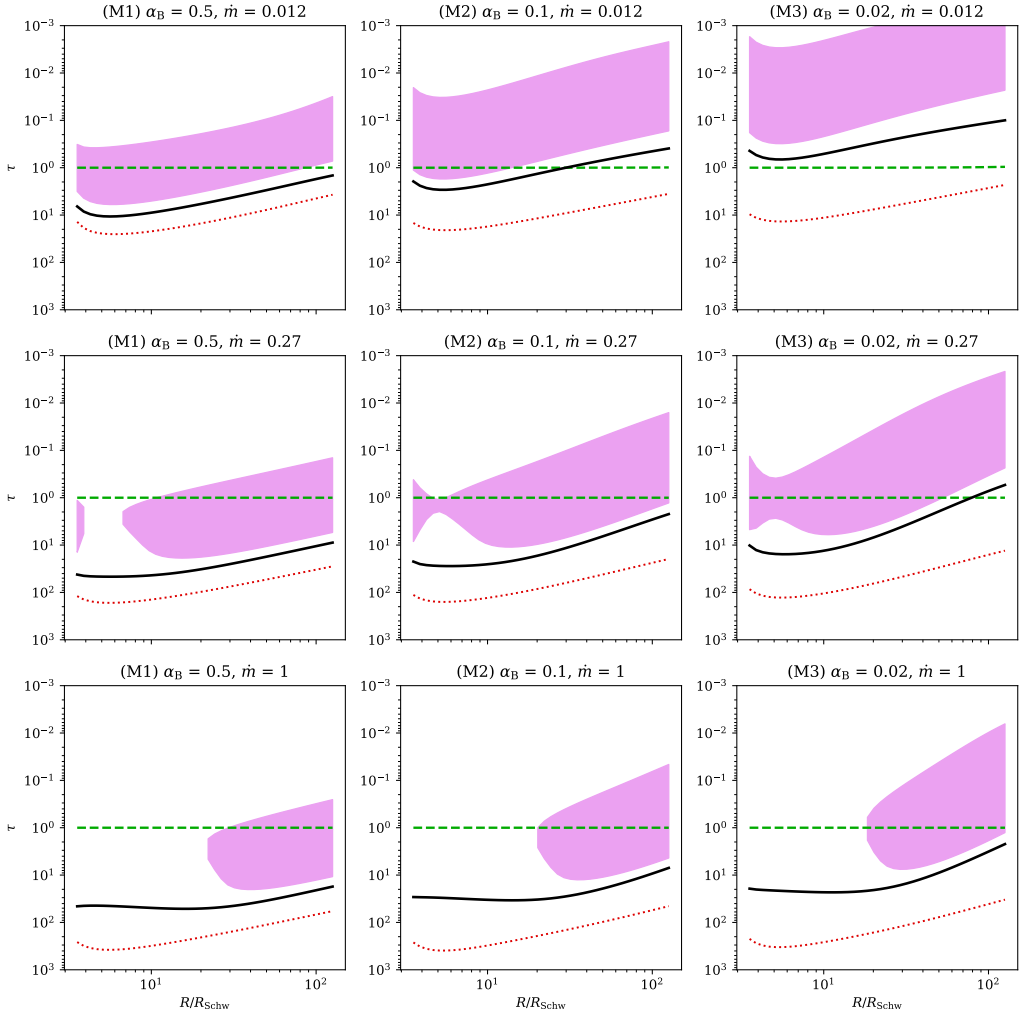

Fig. 5. Thomson scattering optical depth of TI zones, plotted against the radial distance from the BH of the mass $M_{BH} = 10^8\,M_\odot$, and shown for three values of magnetic parameters M1, M2, and M3 (from left to right columns), and an accretion rate of $\dot{m} = 0.012$, 0.27, and 0.1 (from upper to bottom rows). The photosphere is marked using the green dashed line, temperature minimum with a thick black solid line, thermalization depth ($\tau* = 1$) with a red dotted line. The extent of the thermal instability is presented as a pink-filled area.

We generated a set of models based on random distribution of the global disk parameters described by Eqs. (25) and (26). The vertical structures of all models in the sample are plotted collectively in Fig. 6, with the full sample (upper panels) as well as sample clipped according to the criterion of the density inversion (lower panels) described in Sect. 2.4. The temperature inversion occurs between $\tau = 0.01$ and $\tau = 30$ for all models, with both the magnetic field and accretion rate having a positive effect on the corona depth, as shown in left panels of both rows of Fig. 6. The density follows a rather predictable relation $n_H \propto z^{-q-2} \propto (N_H)^{\frac{q+2}{q+1}}$ and the heating rate changes as $q_h \propto z^{q+4} \propto (N_H)^{-\frac{q+4}{q+1}}$, with small fluctuations due to the opacity.

When we remove the models that do not satisfy our criterion for the density gradient (i.e., moving from the upper to lower panels of Fig. 6), the picture does not change much, but it becomes more complex when we omit the parts of the structure which is thermally unstable (when $d \ln \Lambda / d \ln T < 0$). For the set of models we analyzed, the TI is confined to the area where $10^{-24} \le q_h \le 10^{-22}$ and this does not seem to strongly vary with any of the model parameters we consider. Thus, we can summarize these results according to the following: independently of the model parameters, those associated with the accretion disk or with the magnetic field, the classical TI (under constant gas pressure) is present for magnetically supported disk with radiative processes as Comptonization and free-free emission.

3.5. Observational predictions

As the main outcome of our computations, we obtain values for the warm coronal temperatures and optical depths, which are directly comparable to the measurements reported in the literature. The data analysis concerning warm corona require high resolution, sensitive telescopes to collect enough photons in the soft X-ray energy range around 1 keV. The overall modeling is time consuming and usually one paper is devoted to one source. We have looked at the literature and we chose those sources for which both parameters: warm coronal temperature and its optical depth were measured. The warm corona measurement for the sample of objects has only been presented by Jin et al. (2012), who collected 51 sources. We take all those points into account while comparing to data. In addition we selected measured warm corona

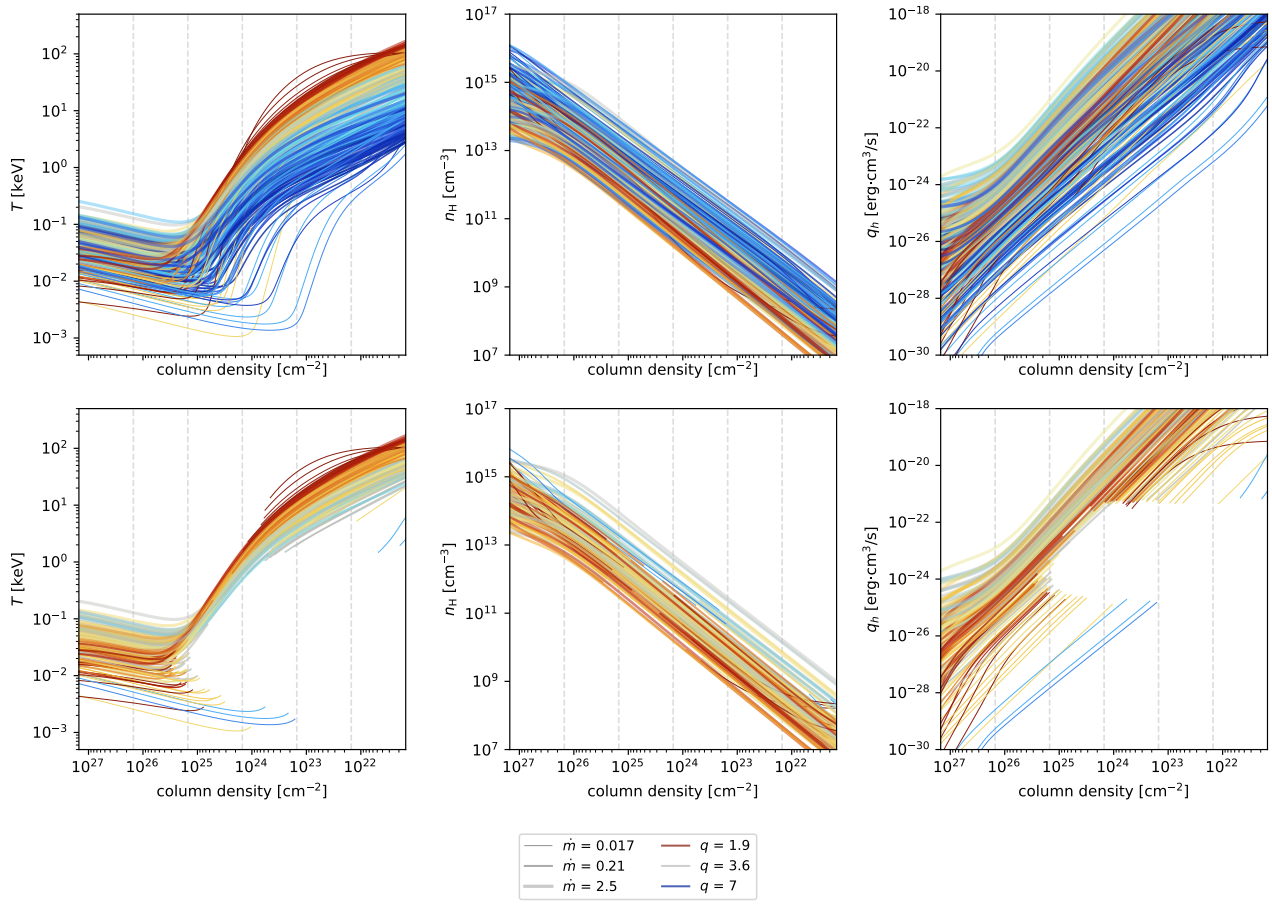

Fig. 6. Vertical structure of temperature, density and dissipation heating rate defined by Eq. (22) for a sample of models computed according to the method described in Sect. 3.4. The first row shows the complete sample of models, while the second row only shows models that do not exhibit density inversion discussed in Sect. 2.4. Zones where TI occurs are omitted, which produces the gaps that are visible in many models. The color of the line corresponds to the magnetic gradient, q, (red is stronger field, blue is weaker), while the thickness shows the accretion rate $\dot{m}$ (thicker is higher). The gray vertical lines show the optical depths τ equal to (from left to right): 100, 10, 1, 0.1, and 0.01.

parameters of individual sources found in Magdziarz et al. (1998), Page et al. (2004), Mehdipour et al. (2011, 2015), Done et al. (2012), Petrucci et al. (2013), Matt et al. (2014), Middei et al. (2018, 2019), Porquet et al. (2018), Ursini et al. (2018). All data points compared to our model in Sect. 3.5 below, are listed in Table 1.

From our random sample of models, we extracted essential parameters as optical depth of the warm corona, its temperature, accretion rate, black hole mass, and magnetic field gradient (all described at the beginning of Sect. 3). The results are shown in Fig. 7, where the random values described in Sect. 3.4 were selected to roughly match the observational points taken from Table 1, in terms of accretion rate and the black hole mass. At the same time, we allowed the magnetic parameters of the disk to vary across a very broad range, namely, from $\beta_0 \approx 10^3$ to $\beta_0 \approx 1$. This allows us to scan all possibilities while remaining close to observations in terms of known quantities. Observations are marked on the right side of the figure according to data analyzed in papers listed in Table 1. Some source are reported twice or even more, but it does not matter since we are interested in the general observational trend of the warm corona.

In the left panel of Fig. 7, we include all results of our models by colored open circles, with no limit to radiation pressure or viscous instability (as long as the model has converged). The size of the circle indicates the value of the accretion rate, while its color reflect the value of magnetic field gradient, both given on

Table 1. Observational points from literature compared to our model.

Source	Type	Refs.
NGC 5548	Sy1	Magdziarz et al. (1998)
Q 0056-363	QSO	Page et al. (2004)
Mrk 876	QSO	
B2 1028+31	QSO	
Mrk 509	Sy1.5	Mehdipour et al. (2011)
RE 1034+396	NLS1	Done et al. (2012)
PG 1048+213	BLS1	
51 sources	AGN1	Jin et al. (2012)
Mrk 509	Sy1.5	Petrucci et al. (2013)
Ark 120	Sy1	Matt et al. (2014)
NGC 5548	Sy1	Mehdipour et al. (2015)
NGC 7469	Sy1	Middei et al. (2018)
Ark 120	Sy1	Porquet et al. (2018)
3C 382	BLRG	Ursini et al. (2018)
NGC 4593	Sy1	Middei et al. (2019)

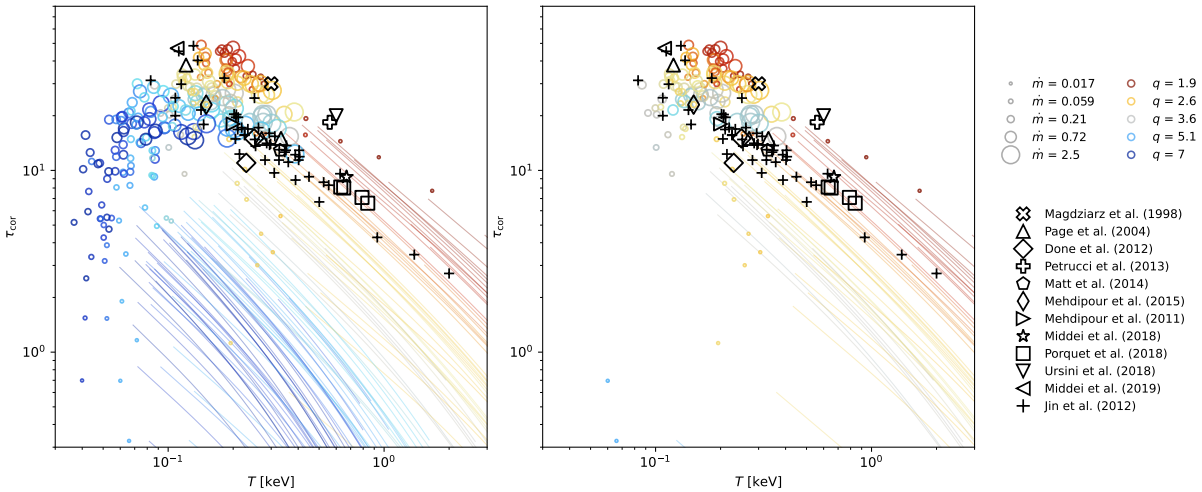

Fig. 7. Parameters of the corona τ_{cor} and T_{avg} determined for a random sample of models are marked by open circles. The size of the points determines the accretion rate and color of the points corresponds to the magnetic field gradient (similar to Fig. 6) given on the right side of the figure. For models where the TI is present, the values of τ and T_{avg} computed at every point of the instability are displayed by thin lines. In the left panel, all models are shown, while in the right panel, models where the density inversion occurs (see Sect. 2.4) are filtered out. Additionally, data points from the literature are drawn using black markers listed on the right side of the figure. The data points clearly follow TI strips.

the right side of the figure. The cloud of points on the τ_{cor}–T_{avg} plane coincide with the observational results, but the range of corona parameters obtained with our numerical code is broader. A clear correlation of magnetic field strength and the accretion rate with resulting corona parameters is seen. Observations follow the models computed for higher accretion rates and moderate magnetic field gradient.

In the right panel of Fig. 7, we removed all the models where the density inversion occurs, which are the models dominated by the radiation pressure and not stabilized by magnetic pressure. We rejected these models because unless convection is present to transfer the energy from the disk, the solution becomes "puffed up" and generally unstable. The models that are removed in this step are mostly models when $\tau_{cor} < 10$ or optically thick models with high accretion and low magnetic field. The data points seem to group around the models which do not display TI in the structure of the warm corona, but some of them follow thin lines, which are thermally unstable zones. The distribution among instability strips can be attributed to our choice of the cutoff of the corona base at the temperature minimum. Had it been chosen according to a different criterion, a more shallow and hotter corona would be obtained. The TI might cause the corona to be shallower than the temperature minimum, which could potentially happen at undetermined point in the vertical structure.

To check at which point the vertical structure the data is in line with the model, we took the black hole mass and the accretion rate for each point from Jin et al. (2012) and we ran a corresponding model, assuming constant magnetic parameters of $\alpha_B = 0.18$, $\eta = 0.21$ and $\nu = 1$. The global disk parameters were chosen to fall roughly in the middle of the range consistent with the observations. We then proceeded to tune the parameter α_B for each model, so that at the optical depth, τ_{cor}, the average temperature yields T_{avg}, with both values taken from the observational data. For some models, it is not possible, but for most (44 objects from the sample of 51), such value of α_B does exist. Both fixed-parameter and fine-tuned models are shown in Fig. 8, where different colors display different global parameters for the disk. The observed cases of T_{avg} versus τ_{cor} are marked by filled circles, while the same parameters as an outcome of our adjusted models are given by crosses. Additionally, using solid thin lines, we plot the averaged temperature integrated from the surface down to the local optical depth given on the x-axis of our graph. The thick solid lines display the extensions of thermally unstable zones. The cases displaying high accretion rates (shown at the top) do not indicate TI. It is clear from the figure that tuning the magnetic parameters does not result in any significant change, which means that the fixed values are a good approximation for this set of observations.

In most cases, the observed optical depth of the warm corona is shallower than the τ_{cor} derived from our model (indicated by crosses in the figure), with the exception of a few models with the lowest accretion rates, where it seems to be deeper than predicted. For a range of models, the location of the warm corona is very coincident with the bottom, rather than the top of the TI, and the locations of the two exhibit some correlation in that range. Above some threshold, our model does not predict the occurrence of the TI, yet the observed optical depth falls short compared to the τ_{cor} from our model.

4. Discussion

We computed a sample of models of the disk-corona vertical structure, where both layers are physically bounded by magnetic field heating as well as Compton and free-free cooling. Our approach to the MRI description is parameterized to adjust the results obtained from simulations, as explained in GR20. The warm, optically thick corona is formed self consistently on the top of an accretion disk for the range of global disk and magnetic parameters. In general, the optical depth of the warm corona is larger for a higher accretion rate and a higher magnetization. Nevertheless, the data show that even models of moderate accretion rates can reproduce the observations when the magnetic parameters are adjusted.

Magnetic heating does not remove the classical TI under constant gas pressure seen in regions of high temperatures on the order of 1 keV and high densities on the order of 10^{12} cm^{-3}, cooled by radiation processes. Interestingly, this kind of TI is

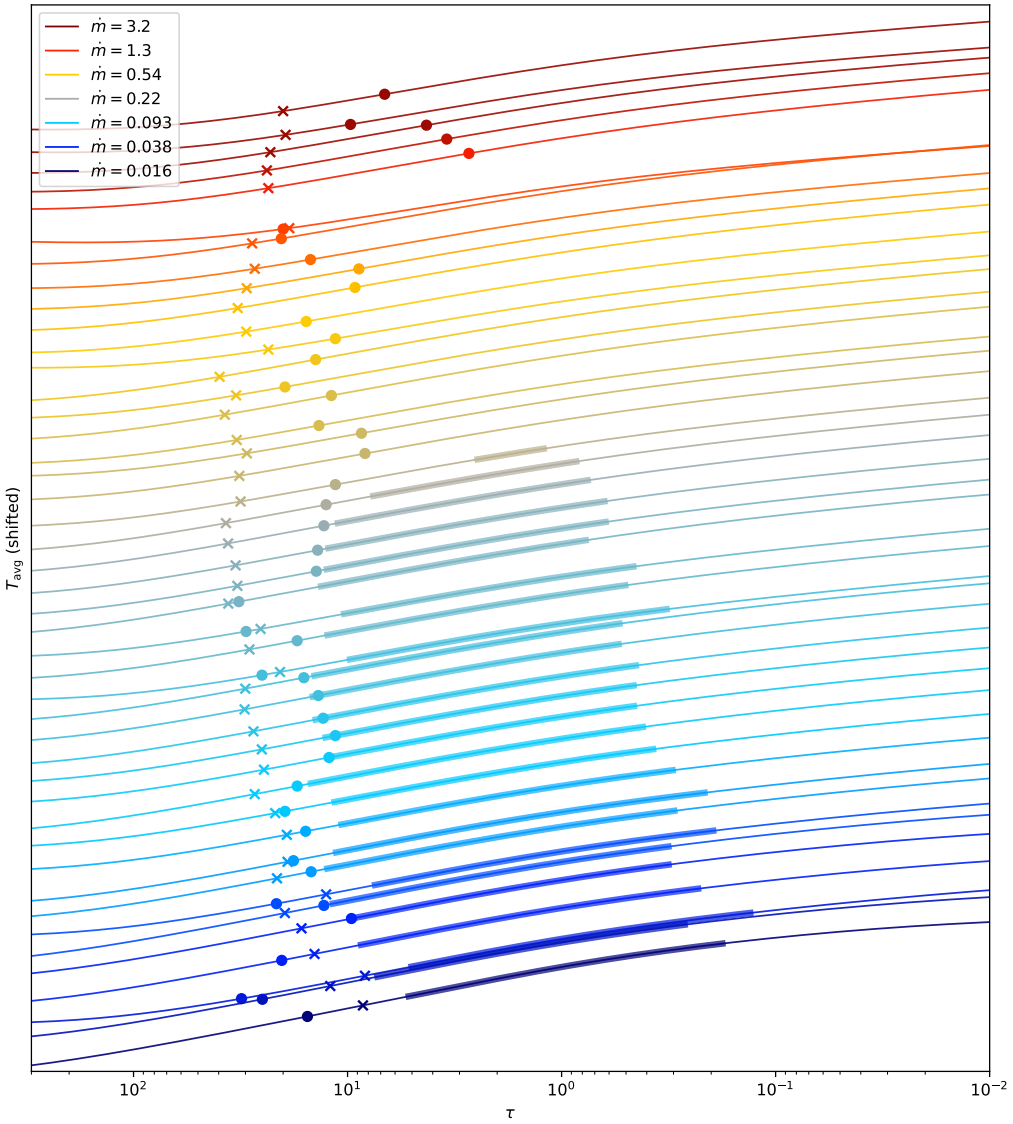

Fig. 8. Profiles of averaged temperature versus the optical depth for fine-tune models. The temperature is averaged between the optical depth given by the coordinate of the horizontal axis and the surface of the corona. Thicker lines are overlayed to indicate where the condition for the TI is fulfilled. Circle markers are temperatures and optical depths obtained by Jin et al. (2012). Cross markers indicate the averaged temperature at $\tau_{\rm cor}$ of a given model. Magnetic parameters are adjusted so that the temperature profile crosses the observational point. Each profile is shifted slightly for a clearer presentation and models are sorted according to the accretion rate, $\dot{m}$.

created only for Compton and free-free absorption or emission. When magnetic heating with simple description of MRI and reconection is taken into account as a main source of gas heating, the disk becomes dominated by magnetic pressure, which acts as a freezer for the TI zone. In order to check this behavior, a stability parameter should be computed under constant gas plus magnetic pressure. In such a case, classical TI exists with negative slope of temperature versus ionization parameter, but the stability parameter under constant gas plus magnetic pressure is always positive. To prove whether such gas is stable, the timescales for TI frozen into magnetic field should be estimated and we plan to do so in the forthcoming paper. In the all previous approaches to the ionized disk atmospheres, the ionization structure was always solved only up to the depth of the photosphere, namely, to the lower branch, which was stabilized due to atomic cooling and heating. Many papers showing such a stability curve never run the computations deeper in the disk structure where the energy is dissipated. In our approach, the magnetic heating that is generated at each point of a vertical structure of the disk and corona provides additional properties to the normal behavior of the gas, namely: the cold disk temperature increases when going towards the equatorial plane, as explicitly presented in panel a of Fig. 1.

Compton and free-free processes fully account for the extension of stability curve from the hot layers on the corona surface, down to the corona base at $\tau_{\rm cor}$. Ionization and recombination may increase the unstable zone, but this should be checked in the future studies. Also, TI may impact the gas evolution on thermal timescales. In the future, time-dependent simulations may show the impact of TI on the warm corona gas.

For all analyzed models, the structure was stable when the isobaric constraint of constant gas plus magnetic pressure was assumed. Of course, such a treatment of a magnetic field only holds true in idealized case, assuming that the field is frozen into matter and there are no significant pressure gradients along the flux tube. If there is a pressure change, the magnetic structure would need to inflate as a whole, without any escape of the matter. Practically, magnetic structures in the corona are tangled and can be considered as pressurized, but open. If a thermal runaway or collapse occurred in a flux tube, matter could be pushed or sucked into the flux tube in order to maintain the pressure equilibrium. In such cases, even in the presence of a strong field, the original criterion of constant gas pressure would hold and strong TI would occur within separate flux tubes, forming prominence-like structures. If we searched for the conditions needed to obtain a uniform, warm corona (and not clumpy prominences), the density n_0 (Eq. (15)) would still be a reasonable order-of-magnitude limitation.

Observations predictions and modeling implications

As we demonstrate in this work, the observations follow our model of a warm corona heated by MRI. All of the data points are in the range $T = 0.01$–$1\,\mathrm{keV}$ and $\tau_{\rm es} = 2$–50. The coronal temperature appears to be strongly correlated with the coronal magnetic field (in particular, its spatial gradient). The accretion rate, on the other hand, seems to increase the optical depth of the corona, at the slight cost of temperature.

Our numerical model has several weaknesses. The greatest limitation to our model is that it is static and one-dimensional. That implies that the corona assumed must be layer-like, clumpy, and unstable, but optically thick clumps cannot be studied. According to the degree that the models are affected by the thermal instability, in our study we were not able definitively exclude the possibility that the clumpy corona can also reproduce the observations. It is possible that a dynamical model could resolve the issue of a local instability, as long as the overall optically thick disk structure survives.

It is also possible that a thin-disk approximation is not well-suited to the problem, as there is growing evidence that multi-layer accretion where the accretion of disk and corona are decoupled may be more realistic (Lančová et al. 2019; Wielgus et al. 2022). We were not able to treat such an accretion mode with our approach.

Another limitation is that we could not obtain the spectrum from our model. While quantities such as optical depth and temperature can be fitted to spectra and we may compare the values with our model, there is some level of degeneracy and the best way to verify the correctness of our predictions would be to at least compare the spectral parameter Γ, which is the slope of the power law usually fitted to the data.

Despite those limitations, our model has allowed us to determine the location and properties of the TI. That said, we cannot exclude that there is a coincidence of occurrence of TI i our models and the warm corona in nature. One peculiar possibility is that the warm corona could actually be driven by the TI. Instead of one layer, many scatterings through more and less dense areas could be more effective than a single, uniform layer in producing a Comptonization spectrum. More investigations are needed using dynamic models that allow for the unstable, clumpy medium to develop (including the magnetic field as essential part to maintain the physical structure of the clumps) and followed by radiative transfer calculations aimed at proving whether such structures can indeed create warm Comptonization signatures.

If we assume the opposite but (as far as we consider) more likely alternative that the clumpy medium does not contribute to the observed spectrum, another interesting possibility emerges. It could be that the corona exists at the verge of the instability. The new warm matter is constantly inflowing, and once it reaches the unstable conditions, it collapses into clumps that are ejected or (more likely) fall back into the disk core. If the condensation timescale is long compared to the dynamical timescale, the matter could exist at the brink of the instability long enough to continuously Comptonizes the soft photons. This could act as a stabilizing mechanism and explain why the observed properties of the warm corona seem to be clustered in a narrow range of the parameter space. While we cannot distinguish which of these scenarios is closer to the truth, the striking coincidence of the warm corona with TI is hard to overlook.

5. Conclusions

We have clearly demonstrated that magnetic heating can produce a warm and optically thick corona above accretion disk in AGN. Obtained theoretical values of coronal temperatures and optical depths agree with those observed for the best known sources. The magnetic viscosity parameter increases the coronal temperature as well as the optical thickness. Magnetic heating does not remove the local thermal instability of the corona (TI) caused by radiation processes in the warm ($\sim$1.0 keV), and dense (above $10^{12}\,\mathrm{cm}^{-3}$) gas. Classical TI operates for accretion rates lower than 0.1 in Eddington units and does not depend much on magnetic viscosity; nevertheless, it is always the combination of those parameters fully determines instability strip. When magnetic heating is taken into account, stability parameter computed under constant gas plus magnetic pressure is always positive, suggesting that thermally unstable zone in the classical way, becomes a kind of frozen into magnetic field and can produce interesting observational features, including soft X-ray excess.

The case of AGNs differs from that of GBHBs, where TI occurs for $\dot{m} < 0,003$ for low $\alpha_{\rm B}$ and $\dot{m} < 0,05$ for high $\alpha_{\rm B}$ (GR20). Also, the optical thickness of the warm corona in AGN is relatively higher than in the case of GBHBs by a factor of 5. Interestingly, TI operates only when Compton heating and free-free emission are introduced. It does not require ionization or recombination processes to be included. Nevertheless, we claim here that ionization may influence the extension of the TI zone and we plan to check it in our future work.

Observations follow TI strip of the warm corona in magnetically supported disk. Thermally unstable gas may undergo evolution under thermal timescale, which, in principle, can be computed in our models. Such theoretical timescale should be compared to the variability measurements of soft corona. We plan to do so in the next step of our project. We conclude here that the TI resulting in the gas, which is cooled due to radiation, may be a common mechanism affecting the existence of the warm corona above accretion disks around black holes across different masses. This is confirmed by the fact that we obtained TI in the disk vertical structure in the case of AGNs considered here, as well as in case of GBHB presented in our previous paper (GR20).

Acknowledgements. This research was supported by Polish National Science Center grants No. 2019/33/N/ST9/02804 and 2021/41/B/ST9/04110. We acknowledge financial support from the International Space Science Institute (ISSI) through the International Team proposal "Warm coronae in

AGN: Observational evidence and physical understanding". Software: FORTRAN, Python (Van Rossum & Drake 2009), Sympy (Meurer et al. 2017), LAPACK (Anderson et al. 1990) and GNU Parallel (Tange 2011).

References

Adhikari, T. P., Różańska, A., Sobolewska, M., & Czerny, B. 2015, ApJ, 815, 83
Anderson, E., Bai, Z., Dongarra, J., et al. 1990, in Proceedings of the 1990 ACM/IEEE Conference on Supercomputing, Supercomputing '90 (Los Alamitos, CA, USA: IEEE Computer Society Press), 2
Ballantyne, D. R. 2020, MNRAS, 491, 3553
Begelman, M. C. 2006, ApJ, 643, 1065
Begelman, M. C., Armitage, P. J., & Reynolds, C. S. 2015, ApJ, 809, 118
Bianchi, S., Guainazzi, M., Matt, G., Fonseca Bonilla, N., & Ponti, G. 2009, A&A, 495, 421
Crummy, J., Fabian, A. C., Gallo, L., & Ross, R. R. 2006, MNRAS, 365, 1067
Done, C., Davis, S. W., Jin, C., Blaes, O., & Ward, M. 2012, MNRAS, 420, 1848
Field, G. B. 1965, ApJ, 142, 531
García, J. A., Kara, E., Walton, D., et al. 2019, ApJ, 871, 88
Gierliński, M., & Done, C. 2004, MNRAS, 349, L7
Gronkiewicz, D., & Różańska, A. 2020, A&A, 633, A35
Haardt, F., & Maraschi, L. 1991, ApJ, 380, L51
Henyey, L. G., Forbes, J. E., & Gould, N. L. 1964, ApJ, 139, 306
Janiuk, A., & Czerny, B. 2011, MNRAS, 414, 2186
Jiang, Y.-F., Stone, J. M., & Davis, S. W. 2014, ApJ, 784, 169
Jin, C., Ward, M., Done, C., & Gelbord, J. 2012, MNRAS, 420, 1825
Kato, S., Fukue, J., & Mineshige, S. 2008, Black-Hole Accretion Disks – Towards a New Paradigm –
Keek, L., & Ballantyne, D. R. 2016, MNRAS, 456, 2722
Krolik, J. H., McKee, C. F., & Tarter, C. B. 1981, ApJ, 249, 422
Lančová, D., Abarca, D., Kluźniak, W., et al. 2019, ApJ, 884, L37
Laor, A., Fiore, F., Elvis, M., Wilkes, B. J., & McDowell, J. C. 1994, ApJ, 435, 611
Laor, A., Fiore, F., Elvis, M., Wilkes, B. J., & McDowell, J. C. 1997, ApJ, 477, 93
Lightman, A. P., & Eardley, D. M. 1974, ApJ, 187, L1
Madau, P. 1988, ApJ, 327, 116
Magdziarz, P., Blaes, O. M., Zdziarski, A. A., Johnson, W. N., & Smith, D. A. 1998, MNRAS, 301, 179
Matt, G., Marinucci, A., Guainazzi, M., et al. 2014, MNRAS, 439, 3016
Mehdipour, M., Branduardi-Raymont, G., Kaastra, J. S., et al. 2011, A&A, 534, A39
Mehdipour, M., Kaastra, J. S., Kriss, G. A., et al. 2015, A&A, 575, A22
Meurer, A., Smith, C. P., Paprocki, M., et al. 2017, PeerJ Comput. Sci., 3, e103
Middei, R., Bianchi, S., Cappi, M., et al. 2018, A&A, 615, A163
Middei, R., Bianchi, S., Petrucci, P. O., et al. 2019, MNRAS, 483, 4695
Page, K. L., Schartel, N., Turner, M. J. L., & O'Brien, P. T. 2004, MNRAS, 352, 523
Pessah, M. E., & Psaltis, D. 2005, ApJ, 628, 879
Petrucci, P.-O., Paltani, S., Malzac, J., et al. 2013, A&A, 549, A73
Petrucci, P. O., Ursini, F., De Rosa, A., et al. 2018, A&A, 611, A59
Petrucci, P. O., Gronkiewicz, D., Rozanska, A., et al. 2020, A&A, 634, A85
Piconcelli, E., Jimenez-Bailón, E., Guainazzi, M., et al. 2005, A&A, 432, 15
Porquet, D., Reeves, J. N., Matt, G., et al. 2018, A&A, 609, A42
Pounds, K. A., Stanger, V. J., Turner, T. J., King, A. R., & Czerny, B. 1987, MNRAS, 224, 443
Różańska, A. 1999, MNRAS, 308, 751
Różańska, A., & Czerny, B. 1996, Acta Astron., 46, 233
Różańska, A., Czerny, B., Życki, P. T., & Pojmański, G. 1999, MNRAS, 305, 481
Różańska, A., Malzac, J., Belmont, R., Czerny, B., & Petrucci, P.-O. 2015, A&A, 580, A77
Salvesen, G., Simon, J. B., Armitage, P. J., & Begelman, M. C. 2016, MNRAS, 457, 857
Shakura, N. I., & Sunyaev, R. A. 1973, A&A, 24, 337
Shakura, N. I., & Sunyaev, R. A. 1976, MNRAS, 175, 613
Shibazaki, N., & Hōshi, R. 1975, Prog. Theor. Phys., 54, 706
Szuszkiewicz, E., & Miller, J. C. 1997, MNRAS, 287, 165
Tange, O. 2011, The USENIX Mag., 36, 42
Ursini, F., Petrucci, P. O., Matt, G., et al. 2018, MNRAS, 478, 2663
Van Rossum, G., & Drake, F. L. 2009, Python 3 Reference Manual (Scotts Valley, CA: CreateSpace)
Walter, R., & Fink, H. H. 1993, A&A, 274, 105
Walton, D. J., Nardini, E., Fabian, A. C., Gallo, L. C., & Reis, R. C. 2013, MNRAS, 428, 2901
Wielgus, M., Lančová, D., Straub, O., et al. 2022, MNRAS, 514, 780

Chapter 4

Paper III: Radiation spectra of warm and optically thick coronae in AGN

A&A 634, A85 (2020)
https://doi.org/10.1051/0004-6361/201937011

Astronomy & Astrophysics

Radiation spectra of warm and optically thick coronae in AGNs

P.-O. Petrucci[1], D. Gronkiewicz[2], A. Rozanska[2], R. Belmont[3], S. Bianchi[4], B. Czerny[5], G. Matt[4], J. Malzac[6], R. Middei[4], A. De Rosa[7], F. Ursini[8], and M. Cappi[8]

[1] Univ. Grenoble Alpes, CNRS, IPAG, 38000 Grenoble, France
e-mail: pierre-olivier.petrucci@univ-grenoble-alpes.fr
[2] Nicolaus Copernicus Astronomical Center, Polish Academy of Sciences, Bartycka 18, 00-716 Warsaw, Poland
[3] Laboratoire AIM (CEA/IRFU – CNRS/INSU – Université Paris Diderot), CEA DSM/IRFU/SAp, 91191 Gif-sur-Yvette, France
[4] Dipartimento di Matematica e Fisica, Università degli Studi Roma Tre, via della Vasca Navale 84, 00146 Roma, Italy
[5] Center for Theoretical Physics, Polish Academy of Sciences, Al. Lotnikow 32/46, 02-668 Warsaw, Poland
[6] IRAP, Université de Toulouse, CNRS, UPS, CNES, Toulouse, France
[7] INAF-Istituto di Astrofisica e Planetologie Spaziali, Via Fosso del Cavaliere, 00133 Rome, Italy
[8] INAF-Osservatorio di astrofisica e scienza dello spazio di Bologna (OAS), Via Piero Gobetti 93/3, 40129 Bologna, Italy

Received 28 October 2019 / Accepted 7 January 2020

ABSTRACT

A soft X-ray excess above the 2–10 keV power-law extrapolation is generally observed in the X-ray spectra of active galactic nuclei. The origin of this excess is still not well understood. Presently there are two competitive models: blurred ionized reflection and warm Comptonization. In the case of warm Comptonization, observations suggest a corona temperature in the range 0.1–2 keV and a corona optical depth of about 10–20. Moreover, radiative constraints from spectral fits with Comptonization models suggest that most of the accretion power should be released in the warm corona and the disk below is basically non-dissipative, radiating only the reprocessed emission from the corona. However, the true radiative properties of such a warm and optically thick plasma are not well known. For instance, the importance of the Comptonization process, the potential presence of strong absorption and/or emission features, and the spectral shape of the output spectrum have been studied only very recently. Here, we present simulations of warm and optically thick coronae using the TITAN radiative transfer code coupled with the NOAR Monte-Carlo code, the latter fully accounting for Compton scattering of continuum and lines. Illumination from above by hard X-ray emission and from below by an optically thick accretion disk are taken into account, as well as (uniform) internal heating. Our simulations show that for a large part of the parameter space, the warm corona with sufficient internal mechanical heating is dominated by Compton cooling and neither strong absorption nor emission lines are present in the outgoing spectra. In a smaller part of the parameter space, the calculated emission agrees with the spectral shape of the observed soft X-ray excess. Remarkably, this also corresponds to the conditions of radiative equilibrium of an extended warm corona covering a non-dissipative accretion disk almost entirely. These results confirm that warm Comptonization is a valuable model that can explain the origin of the soft X-ray excess.

Key words. galaxies: active – radiative transfer – methods: numerical – X-rays: galaxies

1. Introduction

When extrapolating the 2–10 keV power law of type 1 (unabsorbed) active galactic nuclei (AGNs) down to soft X-rays (<2 keV), most of the objects show an excess in emission, the so-called soft X-ray excess. This excess is seen in a large majority of AGNs (e.g., Walter & Fink 1993; Page et al. 2004; Gierlinski & Done 2004; Bianchi et al. 2009) and its origin is still not well understood. Two interpretations are generally discussed: blurred ionized reflection (e.g., Crummy et al. 2006; Walton et al. 2013) and Comptonization in a warm ($T \sim 1$ keV) and optically thick ($\tau \sim 10$–20) corona (e.g., Magdziarz et al. 1998; Jin et al. 2012; Petrucci et al. 2013, hereafter P13; Petrucci et al. 2018, hereafter P18; Porquet et al. 2018, and references therein).

Both interpretations give a good fit to the data but both have their own limitations (see discussion in García et al. 2019). Blurred ionized reflection models generally require extreme values for the spin and hot corona compactness, as well as large ionization degree and large densities (see e.g., Jiang et al. 2019a,b) which can also significantly reduce the inferred iron abundances compared to typical (e.g., with density generally equal to 10^{15} cm^{-3}) reflection models (e.g., Tomsick et al. 2018). On the other hand, only a few attempts have been made so far to realistically model the warm corona emission (e.g., Ballantyne 2020). At such low temperature (around 1 keV), large atomic opacities could dominate over the Thomson opacities. This would have two major consequences: Comptonization would not dominate the emitting processes and strong absorption and/or emission features could be present in the output spectrum in contradiction with observations. If true, this would invalidate warm Comptonization as an origin of the soft X-ray excess.

The warm Comptonization modeling of the soft X-ray excess was carefully tested with the data set from the large broadband campaign on Mrk 509 (Kaastra et al. 2011; Petrucci et al. 2013). The data were fitted with the so-called "two-coronae" scenario (see the sketch of Fig. 1). This latter assumes two Comptonization model components, one for the UV-Soft X-rays to simulate the warm corona emission, and one for the hard X-rays to simulate the standard hot corona emission. The model gave statistically good fits for all the observations of the campaign and provided very interesting information on the geometry of each corona (see P13 for more details). Importantly

for the present paper, the warm corona was found to agree very well with a powerful, extended, and optically thick plasma covering a nondissipative accretion disk; that is, all the accretion power would be released in the warm corona, the underlying disk radiating only the reprocessed emission produced by the warm corona. Analyses of larger AGN samples give similar conclusions (e.g., P18). While the two-coronae approach has been successfully applied to several AGNs (e.g., Magdziarz et al. 1998; Czerny et al. 2003; Jin et al. 2012; Matt et al. 2014; Mehdipour et al. 2015; Ursini et al. 2016, 2018; Middei et al. 2018, 2019; Porquet et al. 2018; Kubota & Done 2018), fundamental questions remain unanswered: Can a warm and optically thick corona exist in the upper layers of the accretion flow? Can its spectral emission be dominated by Comptonization and be in agreement with the observed soft and smooth X-ray spectral shape?

A realistic radiative transfer study of an optically thick and warm plasma is not simple however. The optical depth is neither very small nor very large, meaning that radiative transfer cannot be simply approximated. As mentioned above, the temperature is also in a range of values where lots of ions are expected and line emission and/or absorption processes have to be included. Last but not least, the corona heating power has to be locally released as suggested by observations. Różańska et al. (2015, hereafter R15) performed a theoretical study of the existence of such a warm optically thick corona at the surface of a standard accretion disk assuming both radiative and hydrostatic equilibrium. This latter study shows that it is indeed possible to obtain solutions that have the required temperature. Specifically the best conditions are obtained when most of the power of accretion is released into the corona rather than the disk. Nevertheless, the requirement of hydrostatic equilibrium with the underlying disk puts an upper limit on the warm corona optical depth of approximately five. However, R15 also showed that for larger optical depth, large magnetic-to-gas pressure is needed (>30) to keep such a thick corona in hydrostatic equilibrium with negligible free-free emission. The impact of magnetic pressure on the formation of the warm corona has recently been studied in the case of accretion disks in X-ray binaries (XrB) by Gronkiewicz & Różańska (2020). While the estimates of R15 suggest that a warm corona could indeed exist, no spectral emission was simulated. Line radiative transfer was also left out of the computation, preventing a clear answer to the importance of the emission and/or absorption lines in the thermal equilibrium and the output spectrum produced by this optically thick and warm plasma.

The goal of this paper is to simulate energy-dependent spectra of warm coronae in radiative equilibrium thanks to the state-of-the-art radiative transfer code TITAN coupled with the Monte-Carlo code NOAR (Dumont et al. 2003). We first introduce a few parameters and recall in Sect. 2 some analytical estimates of radiative transfer equations in the case of a gray optically thick scattering medium with dissipation. We detail the main characteristics of the TITAN and NOAR codes in Sect. 3.1 and present the results of our simulations in Sect. 3. We discuss these results in Sect. 4 before presenting our conclusions.

2. Analytical estimates

We recall here the analytical solutions of radiative transfer equations for the warm corona with additional heating located above an accretion disk. To ease the analysis, we adopt here a number of simplifying assumptions with respect to the numerical calculations described in the following section. Here we assume

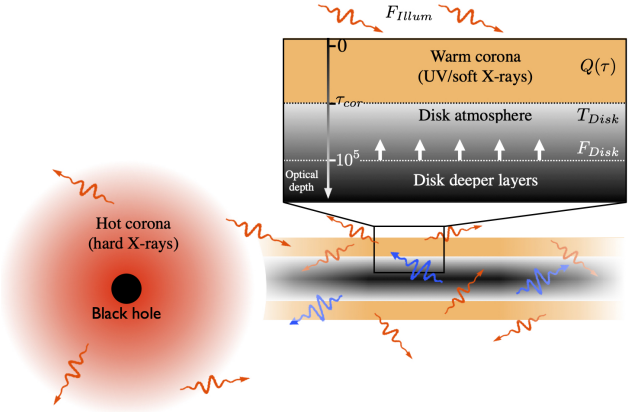

Fig. 1. Sketch of the two coronae approach. A hot ($kT \sim 100$ keV) and optically thin ($\tau \sim 1$) corona (in red) is present in the inner parts of the accretion flow close to the black hole. This produces the hard X-ray emission through Comptonization of the soft photons coming from the outer part of the flow. The outer accretion flow is a vertically structured accretion disk (a zoom is shown in the figure) with cold and optically thick matter in the deeper layers (in black), characterized by a temperature $T_{\rm bb}$ and threaded by a vertical radiative flux $F_{\rm disk}$, while the upper layers (in orange) are composed of a warm ($kT \sim 1$ keV) and optically thick ($\tau_{\rm cor} \sim 10$–20) corona possessing a source of internal heating power $Q(\tau)$. The warm corona is also illuminated from above by an illumination flux $F_{\rm Illum}$ produced by the hot corona. This sketch is partly inspired from Różańska et al. (2015).

a gray atmosphere with pure scattering (i.e., we neglect emission and absorption from bound-free and bound-bound transitions). We also assume that the atmosphere is optically thick, and therefore adopt the Eddington approximation in the whole medium. We assume a constant density $n_{\rm H}$ throughout the atmosphere and we use $\tau_{\rm cor}$ to refer to its total Thomson optical depth. The corona is assumed to be heated with a uniform rate per unit optical depth and per unit solid angle Q (erg s^{-1} cm^{-2} str^{-1}). For simplicity, we neglect any illumination from above the corona. The disk is supposed to radiate like a black body of temperature $T_{\rm bb}$ and we use B to denote the frequency integrated black-body radiation intensity, that is, $B(T_{\rm bb}) = \sigma T_{\rm bb}^4/\pi$. The disk is also characterized by its intrinsic flux $F_{\rm disk}^{\rm int}$ produced through internal dissipation (see Fig. 1). The disk can still radiate ($B > 0$) even if the disk is nondissipative, that is, $F_{\rm disk}^{\rm int} = 0$. In this case, it radiates only by reprocessing the corona flux emitted downward towards the disk. On the other hand, if the corona intercepts only a small fraction of the disk emission, B can be very small, and potentially vanish.

We follow the analytical computations of R15, but we present the equations in a slightly different way, which is useful to understand the results of the numerical simulations presented in the following sections. From now on, the part of the radiative transfer variables emitted upward with respect to the disk is denoted with a plus symbol (+) and the part emitted downward is denoted with a minus symbol (−).

The frequency-integrated radiation transfer equation with an additional input energy rate per unit optical depth and solid angle Q, can be written as:

$$\mu \frac{{\rm d}I}{{\rm d}\tau} = I - J - Q, \tag{1}$$

where μ is the cosine of the azimuthal angle. The optical depth, τ is measured downward, from the top of the corona toward

the disk, $I(\mu, \tau)$ is the radiation true intensity, and $J(\tau)$ is the radiation mean intensity, that is, the intensity averaged over the angles.
In a gray atmosphere and assuming the Eddington approximation in the whole medium, the parts of the radiation intensity emitted upward ($\mu > 0$) $I^+(\tau)$ and backward ($\mu < 0$) $I^-(\tau)$ are given by:

$$I^+(\tau) = J(\tau) + 2H(\tau), \quad (2)$$

$$I^-(\tau) = J(\tau) - 2H(\tau), \quad (3)$$

where $H(\tau)$ is the zeroth moment of Eq. (1). It gives the net flux crossing the corona at each optical depth τ inside the slab. Following R15, the expressions of $J(\tau)$ and $H(\tau)$ are given by:

$$J(\tau) = 3\frac{F_{\rm out}}{4\pi}\left[\frac{2}{3} + \tau - \frac{\chi\tau^2}{2\tau_{\rm cor}}\right], \quad (4)$$

$$H(\tau) = \frac{F_{\rm out}}{4\pi}\left(1 - \frac{\chi\tau}{\tau_{\rm cor}}\right), \quad (5)$$

where $F_{\rm out}$ is the corona escaping radiation flux at its surface[1], that is, at $\tau = 0$. In these equations, the parameter χ is defined by

$$\chi = \frac{F_{\rm cor}}{F_{\rm out}}, \quad (6)$$

where $F_{\rm cor}$ is the flux produced through dissipation in the corona:

$$F_{\rm cor} = 4\pi Q\tau_{\rm cor}. \quad (7)$$

From Eq. (5), χ can be rewritten as:

$$\chi = \frac{\tau_{\rm cor}Q}{H(\tau_{\rm cor}) + \tau_{\rm cor}Q}. \quad (8)$$

Now, at the base of the corona, we simply have:

$$I^+(\tau_{\rm cor}) = J(\tau_{\rm cor}) + 2H(\tau_{\rm cor}) = B. \quad (9)$$

Combining Eqs. (4), (5), and (9), we can express $H(\tau_{\rm cor})$ as a function of the different parameters of the problem:

$$H(\tau_{\rm cor}) = \frac{B}{4 + 3\tau_{\rm cor}} - \frac{\tau_{\rm cor}Q}{2}. \quad (10)$$

The function $H(\tau_{\rm cor})$ gives the net flux crossing the base of the corona, that is, the difference between the flux emitted upward inside the corona and the flux emitted downward by the corona inside the disk. This difference cannot be smaller than $-\tau_{\rm cor}Q/2$ which is reached in the extreme case of no disk emission ($B = 0$).

The value of $H(\tau_{\rm cor})$ can be interpreted in terms of different conditions of the disk-corona radiative equilibrium:

– $H(\tau_{\rm cor}) = 0$: this corresponds to $\chi = 1$. This is the condition when the upward flux perfectly compensates the downward flux at the base of the corona. In the case of a warm corona covering the disk entirely, this imposes that the disk is nondissipative, that is, $F^{\rm int}_{\rm disk} = 0$

– $H(\tau_{\rm cor}) > 0$: this corresponds to $\chi < 1$. In this case, the upward flux entering the warm corona at its base is larger than the downward one. This is the case of slab corona above a dissipative disk with $F^{\rm int}_{\rm disk} > 0$, for example.

– $H(\tau_{\rm cor}) < 0$ but $> -\frac{\tau_{\rm cor}Q}{2}$: this corresponds to $2 > \chi > 1$. In this case, the upward flux entering the warm corona at its base is smaller than the downward one. One example of this is the case of a patchy corona above a nondissipative disk ($F^{\rm int}_{\rm disk} = 0$), where part of the disk emission does not entirely reenter the warm corona.

These analytical results do not take into account heating due to external illumination or other radiation processes (lines, edges, free-free). The full treatment of the radiation transfer problem requires numerical simulations presented in the following sections.

[1] $F_{\rm out}$ is denoted $F^{\rm tot}_{\rm acc}$ in R15.

3. Simulations

3.1. TITAN and NOAR code

To calculate the radiative equilibrium and the output spectra of a dissipative warm corona we used the newest version of the radiative transfer code TITAN (Dumont et al. 2003) coupled with the Monte-Carlo NOAR code (Dumont et al. 2000; Abrassart & Dumont 2001).

TITAN is a one-dimensional code that allows the user to compute the structure- and angle-dependent emergent spectra of hot photoionized gas by solving the radiative transfer simultaneously with ionization and thermal equilibrium. This can be done assuming a constant density, a constant pressure, or a hydrostatic equilibrium prescription. On the "top" side of the gas slab, TITAN allows illumination by radiation of any spectral energy distribution (SED); on the "disk" side it allows the boundary condition to be set for black-body illumination to account for the presence of a colder disk underneath.

Assuming the balance between ionization and recombination of ions, excitation and de-excitation, and the most important atomic lines, TITAN computes the physical state of the gas at each depth in thermal and pressure equilibrium. About 4000 line transitions are included in the TITAN code. The population of each ion level is computed by solving the set of ionization equations coupled with the set of statistical equations describing the excitation equilibrium in full nonlocal thermal equilibrium (NLTE). Free-free emission is fully taken into account. The code was designed to work with optically thick media and solves the radiative transfer equation both in continuum and lines using the Accelerated Lambda Iteration (ALI) method (Collin et al. 2004). The computations are done assuming a complete redistribution function in the lines. Partial redistribution is mimicked by a Doppler profile for some of the most intense resonant lines.

The Compton heating and cooling balance of the matter is taken into account by solving simultaneously for the temperature structure and the radiation field. Although TITAN includes most relevant processes, it does not take into account the Compton heating of the radiation field and the corresponding photon energy shift via Comptonization in the emergent spectra. The former effect is mainly significant for $\chi > 1$ and in this case the temperature computed by TITAN can be overestimated by a factor of a few. To take into account the latter effect, we use the Monte Carlo code NOAR that takes the density, temperature, and ionization structure of the slab calculated by TITAN and computes the emergent spectra on both sides of the slab.

The coupling between TITAN and NOAR allows a complete treatment of the emission from a photoionized, Comptonized medium. It can be used in a variety of cases, such as illuminated disk atmospheres (Różańska et al. 2002) and warm absorbers (Różańska et al. 2006) in AGNs.

For the purpose of this paper we consider a warm constant-density corona and an illumination from above, normal to the

disk[2]. The computational pipeline that we built runs TITAN with different values of the following parameters: gas density $n_{\rm H}$ in the range $[10^9$–$10^{14}]\,{\rm cm}^{-3}$, total optical depth $\tau_{\rm cor}$ in the range [2–40], local heating rate $q_{\rm h}$ in the range $[10^{-23}$–$10^{-19}]\,{\rm erg\,s^{-1}\,cm^3}$, ionization parameter ξ_0 of the "top" side illumination[3] (assuming a power law with spectral photon index of 1.8 in the energy range 50 eV–100 keV) in the range $[10$–$3\times10^5]\,{\rm erg\,s^{-1}\,cm}$ and illumination black-body temperature $T_{\rm bb}$ on the "disk" side in the range $[3\times10^4$–$10^6]$ K. We emphasize that the ionization parameter ξ_0 is directly linked to the flux of the incoming radiation at the surface of the slab, but TITAN takes also into account the spectral shape of this incoming radiation in the radiative transfer computation. The mechanical heating rate $q_{\rm h}$ is supposed to be uniform throughout the entire slab. It is related to the heating power per unit optical depth and solid angle Q defined in Sect. 2:

$$q_{\rm h} = 4\pi Q\sigma_{\rm T}/n_{\rm H}. \tag{11}$$

TITAN computes the ionization and temperature structure of the slab. We then use this structure to run NOAR in order to simulate the effects of photon energy shifts due to Comptonization. We run NOAR twice: once illuminating the slab by the power law, and then invert the structure and illuminate it with a black-body SED in order to simulate the soft flux from the disk below the corona. We then normalize the obtained spectra from photons to physical unit by correlating them with TITAN. In this way, despite two independent runs of NOAR, we can obtain the combined spectrum of reflection and soft Comptonization or either of the components separately. In the end, the final spectra are analyzed to extract the values shown in the maps.

We performed hundreds of simulations varying the five parameters $n_{\rm H}$, $\tau_{\rm cor}$, $q_{\rm h}$, ξ_0 and $T_{\rm bb}$. For each simulation, we can compute the value of χ given by (see Eqs. (8) and (10)):

$$\chi = \frac{\tau_{\rm cor} Q}{\frac{B}{4+3\tau_{\rm cor}} + \frac{\tau_{\rm cor} Q}{2}}. \tag{12}$$

Some of these simulations did not converge in some part of the parameter space. The true reason for this is not clear yet. The matter on the back side of the cloud can become too cool and too optically thick, below the actual limitations of the TITAN code. However, this lack of convergence could also be linked to thermal instabilities that could exist at large τ. While it is not a problem that is simple to understand and solve, it has no impact on the results of the present paper since this part of the parameter space (mainly characterized by $q_{\rm h} < 10^{-23}\,{\rm erg\,s^{-1}\,cm^3}$) is not relevant to emission in the soft X-ray band (overly low corona temperature). For this reason, we present only simulations with $q_{\rm h} > 10^{-23}\,{\rm erg\,s^{-1}\,cm^3}$. We plan to improve TITAN simulations for gas of much greater optical depth in future work.

Moreover, since the main goal of this analysis is to study the spectral properties of the warm corona, we only consider the intrinsic warm corona emission spectrum and ignore any reflected components originating from the hot corona. Reflection due to external illumination will be considered in a forthcoming paper.

[2] We do not expect the effects of anisotropy of the illumination to have a significant influence on the thermal structure of the warm corona (which is the main goal of this publication). Indeed, after a few τ, these anisotropy effects will be spread out by the multiple photon scatterings.

[3] By definition $\xi_0 = F_{\rm illum}/n_{\rm H}$ with $F_{\rm illum}$ the illuminating flux impinging on the slab surface (see Fig. 1).

3.2. Results

The two following sections present results from a subset of simulations where the warm corona density $n_{\rm H} = 10^{12}\,{\rm cm}^{-3}$, the disk temperature $T_{\rm bb} = 10^5$ K, and the ionization parameter $\xi_0 = 10^3\,{\rm erg\,s^{-1}\,cm}$. These are typical values (e.g., Rees 1984) for AGNs with a black hole mass of 10^8 solar masses such as for example Mkn 509. We discussed the effects of these parameters on our solutions in Sect. 3.2.3.

3.2.1. Compton dominated

The left panel of Fig. 2 shows a map of the ratio of the Compton cooling $p_{\rm compt}$ to the warm corona internal heating $q_{\rm h}$ in the χ–$\tau_{\rm cor}$ plane. The color scale goes from 20 to 100%. For a very large part of the parameter space, Compton cooling is clearly the dominant (>90%) cooling process that balances the internal heating of the warm corona. This is the first important result of this work; it justifies the main hypothesis used in the two-coronae approach where the warm corona emission is modeled with pure Comptonization codes.

The Compton cooling becomes less dominant at lower χ and larger $\tau_{\rm cor}$ where free-free and line processes start to play a role. The right panel of Fig. 2 shows the vertical distribution of the different heating and cooling processes for two simulations with $\tau_{\rm cor} = 20$ but with two different values of χ : 1.35 and 0.753. This corresponds to the two simulations indicated by an "x" and a "+", respectively, in the left panel of Fig. 2; Compton cooling represents more than 90% of the total cooling processes in the case $\chi = 1.35$, and less than 70% for $\chi = 0.753$.

The solid green line overplotted in the left panel of Fig. 2 corresponds to the condition $\chi = 1$, that is, the value expected in the case of radiative equilibrium between a slab corona and the nondissipative disk that it covers entirely (see Sect. 2). The region above the green line agrees with a nondissipative disk covered by a patchy corona. The dashed contours in the left panel of Fig. 2 correspond to different values of the covering factor from 0.95 to 0.40 (see Eqs. (A.6) and (A.9) for the general expression of χ as a function of the covering factor). On the other hand, the region below the green lines agrees with a slab corona above a dissipative disk.

3.2.2. Temperature and spectral shape

The left panel of Fig. 3 shows the same map of the ratio of the Compton cooling $p_{\rm compt}$ to the warm corona internal heating $q_{\rm h}$ as in Fig. 2 but we have now over plotted the contours of the average corona temperature in dotted lines. This temperature is defined as $T_{\rm avg} = \frac{1}{\tau_{\rm cor}}\int_0^{\tau_{\rm cor}} T(\tau){\rm d}\tau$. An example of the temperature vertical distribution $T(\tau)$ for $\tau_{\rm cor} = 20$ and $\chi = 1.35$ and 0.753 is plotted in the right panel of Fig. 3. The Compton cooling being dominant, the electron temperature naturally decreases with τ due to the increase of the soft photon flux while the heating Q is assumed to be constant (see R15). As expected, for larger χ (i.e., larger corona heating with respect to the total radiative cooling) the corona temperature is higher.

For each simulation, our code also computes the spectrum emitted upward by the warm corona. Each spectrum is fitted above 100 eV with a cut-off power law. The dot dashed lines reported in the left panel of Fig. 3 correspond to different spectral photon indices of these spectra between 1.8 and 4.5. As an example, Fig. 4 shows the simulated spectra emitted by the warm corona for $\tau_{\rm cor} = 20$ and $\chi = 1.35$ (red line) and 0.753

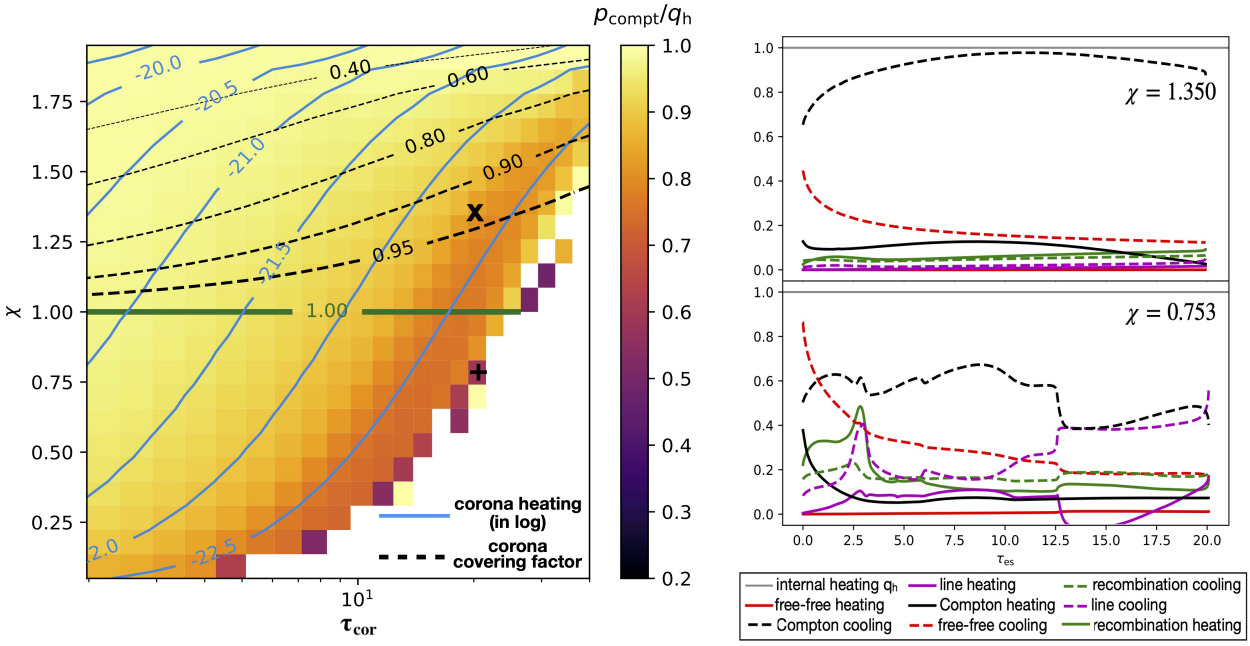

Fig. 2. *Left*: map of the average Compton cooling $\left(p_{compt} = \frac{1}{\tau_{cor}} \int_0^{\tau_{cor}} p_{compt}(\tau) d\tau\right)$ to the warm corona heating (q_h) ratio in the χ–τ_{cor} plane, with χ being defined by Eq. (12). The color scale on the right ranges from 20 (black) to 100% (white). The other parameters are fixed to $T_{bb} = 10^5$ K, $\xi_0 = 10^3$ erg s^{-1} cm, and $n_H = 10^{12}$ cm^{-3}. The solid green line refers to $\chi = 1$, that is, the case of radiative equilibrium between a corona and a nondissipative disk that it covers entirely; it divides the χ–τ_{cor} into two regions that can be characterized by different radiative equilibrium properties (see Sect. 2). The region above the green line, that is, $\chi > 1$, agrees with a nondissipative disk covered by a patchy corona. The dashed lines correspond to different values of the corona covering factor from 0.95 to 0.40 (see Eq. (A.9)). The region below the green line, that is, $\chi < 1$, agrees with a slab corona above a disk which is now dissipative ($F_{disk} > 0$). The blue contours correspond to different values of the logarithm of the warm corona heating q_h (in unit of erg s^{-1} cm^3). *Right*: cooling and heating process fractions with respect to the warm corona heating q_h across the corona for $\tau_{cor} = 20$ but for two different values of χ, 0.753 (*bottom*) and 1.35 (*top*). This corresponds to the simulations indicated in the left panel with either a "+" or an "x", respectively.

(blue line). In the former case, the spectrum can be fitted with a cut-off power law with $\Gamma \simeq 2.5$ and $E_c \simeq 2$ keV while for $\chi = 0.753$ we find $\Gamma \simeq 4.3$ and $E_c \simeq 10$ keV[4]. We also report in this figure the black-body spectrum (black line) emitted by the disk at the bottom of the warm corona. The difference in flux between the disk black-body and the corona spectra results from the large opacity of the warm corona. This reduces the flux of the disk by a factor of approximately $\frac{1}{1 + \frac{3}{4}\tau_{cor}}$ after scattering through the corona.

Observationally, when fitted with a Comptonization model, the photon index of the soft X-ray excess is generally between 2.2 and 3.2 and peaks around 2.5 and the temperature is between ~0.1 and ~2 keV (see e.g., P18 and references therein). Very interestingly, there is a region of our parameter space with the correct range of temperatures and photon indices. This corresponds to the dark area in the left panel of Fig. 3. Moreover, this region is not far from the solid green line that corresponds to the condition $\chi = 1$, that is, the expected value for a slab corona covering a nondissipative disk entirely. Alternatively, when we compare the position of the dark area of Fig. 3(left) with Fig. 2(left), it is in better agreement with a slightly patchy corona with a covering factor in between ~0.9 and ~1. This is another important result of these simulations, and confirms the modeling done by R15 and agrees with the observational estimates of P13 and P18.

As explained in Sect. 3.1, because TITAN does not take into account the Compton heating of the radiation field, the plasma temperature can be over-estimated in our computations. However, this effect is only significant for $\chi > 1$, and only the temperatures in the upper part of Fig. 3(left) are expected to be smaller than the ones computed by TITAN. A precise estimate is not easy to obtain, but it means that the dark region is expected to be even larger than the one shown in Fig. 3.

It is also worth noting that we cannot exclude disk–corona geometries that would combine a lower covering factor with a more dissipative disk. While not impossible, the required fine tuning between the covering factor and the disk intrinsic dissipation to be in the right ranges of observed temperatures and spectral indices is not easy to explain from a physical point of view, making this option relatively unlikely.

3.2.3. Dependencies on ξ_0, n_H and T_{bb}

In order to check the dependency of our results on the different parameters of the simulations, we tested different disk temperatures T_{bb}, different corona densities n_H, and different values of the ionization parameter ξ_0 of the illumination from above. Figure 5 presents the contours of the warm corona temperature (blue lines) and warm corona spectral photon index (black dashed lines) in the planes (from left to right) χ–T_{bb}, χ–n_H, and χ–ξ_0 for a corona optical depth τ_{cor} fixed to 20.

[4] It is known that an exponential cut-off is a poor approximation of the cut-off of realistic Comptonization models (e.g., Petrucci et al. 2000); it overpredicts the corona temperature by a factor of two to three which is indeed what we observe.

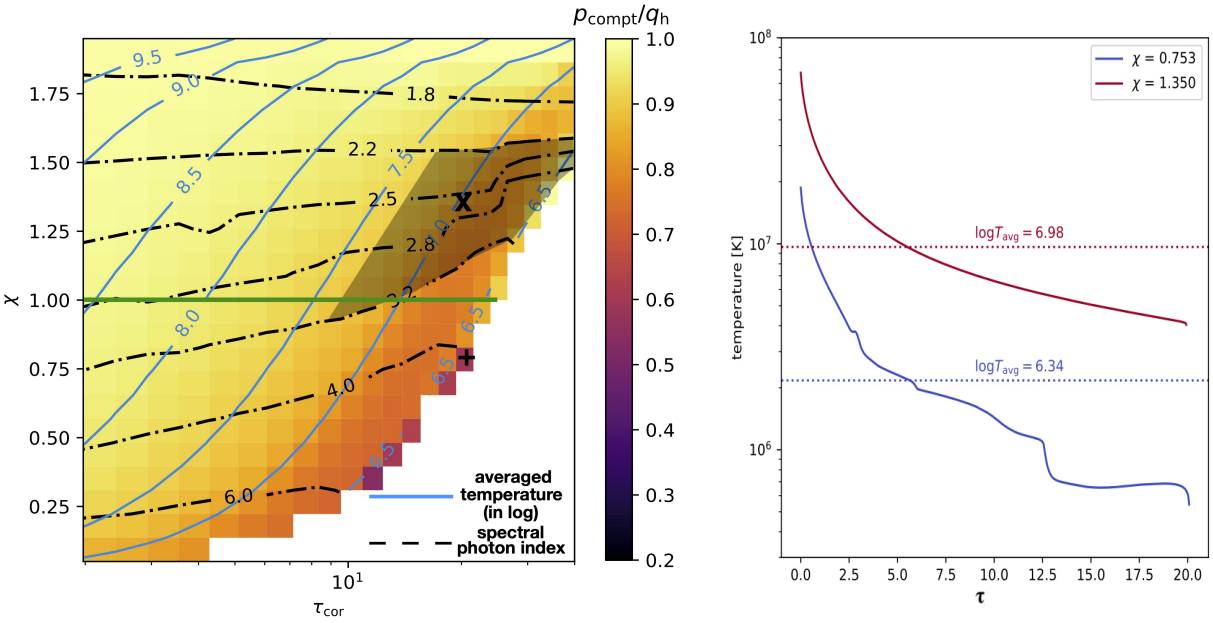

Fig. 3. *Left*: same map as in Fig. 2 but with the contours of the logarithm of the vertical average coronal temperature (in Kelvin, blue solid line) and the contours of the photon indices of the output spectrum produced by the corona (black dot-dashed lines). The other parameters are fixed to $T_{bb} = 10^5$ K, $\xi_0 = 10^3$ erg s^{-1} cm, and $n_H = 10^{12}$ cm^{-3}. Similarly to Fig. 2 the green line corresponds to the condition $\chi = 1$. The darkened area corresponds to the usual observational constraints of the temperature (0.1–2 keV) and photon index (2.2–3.2) of the soft X-ray excess. *Right*: vertical coronal temperature profiles for $\tau_{cor} = 20$ and $\chi = 1.35$ and 0.753. The corresponding average temperatures $T_{avg} = \frac{1}{\tau_{cor}} \int_0^{\tau_{cor}} T(\tau) d\tau$ are indicated for each temperature profile.

These figures show that for large T_{bb} or low n_H or ξ_0, the temperature and the spectral photon index of the warm corona emission are almost insensitive to these parameters. In the case shown here, that is, $\tau_{cor} = 20$, this corresponds to $T_{bb} > 10^5$ K, $n_H < 10^{12}$ cm^{-3} or $\xi_0 < 10^4$. In this region of the parameter space, the properties of the warm corona are mainly driven by χ. However, for smaller T_{bb} or larger density, n_H, or ionization parameter, ξ_0 , the radiative and spectral properties of the corona depend significantly on these parameter values. The background colors in Fig. 5 correspond to the Compton-cooling-to-corona-heating ratio p_{compt}/q_h, whose color scale is reported on the right of the figure.

The dependencies of the corona emission spectral shape on T_{bb} and n_H can be explained by the properties of the Comptonization process in an environment in radiative equilibrium. At low density or high disk temperature, our simulations show that the corona emission is dominated by Comptonization. In this case, as long as the heating over cooling of the warm corona remains constant, no significant spectral variability is expected. The corona heating is directly related to the sum of the internal heating Q and the illumination ξ_0 while the cooling is related to $B = \sigma T_{bb}^4$. They are all related to one another through the net flux crossing the base of the corona (see Eq. (10)). As long as the illumination is negligible with respect to warm corona internal heating power, a constant χ implies a constant heating-to-cooling ratio and the warm corona temperature is not expected to change. The warm corona optical depth being fixed, the spectral shape of the warm corona emission remains roughly constant. This is very similar to the constancy of the spectral shape of the emission from a hot optically thin corona in radiative equilibrium with the surrounding soft photon field (e.g., Haardt & Maraschi 1991; Haardt 1993; Petrucci et al. 2000; Tortosa et al. 2018).

However, for densities larger than $\sim 10^{12}$ cm^{-3} and disk temperatures lower than $\sim 10^5$ K, the dependence on these parameters becomes important. This is due to the fact that in this part of the parameter space, the corona radiative processes are less dominated by Comptonization, either because the soft seed photon flux decreases (at low T_{bb}) or the free-free and bound-free processes increase (at high density) through their dependence on the density squared. The previous discussion in terms of radiative equilibrium no longer holds. At constant χ, decreasing T_{bb} or increasing n_H results in a decrease of the temperature and a steepening of the warm corona spectrum. These conditions are thus less favorable to producing spectra that could reach the soft X-ray band and produce a significant soft X-ray excess.

The dependence of the spectral shape and temperature of the warm corona on the ionization parameter ξ_0 is quite different. The spectral shape and temperature are almost independent of ξ_0 unless this latter becomes larger than a few 10^4 erg s^{-1} cm. While for such values of ξ_0, the warm corona is dominated by Compton cooling, the spectral shape (photon index and temperature) varies with ξ_0 and the lower the χ the larger the variation. In fact, increasing ξ_0 increases the heating of the corona which is not compensated by a similar increase of the cooling given the small fraction of the illumination flux that reaches the disk (because of the large corona optical depth) and is reprocessed there. At constant χ, this implies an increase of the warm corona temperature and a hardening of the spectra. This is interesting because it shows that even for small χ, the warm corona can produce spectra in agreement with the soft X-ray excess spectral properties if the illumination is strong enough.

Since the spectral shape and temperature of the warm corona vary in a similar way for opposite variations of the illumination and the density, an increase of the illumination could attenuate any effects seen in the spectral shape caused by an increase in

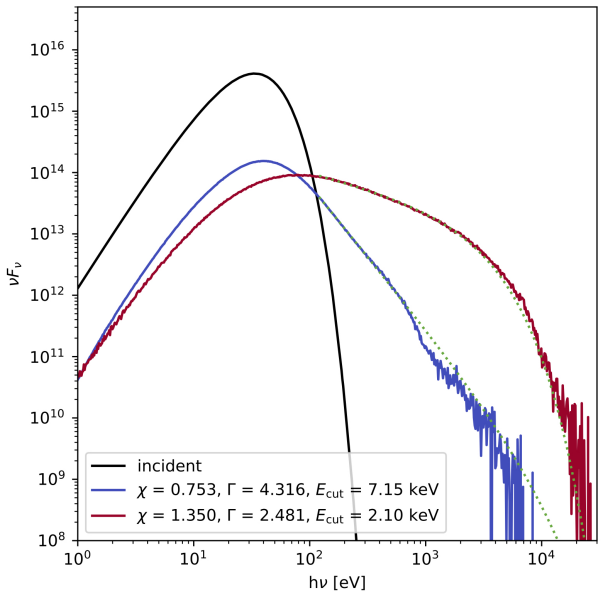

Fig. 4. Two examples of simulated spectra emitted by the warm corona for $\tau_{cor} = 20$ and two different values of χ : 1.35 (red) and 0.753 (blue). The best fit values for the photon index and high-energy cut-off when the spectra are fitted with a high-energy exponential cut-off power law are indicated in the figure. The simulation corresponding to the red spectrum is represented by the "x" in Fig. 3 and is in the parameter space which agrees with the spectral shape of the soft X-ray excess. On the contrary, the simulation corresponding to the blue spectrum is represented by the "+" in Fig. 3 and has a much steeper spectrum compared to the usual values of the soft X-ray excess. We also report in black the corresponding black-body spectrum emitted by the disk at the bottom of the warm corona.

density. To verify this hypothesis, Fig. 6 shows a map of the spectral photon index in the ξ_0–n_H plane. Simulations with large density ($>10^{14}$ cm^{-3}) can indeed produce spectra with the correct spectral photon index (i.e., in the range [2.2–3.2]) for a large ionization parameter of the illumination (ξ_0 larger than a few 10^4 erg s^{-1} cm). In this region of the parameter space, the spectral photon index is also relatively dependent on ξ_0.

3.3. Emission and/or absorption lines

As mentioned above, in the region of the parameter space which agrees with the observational constraint of the soft X-ray excess (dark area in Fig. 3-left), Comptonization is the dominant cooling process. This is of course directly related to the assumed extra heating Q which keeps the corona temperature high enough and strongly weakens the cooling due to free-free or line emission. This also means that the presence of emission and/or absorption features in the output spectrum is expected to be small. Figure 7 shows the ionization fraction of iron and oxygen for $\tau_{cor} = 20$ and $\chi = 0.753$ and 1.35. A large fraction of iron is fully ionized at the corona surface (~30% for $\chi = 0.753$ and >70% for $\chi = 1.35$). Therefore, ionized iron lines are potentially expected, but only around 7 keV and certainly not in the soft X-rays. Correspondingly, oxygen is always fully ionized very deep inside the corona (up to $\tau = 5$ for $\chi = 0.753$ but in the entire corona for $\chi = 1.35$). There is no chance for line emission to get out of the corona without being completely smeared by Comptonization effects. This confirms that no lines are expected from this element and we have checked that this is the case for all the other elements, especially those producing lines below 2 keV (e.g., silicon, magnesium). In conclusion, the spectra presented in Fig. 4 do not show any strong emission and/or absorption features in the energy range where soft X-ray excess is observed.

4. Discussion

4.1. Brief summary

Here we used the state-of-the-art radiative transfer code TITAN coupled with the Monte Carlo code NOAR to simulate the physical and radiative properties of optically thick and dissipative coronae for different sets of optical depth, density, and internal heating power. We also assumed illumination from above by X-rays, characterized by the ionization parameter ξ_0, and from below by an optically thick accretion disk radiating as a black body with a temperature of T_{bb}. The simulations included all the relevant cooling and heating processes. The vertical temperature profile of the corona was computed assuming radiative equilibrium and the total emitting spectrum (continuum and emitting and/or absorbing features) was produced.

We show that, in a large part of the parameter space, Compton scattering is the dominant cooling process which balances the internal heating power of the corona. Moreover, there is a region of the parameter space where warm (kT in 0.1–2 keV) and optically thick ($\tau \sim 20$) coronae produce spectra in agreement with the observed soft X-ray excess spectral shape. No strong emission and/or absorption features are observed. This region of the parameter space is also consistent with a slightly patchy corona (covering factor between 0.9 and 1) in radiative equilibrium above a non-dissipative accretion disk, all the power being released in the warm corona. These results are in very good agreement with the physical constraints obtained from the fit of the soft X-ray excess with warm Comptonization model (e.g., P13, P18) and with the theoretical estimates made by R15. However, our more accurate and more physical simulations differ significantly from the ones done by García et al. (2019), where some fundamental ingredients (like the corona internal heating power) were not included. Our results show that a warm and optically thick corona can indeed explain the soft X-ray excess, provided that such coronal heating is allowed.

4.2. An accretion disk and two powerful coronae to explain the broad-band spectral emission of radio-quiet AGNs

The results of our analysis crucially depend on the assumption that internal heating power is released in the warm corona up to large optical depth ($\tau > 10$). Indeed, if Q goes to zero, the equations shown in Sect. 2 reduce to the standard radiative profiles of gray atmospheres. On the other hand, the radiative properties of the warm corona are directly related to the conditions of radiative equilibrium with the accretion disk. A powerful warm corona almost entirely covering a nondissipative disk will naturally produce spectra in agreement with the observed soft X-ray excess spectral properties.

This is very similar to the case of the hot corona that produces the hard X-ray (above ~2 keV) emission in radio-quiet AGNs. This hot corona is also believed to be dominated by Comptonization and to have its own local heating (e.g., Merloni & Fabian 2001). Furthermore, its radiative properties are strongly constrained by its radiative equilibrium with the surrounding colder regions, which are sources of soft seed photons (e.g., Haardt & Maraschi 1991, 1993; Haardt et al. 1997).

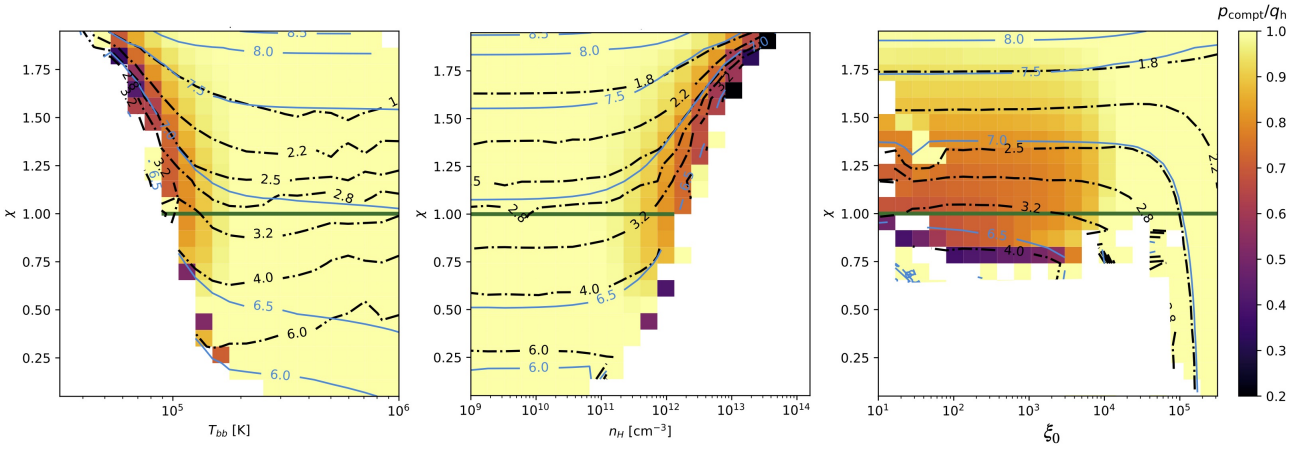

Fig. 5. Contours of the warm corona temperature (blue lines) and the warm corona spectral photon index (black dashed lines) in the planes *from left to right*: χ–T_{bb}, χ–n_H, and χ–ξ_0. When T_{bb}, n_H, or ξ_0 are not variable they are fixed to $T_{bb} = 10^5$ K, $n_H = 10^{12}$ cm^{-3}, and $\xi_0 = 10^3$ erg s^{-1} cm. The corona optical depth τ_{cor} is fixed to 20. The background colors correspond to the Compton cooling to corona heating fraction whose color scale is reported on the right. Similarly to Fig. 2 the green line corresponds to the condition $\chi = 1$.

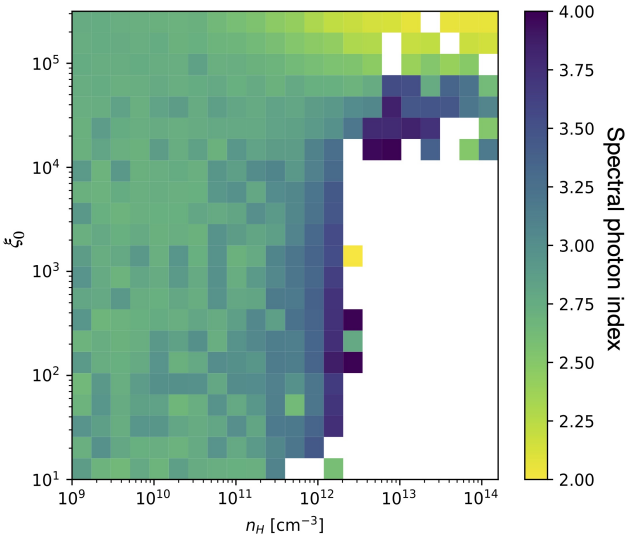

Fig. 6. Map of the spectral photon index of the warm corona emission in the ξ_0–n_H plane. The other parameters are fixed to $T_{bb} = 10^5$ K, $\chi = 1$ and $\tau_{cor} = 20$.

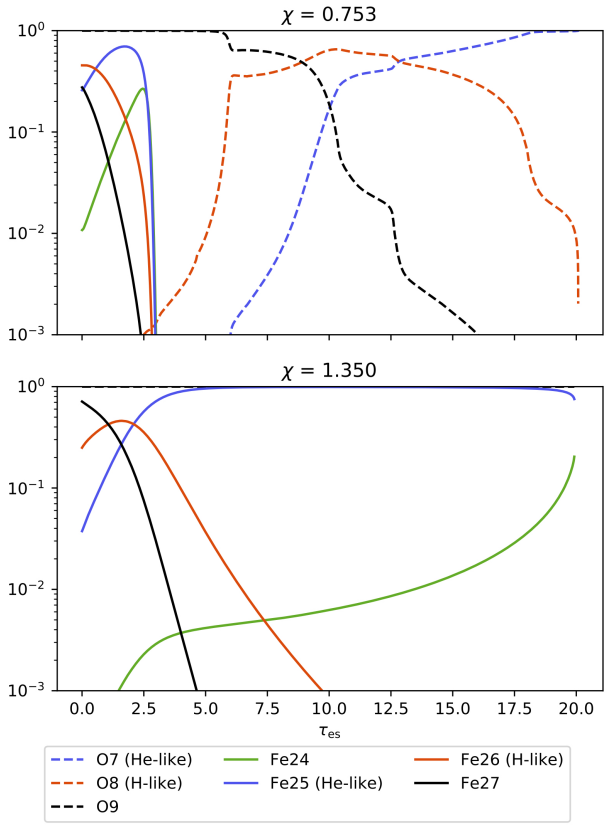

Fig. 7. Ionization state of iron and oxygen across the corona for $\tau_{cor} = 20$ and $\chi = 0.753$ (*top*) and 1.35 (*bottom*). The other parameters are fixed to $T_{bb} = 10^5$ K, $\xi_0 = 10^3$ erg s^{-1} cm, and $n_H = 10^{12}$ cm^{-3}. We note that for $\chi = 1.350$, oxygen is fully ionized throughout the entire corona.

However, in order to agree with hard X-ray observations (spectral photon index $\Gamma \sim 1.9$, temperature $kT \sim$100–300 keV) the hot corona has to be optically thin and significantly patchy (see also discussion in P18).

Combining these constraints for the hot and warm coronae, the UV/soft X-ray/hard X-ray spectral emission of radio quiet AGNs would result from the radiative equilibrium between three main components: a weakly dissipative accretion disk and two powerful coronae, one optically thick and warm and one optically thin and hot (see also e.g., Kubota & Done 2018). Variations in the geometry and/or in the repartition of the heating power among these three components would produce the palette of observed broad-band spectral shapes.

4.3. Origin of the warm corona heating

The immediate question raised by this work refers to the origin of the warm corona internal heating power and the reason why it should be preferentially released in the upper layer of the accretion flow rather than in its deeper layers as assumed in standard accretion disk theory (e.g., Shakura & Sunyaev 1973). While a detailed answer to these questions is beyond the scope of this paper, we note that recent simulations and modeling of accretion flows seem to offer some clues. Clearly, the magnetic field

plays a crucial role here and we naively expect that the buoyant rise of magnetic field generated within a magnetically dominated accretion disk could transport substantial amounts of energy vertically and then heat up the upper layers of the accretion flow (e.g., Merloni et al. 2000; Hirose et al. 2006; Begelman et al. 2015). Very recently, through radiative transfer computation in hydrostatic and radiative equilibrium, Gronkiewicz & Różańska (2020) showed that gas heating by magnetic dynamo (following Begelman et al. 2015) is indeed able to heat the upper layers of the accretion flow up to a few keV for optical depths as great as approximately ten. By construction, in this approach, the underlying disk cannot be completely passive, but these results offer support to the presence of such local heating close to the disk surface.

Recent general-relativistic magnetohydrodynamic (GRMHD) simulations also indicate that magnetized disks accrete preferentially through the disk atmosphere where the disk is magnetically dominated (Beckwith et al. 2009; Zhu & Stone 2018; Mishra et al. 2020; Jiang et al. 2019c). Such "coronal accretion" could play the role of our warm corona if some heating linked to the accretion phenomena could be locally released. In another domain of application, 3D radiation-MHD calculations, when applied to protostellar disks, show that the disk surface layer can indeed be heated by dissipating the disk magnetic field, while the disk interior is "magnetically dead" and colder than a standard accretion disk (e.g., Hirose & Turner 2011). These different results suggest that the presence of local heating power at the disk surface and up to optical depths of a few is physically plausible.

4.4. Potential impacts of the presence of a warm corona in the upper layers of the accretion flow

The presence of a warm plasma in the upper layers of the accretion flow could have several effects on the dynamical, spectral, and temporal properties of the accretion flow itself. It is already known that a warm corona can stabilize the underlying accretion disk, which is otherwise subject to radiation pressure instability (see Czerny 2019 for a very recent review). More unexpectedly, the presence of a warm corona in the quasar SED has recently been shown to be an important element in reproducing the extreme part of the main sequence of quasars[5], especially quasars with particularly strong FeII emission (Panda et al. 2019). These two examples show the wide variety of impacts expected from the existence of such a warm corona in the inner regions of an AGN. Below, we indicate a few other effects suggested by the present analysis.

4.4.1. Outflows

A warm corona could play a major role in the production of disk outflows. The fact that the corona could be out of hydrostatic equilibrium has already been pointed out by R15 and outflows may naturally appear (see also the discussion in Gronkiewicz & Różańska 2020). A precise understanding of these effects would require a numerical resolution of the disk–corona vertical equilibrium in the gravitational potential of the central compact object which is far beyond the scope of the present paper where we simply assume a constant coronal density. Nevertheless, we would like to make a few admittedly qualitative remarks. Interestingly, the comparison of wind signatures in AGNs and XrBs with outflow MHD simulations suggests high ejection efficiencies $p > 0.5$ with $\dot{M}_{\rm acc} \propto R^{\rm p}$ (Zhang & Xie 2013; Fukumura et al. 2015, 2018; Chakravorty et al. 2016). Such high values of p are more easily reached if there is some heating deposit at the disk surface (e.g., Casse & Ferreira 2000; Ferreira & Casse 2004). As shown in the present study, the presence of a warm corona could also explain the soft X-ray excess observed in a large number of AGNs, and therefore we could expect to find stronger wind signatures in objects where a strong soft X-ray excess is also present. To our knowledge, no such relation has been observed yet. However, the observational signatures are not obvious given the variability of the wind signatures and the potential dependence on physical parameters such as for example the disk–corona inclination. As we have seen, the importance and the spectral shape of the warm corona emission also depend on parameters like the disk temperature, the density of the warm corona, and illumination by the hot corona. Therefore, even if there is significant heating deposit at the disk surface, which would favor disk outflows, the warm corona emission may not be always sufficient to produce soft X-ray excess.

4.4.2. Spectral variability

We show in Sect. 3.2.3 that at low density, high disk temperature, or low illumination, the corona thermal properties and spectral emission depend almost exclusively on χ. As a consequence, no significant spectral variability is expected unless the warm corona–disk structure changes, for example, if the corona becomes more patchy (χ will increase) or the disk becomes more dissipative (χ will decrease).

For densities larger than $\sim 10^{12}\,{\rm cm}^{-3}$, disk temperatures lower than $\sim 10^5\,{\rm K}$ or corona illumination with ξ_0 larger than $10^4\,{\rm erg\,cm\,s}^{-1}$ however, the dependence on these parameters becomes important. Moreover, the ranges of density and disk temperature in agreement with a soft X-ray excess spectral shape become narrower. Even if χ remains constant, small changes of $n_{\rm H}$, $T_{\rm bb}$ or ξ_0 are expected to produce significant spectral variability of the warm corona emission and consequently on the soft X-ray range. Interestingly, high illumination can compensate the limitations due to overly large densities or overly low disk temperatures. However, obtaining the correct spectral shape could require some fine tuning between these parameters.

4.4.3. Reverberation lags

Delays (or "lags") between the different energy bands of the X-ray continua have been detected many times in the past 10 years (e.g., De Marco et al. 2013, 2015, 2017; Kara et al. 2016; Epitropakis et al. 2016). On long timescales, hard X-rays lag behind the soft X-rays while at short timescales the reverse is observed. The former situation is generally interpreted as intrinsic accretion fluctuations which drive the variability from the outer (and colder) parts of the accretion flow to the inner (and hotter) parts. The negative lags (that is, when the soft X-rays lag behind the hard X-rays), on short timescales, are interpreted as reverberation lags and would be due to the time delays between the changes in the direct X-ray continuum and the reprocessed, reflected X-rays from the disk (see Uttley et al. 2014; De Marco & Ponti 2019 for recent reviews). Simulations built to reproduce these lags generally assume the presence of a point-like X-ray source (the so-called lamp-post model) above a cold standard accretion disk (Emmanoulopoulos et al. 2014;

[5] See Marziani et al. (2018) for a recent review on the quasar main sequence.

Cackett et al. 2014; Chainakun & Young 2015; Epitropakis et al. 2016; Chainakun et al. 2016 but see Chainakun et al. 2019; Mahmoud & Done 2018; Mahmoud et al. 2019 for radially stratified geometries). If this interpretation of the negative lags is correct, part of the soft X-ray emission should be explained by reflected photons. But the presence of a warm corona at the surface of the accretion disk could modify this picture. First, the shape of the reflection component can be different if the presence of a warm corona at the surface of the disk is taken into account, because it can significantly modify the ionization conditions at the surface of the accretion flow. Second, the soft X-ray photons emitted by the warm corona that will reach the observer will have a pathway that is clearly distinct from that of the hard X-ray photons. We can expect that a radially stratified geometry, with the hot corona in the inner region and the warm corona outside covering the inner part of the optically thick accretion disk, will produce time lags between the hard and soft energy ranges. The timing properties of a geometry of this type were recently studied and applied to X-ray binaries (Mahmoud & Done 2018; Mahmoud et al. 2019) and the frequency-dependent lags between the X-ray bands were successfully reproduced. While these results strongly depend on the assumed geometry of the accretion flow, which is little understood, they are encouraging and provide hope for an application in AGNs.

5. Conclusion

We studied the radiative equilibrium and spectral emission of an optically thick plasma (the so-called warm corona) heated by an internal source of power and illuminated from above by a hard X-ray power law and from below by a disk black-body. Such a plasma has been proposed to explain the soft X-ray excess observed in a large number of AGNs, however its radiative properties have not yet been studied in detail. We made simulations using the latest version of the radiative transfer code TITAN coupled with the Monte-Carlo code NOAR, the latter fully accounting for Compton scattering of continuum and lines. We tested different plasma optical depths, densities, internal heating powers, disk temperatures, and ionization parameters of the power law illumination. Our main conclusions are as follows.

- In a large part of the parameter space, the Compton cooling is dominant across all the corona. For a given optical depth, higher internal heating, higher disk temperatures, lower densities, and higher illumination favor this dominance.
- The emission and absorption lines are also expected to be weak or completely absent due to the high ionization state of matter in the upper part (τ of a few) of the corona where the ions are highly ionized and even completely stripped.
- There is a portion of the parameter space where the spectral emission of the warm corona has spectral properties (spectral index, temperature) similar to those observed for the soft X-ray excess.
- This portion of the parameter space is consistent with a warm corona covering a large part of a weakly dissipative accretion disk.

These results confirm the modeling done by Różańska et al. (2015), they agree with the observational estimates of Petrucci et al. (2013, 2018), and they rule out the limitations generally put forward (i.e., no Compton dominance, emission and/or absorption lines expected in the outgoing spectrum) concerning the warm Comptonization modeling of the soft X-ray excess.

However, these conclusions rely on the existence of internal heating power in the corona. This is a mandatory condition for the existence of such warm plasma above the accretion disk. The origin of such an internal heating power is unknown although recent simulations and modeling of magnetized accretion flows seem to offer some support to it.

The dependencies of the warm corona properties on the model parameters (such as e.g., the densities and the hard power-law illumination) could explain the diversity of the soft X-ray excess spectral shape and even its absence in some AGNs. This will be studied in a forthcoming paper.

We note that during the completion of our paper, we became aware of a study by Ballantyne (2020, hereafter B20) covering a similar subject. This latter paper is complementary to ours and we discuss here the main differences and similarities. First, in B20 the reflection is included in the output spectra. This makes a comparison to our spectra difficult. Similar to our work however, B20 generally assumes constant corona densities, but the author considers a small range of corona densities of a few 10^{14} cm^{-3}, two orders of magnitude larger than the typical values of 10^{12} cm^{-3} used in our simulations. At such large densities, and even if we have difficulty in obtaining TITAN solutions that are able to converge, we do not expect a spectral emission in agreement with the soft X-ray excess spectral shape (see Fig. 5 middle plot). The illumination above the warm corona may certainly play a crucial role here, as explained in Sect. 3.2.3 and in agreement with the conclusions of B20. However, we do not simulate the same range of parameters, and so again a precise comparison is not easy. Our study covers a large range of densities but lower than 10^{14} cm^{-3}. Furthermore, we show that smaller densities help to obtain better conditions to produce a warm corona with the required properties. Interestingly, B20 is also able to study the case of a warm corona with $\tau_{\rm cor} = 10$ in hydrostatic equilibrium, but contrary to R15, this hydrostatic equilibrium does not include the presence of the underlying disk. Even so, the vertical decrease in density of the B20 hydrostatic solution favors the formation of the warm corona. Another important difference between B20 and our analysis is that the corona internal heating in B20 is a fraction of the total dissipation. In this case, increasing the coronal heating implies a decrease of the disk flux while in our calculations the two quantities are disconnected. This allows us to use the internal heating as a free parameter and to explore a larger range of values. In conclusion, our approaches are slightly different and our parameter spaces are not the same. Nevertheless, we both conclude that a warm corona with the correct properties could reproduce the observed soft X-ray excess of type 1 AGNs.

Acknowledgements. We thank the anonymous referee for comments which helped us improve the clarity of the paper. We warmly thanks Anne-Marie Dumont, who was providing us with the newest version of NOAR and the associated documentation. POP acknowledges financial support from CNES and the French PNHE. SB, ADR and GM acknowledges financial support from the Italian Space Agency under grant ASI-INAF 2017-14-H.O. AR and DG acknowledge financial support from Polish National Science Center grants No. 2015/17/B/ST9/03422 and 2015/18/M/ST9/00541. BC acknowledges the financial support by the National Science Centre, Poland, grant No. 2017/26/A/ST9/00756 (Maestro 9). FU acknowledges financial support from ASI and INAF under INTEGRAL "accordo ASI/INAF 2013-025-R1".

References

Abrassart, A., & Dumont, A. M. 2001, in X-ray Astronomy: Stellar Endpoints, AGN, and the Diffuse X-ray Background, eds. N. E. White, G. Malaguti, & G. G. C. Palumbo, 599, 489
Ballantyne, D. R. 2020, MNRAS, 491, 3553
Beckwith, K., Hawley, J. F., & Krolik, J. H. 2009, ApJ, 707, 428
Begelman, M. C., Armitage, P. J., & Reynolds, C. S. 2015, ApJ, 809, 118
Bianchi, S., Guainazzi, M., Matt, G., Fonseca Bonilla, N., & Ponti, G. 2009, A&A, 495, 421

Cackett, E. M., Zoghbi, A., Reynolds, C., et al. 2014, MNRAS, 438, 2980
Casse, F., & Ferreira, J. 2000, A&A, 361, 1178
Chainakun, P., & Young, A. J. 2015, MNRAS, 452, 333
Chainakun, P., Young, A. J., & Kara, E. 2016, MNRAS, 460, 3076
Chainakun, P., Watcharangkool, A., Young, A. J., & Hancock, S. 2019, MNRAS, 487, 667
Chakravorty, S., Petrucci, P.-O., Ferreira, J., et al. 2016, A&A, 589, A119
Collin, S., Dumont, A.-M., & Godet, O. 2004, A&A, 419, 877
Crummy, J., Fabian, A. C., Gallo, L., & Ross, R. R. 2006, MNRAS, 365, 1067
Czerny, B. 2019, Universe, 5, 131
Czerny, B., Nikoajuk, M., Rozanska, A., et al. 2003, A&A, 412, 317
De Marco, B., & Ponti, G. 2019, Astron. Nachr., 340, 290
De Marco, B., Ponti, G., Cappi, M., et al. 2013, MNRAS, 431, 2441
De Marco, B., Ponti, G., Muñoz-Darias, T., & Nandra, K. 2015, ApJ, 814, 50
De Marco, B., Ponti, G., Petrucci, P. O., et al. 2017, MNRAS, 471, 1475
Dumont, A. M., Abrassart, A., & Collin, S. 2000, A&A, 357, 823
Dumont, A. M., Collin, S., Paletou, F., et al. 2003, A&A, 407, 13
Emmanoulopoulos, D., Papadakis, I. E., Dovčiak, M., & McHardy, I. M. 2014, MNRAS, 439, 3931
Epitropakis, A., Papadakis, I. E., Dovčiak, M., et al. 2016, A&A, 594, A71
Ferreira, J., & Casse, F. 2004, ApJ, 601, L139
Fukumura, K., Tombesi, F., Kazanas, D., et al. 2015, ApJ, 805, 17
Fukumura, K., Kazanas, D., Shrader, C., et al. 2018, ApJ, 853, 40
García, J. A., Kara, E., Walton, D., et al. 2019, ApJ, 871, 88
Gierlinski, M., & Done, C. 2004, MNRAS, 349, L7
Gronkiewicz, D., & Różańska, A. 2020, A&A, 633, A35
Haardt, F. 1993, ApJ, 413, 680
Haardt, F., & Maraschi, L. 1991, ApJ, 380, L51
Haardt, F., & Maraschi, L. 1993, ApJ, 413, 507
Haardt, F., Maraschi, L., & Ghisellini, G. 1997, ApJ, 476, 620
Hirose, S., & Turner, N. J. 2011, ApJ, 732, L30
Hirose, S., Krolik, J. H., & Stone, J. M. 2006, ApJ, 640, 901
Jiang, J., Fabian, A. C., Dauser, T., et al. 2019a, MNRAS, 489, 3436
Jiang, J., Fabian, A. C., Wang, J., et al. 2019b, MNRAS, 484, 1972
Jiang, Y.-F., Stone, J. M., & Davis, S. W. 2019c, ApJ, 880, 67
Jin, C., Ward, M., & Done, C. 2012, MNRAS, 425, 907
Kaastra, J. S., Petrucci, P. O., Cappi, M., et al. 2011, A&A, 534, A36
Kara, E., Alston, W. N., Fabian, A. C., et al. 2016, MNRAS, 462, 511
Kubota, A., & Done, C. 2018, MNRAS, 480, 1247
Magdziarz, P., Blaes, O. M., Zdziarski, A. A., Johnson, W. N., & Smith, D. A. 1998, MNRAS, 301, 179
Mahmoud, R. D., & Done, C. 2018, MNRAS, 480, 4040
Mahmoud, R. D., Done, C., & De Marco, B. 2019, MNRAS, 486, 2137
Marziani, P., Dultzin, D., Sulentic, J. W., et al. 2018, Front. Astron. Space Sci., 5, 6
Matt, G., Marinucci, A., Guainazzi, M., et al. 2014, MNRAS, 439, 3016
Mehdipour, M., Kaastra, J. S., Kriss, G. A., et al. 2015, A&A, 575, A22
Merloni, A., & Fabian, A. C. 2001, MNRAS, 321, 549
Merloni, A., Fabian, A. C., & Ross, R. R. 2000, MNRAS, 313, 193
Middei, R., Bianchi, S., Cappi, M., et al. 2018, A&A, 615, A163
Middei, R., Bianchi, S., Petrucci, P. O., et al. 2019, MNRAS, 483, 4695
Mishra, B., Begelman, M. C., Armitage, P. J., & Simon, J. B. 2020, MNRAS, 492, 1855
Page, K. L., Schartel, N., Turner, M. J. L., & O'Brien, P. T. 2004, MNRAS, 352, 523
Panda, S., Czerny, B., Done, C., & Kubota, A. 2019, ApJ, 875, 133
Petrucci, P.-O., Haardt, F., Maraschi, L., et al. 2000, ApJ, 540, 131
Petrucci, P.-O., Paltani, S., Malzac, J., et al. 2013, A&A, 549, A73
Petrucci, P.-O., Ursini, F., De Rosa, A., et al. 2018, A&A, 611, A59
Porquet, D., Reeves, J. N., Matt, G., et al. 2018, A&A, 609, A42
Rees, M. J. 1984, ARA&A, 22, 471
Różańska, A., Dumont, A. M., Czerny, B., & Collin, S. 2002, MNRAS, 332, 799
Różańska, A., Goosmann, R., Dumont, A.-M., & Czerny, B. 2006, A&A, 452, 1
Różańska, A., Malzac, J., Belmont, R., Czerny, B., & Petrucci, P.-O. 2015, A&A, 580, A77
Shakura, N. I., & Sunyaev, R. A. 1973, A&A, 24, 337
Tomsick, J. A., Parker, M. L., García, J. A., et al. 2018, ApJ, 855, 3
Tortosa, A., Bianchi, S., Marinucci, A., Matt, G., & Petrucci, P. O. 2018, A&A, 614, A37
Ursini, F., Petrucci, P.-O., Matt, G., et al. 2016, MNRAS, 463, 382
Ursini, F., Petrucci, P. O., Matt, G., et al. 2018, MNRAS, 478, 2663
Uttley, P., Cackett, E. M., Fabian, A. C., Kara, E., & Wilkins, D. R. 2014, A&ARv, 22, 72
Walter, R., & Fink, H. H. 1993, A&A, 274, 105
Walton, D. J., Nardini, E., Fabian, A. C., Gallo, L. C., & Reis, R. C. 2013, MNRAS, 428, 2901
Zhang, J.-F., & Xie, F.-G. 2013, MNRAS, 435, 1165
Zhu, Z., & Stone, J. M. 2018, ApJ, 857, 34

Appendix A: Appendix

The general radiative equilibrium of a corona above a disk has already been discussed in P18. However a few mistakes are present in this latter paper. We show the correct equations here below in light of the general results discussed in Sect. 2.

Following the notation of this paper, $F_{\rm tot,disk} = \pi B$ is the total flux emitted by the disk that enters the corona, and $F_{\rm cor} = 4\pi Q\tau_{\rm cor}$ is the flux produced by dissipation inside the corona. In the case of a corona dominated by Comptonization (i.e., zero absorption) in plain parallel geometry and coherent scattering (no photon energy gain during scattering) the transmitted and reflected back fluxes of the disk can be written:

$$F_{\rm disk,trans} = \frac{F_{\rm tot,disk}}{1+\frac{3}{4}\tau_{\rm cor}} = \frac{\pi B}{1+\frac{3}{4}\tau_{\rm cor}}, \tag{A.1}$$

$$F_{\rm disk,ref} = \frac{\frac{3}{4}\tau}{1+\frac{3}{4}\tau}F_{\rm tot,disk} = \frac{\frac{3}{4}\tau}{1+\frac{3}{4}\tau}\pi B. \tag{A.2}$$

The observed flux emitted at the top of the corona is equal to:

$$F_{\rm out} = \frac{F_{\rm tot,disk}}{1+\frac{3}{4}\tau_{\rm cor}} + \frac{F_{\rm cor}}{2} = \frac{\pi B}{1+\frac{3}{4}\tau_{\rm cor}} + \frac{4\pi Q\tau_{\rm cor}}{2}. \tag{A.3}$$

This equation assumes that $F_{\rm cor}$ is distributed homogeneously in the warm corona and is entirely radiated isotropically, that is, that half of it is emitted upward while the other half is emitted backward.

On the other hand, at the transition between the corona and the disk, the radiative equilibrium imposes:

$$F_{\rm tot,disk} = C_f(F_{\rm rep} + F_{\rm disk,intr}) \tag{A.4}$$

$$= C_f\left(\frac{\frac{3}{4}\tau_{\rm cor}}{1+\frac{3}{4}\tau_{\rm cor}}F_{\rm tot,disk} + \frac{F_{\rm cor}}{2} + F_{\rm disk,intr}\right), \tag{A.5}$$

where $F_{\rm rep}$ is the luminosity coming from the warm corona that is reprocessed in the disk (we assume an albedo of zero), $F_{\rm disk,intr}$ is the instrinsic disk heating flux, and C_f the warm corona covering factor. A covering factor $C_f = 1$ corresponds to a corona covering the disk entirely, while $C_f < 1$ corresponds to a patchy corona where part of the disk emission is radiated away without crossing the warm corona.

Introducing the amplification factor $A = 1 + F_{\rm cor}/F_{\rm tot,disk}$, these equations can be combined to give:

$$A - 1 = \frac{F_{\rm cor}}{F_{\rm tot,disk}} = 2\left(\frac{1+\frac{3}{4}\tau_{\rm cor}(1-C_f)}{C_f(1+\frac{3}{4}\tau_{\rm cor})}\right) - 2\frac{F_{\rm disk,intr}}{F_{\rm tot,disk}} \tag{A.6}$$

$$\frac{F_{\rm disk,intr}}{F_{\rm tot,disk}} > \frac{1}{1+\frac{3}{4}\tau_{\rm cor}} - \frac{F_{\rm cor}}{2F_{\rm tot,disk}} = \left.\frac{F_{\rm disk,intr}}{F_{\rm tot,disk}}\right|_{\rm min}. \tag{A.7}$$

In the case $C_f = 1$ and no intrinsic disk emission, Eq. (A.6) simply gives:

$$\frac{F_{\rm cor}}{F_{\rm tot,\,disk}} = \frac{2}{1+\frac{3}{4}\tau_{\rm cor}}. \tag{A.8}$$

Moreover, the amplification factor is related to the parameter χ defined in Eq. (6) via the following equation:

$$\chi = \frac{2(1+3\tau_{\rm cor}/4)(A-1)}{2+(1+3\tau_{\rm cor}/4)(A-1)}. \tag{A.9}$$

Equations (A.6) and (A.7) are different from Eqs. (19) and (21) of P18 (assuming the albedo $a = 0$ and that the corona covers the disk entirely, i.e., $g = 1$). While Eqs. (19) and (21) of P18 agree with an optical depth of the order unity, they do not stand for large optical depth like the one expected in the warm corona. The main impacts of the use of Eqs. (A.6) and (A.7) of the present paper is on the expression of the amplification factor and of Fig. 1 of P18. The correct version of this figure is shown in Fig. A.1. The conclusions of P18 still apply, that is, the observational characteristics of the soft X-ray excess (i.e., a photon index of ~2.5 and a temperature in 0.1–2 keV) agree with an extended warm corona covering the disk which is mainly nondissipative.

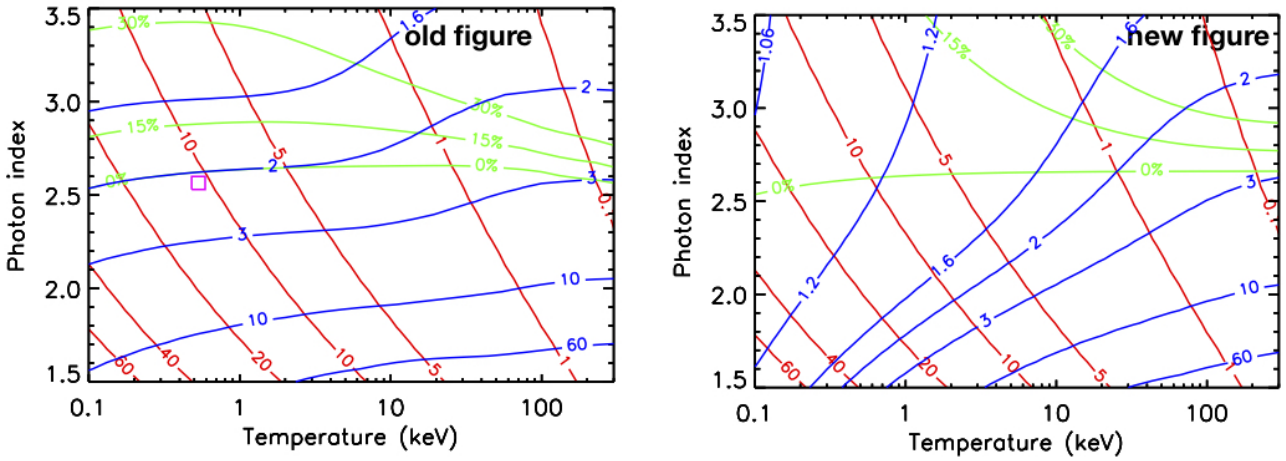

Fig. A.1. *Left*: figure published in P18. *Right*: new figure.